ABSOLUTE TRANSITION PROBABILITIES FOR Ni I AND THE SOLAR NICKEL ABUNDANCE

Thesis by

William Norman Lennard

In Partial Fulfillment of the Requirements
For the Degree of
Doctor of Philosophy

California Institute of Technology
Pasadena, California
1974

(Submitted May 28, 1974)

To Ginny

ACKNOWLEDGMENTS

The author wishes to thank the entire faculty and staff of the Kellogg Radiation Laboratory for their support and assistance during the course of this work. The friendly and cooperative atmosphere in this Laboratory has made the author's stay at Caltech a most pleasant one.

In particular, special thanks is extended to Professor Ward Whaling. His suggestion of this research topic and his guidance and encouragement throughout have made this thesis possible.

The author would also like to thank the staff of the Kitt Peak National Observatory data center for making his stay in Tucson so pleasant. Special thanks must go to Mr. Larry Testerman for his help with the equivalent width measurements and for his calculation of the solar nickel abundance. Kitt Peak generously provided the author with their recent solar spectrum data, their computer programs and unlimited computing time which made possible the analysis of the solar intensities.

Dr. Peter L. Smith and Dr. Donald Mickey provided invaluable assistance in the early stages of the work. W. A. Zajc and R. M. Sills helped with various aspects of the measurements. Dr. J. E. Ross kindly provided tracings of the unpublished Michigan Solar Atlas from the records of the U.C.L.A. astronomy department. Dr. R. Foy of the Observatoire de Meudon, France, supplied useful data for the curve of growth analysis. R. G. Marcley assisted in the calibration of some of the electronic equipment used in this work.

The research was supported in part by the National Science Foundation [GP-28027] and the Office of Naval Research [N00014-67-A-0094-0022]. The author gratefully acknowledges the support of the California Institute of Technology in the form of Graduate Research Assistantships, Graduate Teaching Assistantships and Tuition Scholarships during the course of his studies.

Finally, the author thanks his parents for their patience.

ABSTRACT

Absolute transition probabilities have been measured for 97 lines from 11 levels in Ni I using the lifetime and branching ratio technique. Relative transition probabilities have been determined for 6 lines out of 2 levels whose lifetimes have been measured elsewhere. We have measured equivalent widths from the Kitt Peak Preliminary Solar Atlas for 48 of the lines for which absolute transition probabilities have been measured. An empirical solar curve of growth has been constructed for Ni I to test the consistency of the transition probability and equivalent width measures. The solar data have been used to calculate a value for the photospheric Ni abundance $A_{Ni} = 6.29 \pm 0.2$ based on the results of the transition probability measurements. A new transition ($z^5G^o_5 - e^3G_5$, λ4633.031) has been observed in the Ni I spectrum.

TABLE OF CONTENTS

ACKNOWLEDGMENTS iii

ABSTRACT iv

1. INTRODUCTION 1

2. ATOMIC PHYSICS 4

3. LIFETIME MEASUREMENTS 9

3.1 The Beam-Foil Method 9

3.2 Data Accumulation 10

3.3 Selection of Lines 12

3.4 Data Analysis and Cascading 13

3.5 Discussion of Results 19

3.6 Uncertainties in the Lifetime Measurements 26

4. TRANSITION PROBABILITIES 28

4.1 Introduction 28

4.2 Branching Ratio Measurements 28

4.3 Search for Branches 33

4.4 Results of Branching Ratio Measurements 34

4.4.1 LEVEL $z^3D_2^o$ 34

4.4.2 LEVEL $z^1F_3^o$ 35

4.4.3 LEVEL $z^3P_2^o$ 35

4.4.4 LEVEL $z^3P_1^o$ 36

4.4.5 LEVEL $z^3F_3^o$ 36

4.4.6 LEVEL $z^3F_2^o$ 36

4.4.7 LEVEL $z^1D_2^o$ 37

4.4.8 LEVEL e^3G_5 37

4.4.9 LEVEL e^5F_5 38

4.4.10 LEVEL g^3F_3 38

4.4.11 LEVEL e^3P_2 39

4.4.12 LEVEL $z^5F^o_4$ 40

4.4.13 LEVEL $z^3F^o_4$ 40

4.5 Self-Absorption 41

4.6 Uncertainties in the Transition Probabilities 44

4.7 Comparison of Results with Other Works 47

5. SOLAR DATA 52

5.1 Introduction 52

5.2 Equivalent Widths for Solar Ni I Lines 53

5.3 Uncertainties in the Equivalent Widths 57

5.4 Solar Curve of Growth for Ni I 59

6. SOLAR ABUNDANCE OF NICKEL 64

6.1 Introduction 64

6.2 Abundance from Model Atmosphere Calculations 65

6.3 Abundance from the Curve of Growth 68

6.4 Adopted Value for the Solar Ni Abundance 69

6.5 Use of Abundance Value to Check Lifetime Values 70

APPENDIX A - HYDROGENIC TRANSITIONS IN MULTIPLY CHARGED Fe AND Ni IONS (reprint) 72

APPENDIX B - ABSOLUTE BEAM-FOIL EXCITATION PROBABILITIES OF HYDROGEN-LIKE STATES IN IRON (reprint) 77

APPENDIX C - ABSOLUTE TRANSITION PROBABILITIES IN Ni I (reprint) 83

APPENDIX D - SPECTROMETER CALIBRATION 89

D.1 Introduction 89

D.2 Standard Lamp Source 89

D.3 Calibration Procedure 90

APPENDIX E - BEAM SCATTERING 96

APPENDIX F - FURTHER INVESTIGATION OF THE LIFETIME OF THE $z^3P_2^o$ LEVEL IN Ni I 100

APPENDIX G - SEARCH FOR UNCLASSIFIED LINES IN THE SPECTRUM OF Ni I 105

REFERENCES 107

TABLES 113

FIGURES 177

1. INTRODUCTION

The iron group elements are an important constituent of the solar material. The amount of these elements present in the sun has been the subject of considerable controversy. Iron itself has been extensively studied, and there is now good agreement in abundance values obtained using atomic data measured by quite different methods (Garz *et al.* 1969; Baschek *et al.* 1970; Martinez-Garcia 1971a; Huber and Parkinson 1972; Smith and Whaling 1973). Attention has now turned to other elements in the iron group. Since nickel is the second most abundant element in the group, it is important to establish its abundance accurately.

Table 1 shows recent solar abundance values for Ni obtained by different investigators using several different methods. The meteoritic and coronal values (based on coronal EUV and forbidden lines in the visible) indicate a solar abundance A_{Ni} of 6.2-6.6, where $A_{Ni} = \log_{10}(N_{Ni}/N_H) + 12.00$. On the other hand, measurements based on the photospheric Ni lines for which the most extensive and precise solar observations are available yield a value of A_{Ni} in the range 5.1-6.3. On the average, the photospheric values are lower than the coronal and meteoritic values.

The purpose of this thesis is to make an independent study of Ni I with the aim of redetermining the photospheric Ni abundance. Analysis of the known intensity of a solar absorption line yields a value for the product gfN_{Ni}, where g is the statistical weight of the lower level of the transition, f is the oscillator strength for the transition and N_{Ni} is the total number of Ni atoms causing the absorption. Experience with recent Fe studies had cast suspicion on the atomic transition probability values (or gf values) that enter into the abundance analysis. We have aimed at new measurements of absolute gf values for several astrophysically important Ni I lines. We were able to make use of new solar data which became available while the transition probability measurements were in progress.

We have measured absolute transition probabilities using the lifetime and branching ratio method, a technique that was previously successful with Fe. The lifetime of a level is the reciprocal of the sum of the transition probabilities for all the transitions which depopulate that level. The branching ratios are determined by observations of the relative branch (or line) intensities in a hollow cathode discharge for all of the branches out of each upper level.

Ideally, the photospheric abundance of an element can be determined independently from both the first and second spectra. Their agreement, as with Fe I and Fe II, confirms the reliability of the results. The original plan for this thesis included a study of Ni II with the hope of validating the Ni I results. Unfortunately, Ni II is represented by only 7 unblended (red) lines in the solar spectrum. In order to measure the gf value for a weak line, we must observe a strong line from the same upper level in the beam-foil spectrum in order to be able to measure the lifetime of the level. Of the 7 weak solar Ni II lines, 3 originate in 2 different upper levels whose lifetimes we could measure. However, both levels have branches in the vacuum ultraviolet region ($\lambda < 1900$Å), making branching ratio measurements impossible with the present experimental facilities.

As is frequently the case in research on topics of current interest, other results have been reported while this work was in progress. These developments will be discussed in more detail later in the thesis, but the results appear in Table 1 for completeness and a word of explanation is in order.

Garz *et al*. (1970) have measured *relative* transition probabilities for many Ni I lines. They then used the absolute measurements of Lawrence *et al*. (1965) to adjust their values to an absolute scale. Garz (1971) derived a Ni abundance $A_{Ni} = 6.25 \pm 0.15$ based on the relative measurements.

Grevesse and Swings (1970) obtained $A_{Ni} = 6.3 \pm 0.3$ using very weak photospheric [Ni II] absorption lines. The uncertainty assigned to their results indicates the difficulty of the method.

Two of the recent values shown in Table 1 represent efforts to correct the transition probabilities tabulated by Corliss and Bozman (1962) at the National Bureau of Standards (NBS) after studies of Fe had cast doubt on the reliability of the NBS values. The discrepant values of the solar Ni abundance reported by Grevesse (1969) and Takens (1970) illustrate that such corrected values are of limited reliability and are no substitute for accurate measurements.

2. ATOMIC PHYSICS

It has long been known that transitions occur spontaneously between excited atomic states, producing radiation of a definite frequency or wavelength. In order to determine elemental abundances from spectroscopic observations of stellar objects, the probabilities of these transitions are required. Many parameters have been used to characterize atomic transitions, and it is helpful to recognize which ones are directly measured in the laboratory. We will follow the notation of Sobel'man (1972) in this thesis.

In emission, one observes the intensity of a particular spectral line originating from a transition between two atomic states i and f (initial and final). The number of transitions occurring per unit time interval at a time t is the product of the number of atoms in the upper state, $N_i(t)$, and the probability of a spontaneous transition from i to f, A_{if}. For "allowed" electric dipole (or E1) radiation, A_{if} is given by

$$A_{if} = \frac{64\pi^4}{3h\, g_i\, \lambda_{if}^3} |< f \,||\, \vec{P} \,||\, i >|^2 \tag{2.1}$$

where the matrix element is the reduced matrix element of Racah (1942), g_i is the statistical weight of the upper level ($g_i = 2J_i + 1$), λ_{if} is the wavelength of the emitted spectral line, and $\vec{P}$ is the usual electric dipole operator. It can be seen immediately that calculations of A_{if} will be very difficult for many-electron atoms since the construction of accurate wavefunctions is impossible in practice. This is not the case for magnetic dipole (M1) transitions (so-called "forbidden" transitions) where the operator occurring in the transition probability matrix element is

$$\vec{M} = \frac{e}{2m_e c} (\vec{L} + 2\vec{S}) \tag{2.2}$$

which is not a function of $\vec{r}$, the spatial coordinate. Calculations of probabilities for M1 transitions are more reliable, which is one reason why so many entries in Table 1 are based on forbidden lines.

The coefficient of absorption, B_{fi}, and the coefficient of induced emission, B_{if}, are related to A_{if} by the expressions

$$g_i A_{if} = \frac{8\pi h}{\lambda_{if}^3} g_f B_{fi} \tag{2.3}$$

$$g_i B_{if} = g_f B_{fi} \tag{2.4}$$

A frequently used term in astrophysical analyses is the Ladenburg oscillator strength, or gf value. It is defined by the relation

$$g_f f_{fi} = 1.4992 \times 10^{-16} \lambda_{if}^2 g_i A_{if} \tag{2.5}$$

where λ_{if} is expressed in Å . Hereafter, $g_f f_{fi}$ will be denoted simply by gf . The absorption oscillator strength, f_{fi} , represents the number of classical oscillators per atom in the state f necessary to absorb the same amount of energy that is actually absorbed by an atom in a transition from a state f to a state i . According to equation (2.5), the laboratory measurement of an atomic transition probability in emission, A_{if} , is sufficient to determine the corresponding absorption gf value. The latter quantity is directly used to calculate the number of atoms of an element present in the atmosphere of the sun where they absorb continuum radiation originating in the interior to form the solar Fraunhofer line spectrum.

Of fundamental importance in this thesis is the mean lifetime, τ_i , of an excited state i . It is related to the spontaneous transition probabilities for deexcitation (2.1) by the relation

$$\tau_i^{-1} = \sum_{f<i} A_{if} \tag{2.6}$$

where the sum extends over all states, f , of lower excitation potential ($E_f < E_i$) to which transitions occur. It should be noted here that intersystem E1 transitions, with $\Delta S \neq 0$, are possible for complex atoms such as Ni where significant departures from LS-coupling are observed. In spite of this fact, the notation used to designate electronic configurations will be that derived from the LS-coupling scheme, in agreement with Moore's tabulation of Ni I energy levels (Moore 1971). Only the E1 transition probabilities are significant in the summation (2.6). The M1 and E2 (electric quadrupole) probabilities are smaller than the E1 contributions by factors of approximately 10^5 and 10^8 respectively. Transitions which occur via non-electric dipole processes are almost never observed in the laboratory. They are observed, however, in astrophysical sources (Grevesse and Swings 1970).

The usual procedure for determining the contributions to the summation (2.6) has been to use the wavelength tables of Moore (1945, 1950). Her work will hereafter be denoted by RMT (Revised Multiplet Table). This compilation lists 861 lines in the Ni I spectrum, and has served as a valuable reference for spectroscopic investigations of other elements (Martinez-Garcia *et al.* 1971b; Roberts *et al.* 1973a, 1973b; Smith *et al.* 1973; and Cocke *et al.* 1973). The assumption inherent in relying on this source is that spectral lines which do not appear in the RMT are weak. Corliss (1965) has shown that this assumption is *not* justified for Ni I. He finds 139 transitions which do not appear in the RMT. Some of these are strong lines. In order to search for additional unclassified branches from the upper levels under investigation in this work, all possible transitions, λ_{if} , between the known energy levels of Ni I as compiled by Moore (1971) have been computed using the relation

$$\lambda_{if} = \frac{hc'}{E_i - E_f} \tag{2.7}$$

where E_i and E_f are the energies of the upper and lower levels respectively, and c' is the speed of light in air obtained using the Cauchy dispersion formula (Weast 1968). The selection rules were such as to restrict the computations to only those transitions for which

(i) the parities of the upper and lower levels are different;
(ii) $J_i - J_f = 0$ or ±1 (except no $J_i = 0 \rightarrow J_f = 0$);
(iii) $L_i - L_f = 0$, ±1 or ±2; and
(iv) $S_i - S_f = 0$, ±1 or ±2 .

Some justification for constraints (iii) and (iv) is in order. Although these rules are contrary to the usual selection rules governing atomic radiative processes, they are not at all unusual for heavier atoms such as Ni where many departures from Russell-Saunders (or LS-) coupling are observed. The results of this search are given in Section 4 and in Appendix G.

We have also investigated the possibility that some of the energy levels themselves have not been classified. Roth (1970) has done a theoretical study of the possible excited configurations of Ni I and compared his results to the levels appearing in Moore. His work and the review article by Edlén (1973) indicate that the Ni I term structure as it appears in Moore is essentially complete.

3. LIFETIME MEASUREMENTS

3.1 THE BEAM-FOIL METHOD

The measurement of the mean lifetimes of excited atomic levels using the beam-foil (BF) technique has been carried out for a large variety of atoms and ions in recent years. Bashkin (1970) has given a good review of the general method.

The BF technique is essentially a time-of-flight measurement which uses the known velocity of the moving atoms as a time scale. Figure 1 shows a schematic diagram of the apparatus used in this experiment. Spectroscopically pure nickel metal was introduced into the ion source of an electrostatic accelerator. The source was similar to that described by Magnuson et al. (1965) and has been described by Smith and Whaling (1969) and Whaling et al. (1969) with regard to previous work using iron. The nickel was heated to a temperature high enough to increase its vapor pressure to a few millimeters of Hg. The Ni atoms in the vapor state are ionized by electron bombardment. They are then extracted and accelerated electrostatically to a few hundred keV using the 2 MV Van de Graaff generator in the Kellogg Laboratory. A magnetic field then isolated the mass 58 ions to be studied. The resolution of the mass analyzer was better than 5%, which was sufficient to ensure that unavoidable contaminants in the source did not reach the target chamber. The energy of the ion beam was defined by an electrostatic analyzer calibrated in energy to ±0.5% using the $^{1}H(^{19}F,\alpha\gamma)^{16}O$ resonance at 340.46 keV, which was in the mid-range of the energy region used. This accuracy of the calibration ensured that the incident beam velocity was constant to ±0.25%.

The beam was then admitted to the target chamber where the ions were both excited and ionized in traversing a thin carbon foil (nominally 5 ± 3 or 10 ± 4 $\mu g/cm^2$ in thickness). The exciter foil must be a low-Z material to reduce the scattering of the beam, and it must be durable enough to withstand several minutes of bombardment by the heavy Ni ions. Since the particles are moving at a constant velocity (v) after passing through the foil, the distance from the foil, x, is related to the time, (t), after excitation via $x = vt$. As the particles move beyond the foil, the excited atomic states produced by collisions within the target decay spontaneously. By measuring the intensity of the light emitted at a wavelength corresponding to a particular transition, the lifetime of the upper level involved in the transition can usually be determined unless the upper level is itself fed by cascading transitions from levels at higher excitation energies (see Section 3.4). It should be noted here that the vacuum in the target chamber ($\sim 10^{-6}$ torr) was sufficiently low to ensure that the collisional deexcitation lifetime was much longer than the radiative lifetime.

3.2 DATA ACCUMULATION

Light from the radiating beam was dispersed with a 0.3 meter McPherson normal incidence grating monochromator (Model No. 218) equipped with a refrigerated EMI 6256S photomultiplier tube. The grating, ruled with 1200 lines/mm, was blazed at λ5000 to increase the detection efficiency for visible wavelengths observed in first order.

A short segment of the beam, viewed at 90^0 to its direction of motion, was imaged onto the entrance slit of the monochromator by two quartz-lithium fluoride achromats as described by Smith (1972). Demagnification of the beam was employed to reduce the correction necessary to allow for beam scattering in the foil. This correction is discussed in Appendix E. The detector assembly was moved parallel to the beam on a lathe bed as indicated in Figure 1, and photons were counted as a function of the detector to foil distance using conventional pulse-counting electronics.

The particle beam intensity varied over the periods of data accumulation. This variation necessitated using a second photomultiplier to monitor the integrated light from the foil-excited particles at a position just downstream from the target. The number of particles that has passed through the foil is proportional to the integrated light output, so long as the energy of the beam is not varied. This method of normalizing the different counting periods was compared to the usual Faraday cup technique; both techniques yielded the same results within the uncertainties of the measurements. Current from the monitor phototube, an RCA 8575, was integrated using an Elcor current integrator. The time taken to collect a given predetermined charge in the integrator was also recorded since the number of observed counts in the EMI detector included dark current counts which were proportional to the counting time.

3.3 SELECTION OF LINES

A spectrogram of the radiation emitted by a 444 keV Ni beam after passage through a 10 μgm/cm^2 carbon foil was first taken to identify those transitions produced by the beam-foil interaction. A detailed description of the spectroscopic measurement appears in Appendix C. This survey spectrum spanned the wavelength region $\lambda\lambda$3400-6500; the lower limit was determined by the use of a glass prism as the dispersing element in the spectrograph. Brand _et al._ (1973) have observed the Ni beam-foil spectrum in the region $\lambda > 1560$Å and have identified many Ni I and II lines. Our identifications, tabulated in Appendix **C**, are based on wavelengths appearing in the RMT (1945), and on the work of Corliss (1965) and Shenstone (1970) who analyzed the spectra of Ni I and Ni II respectively. To qualify as a certain identification, it was required that the "strongest" line from a given upper level be present, where "strongest" is defined by the work of those investigators cited above. The reader is referred to Appendices A and B for a detailed discussion of those transitions attributed to Ni IV, Ni V and Ni VI.

Since the weak lines are the astrophysically useful ones with regard to abundance determinations (see Section 6), the solar intensities of all identified Ni I lines were obtained from Moore's compilation (1966). A search was then made to find common upper levels between the observed BF lines and weak solar lines. It was required that the BF wavelengths be well isolated from neighboring lines in order to simplify the lifetime measurements.

3.4 DATA ANALYSIS AND CASCADING

Once a line had been chosen for light decay measurement, it was a straightforward task to measure the number of photons as a function of distance (and therefore of time) from the foil. A typical light decay curve for $\lambda 3566$ (a^1D_2 - $z^1D_2^o$) is shown in Figure 1 of Appendix C. The upper curve shows the counts obtained while observing at the peak of the Doppler-broadened line profile, corrected for all background effects. The background is comprised of two parts: dark counts due to thermal electrons emitted from the photocathode in the absence of any incident light and the continuous background measured approximately 10Å away from the peak of the line center, shown in the lower curve of the figure. The dark counts represent a continuous rate of 1-2 counts/sec, and the continuum counts away from the line contribute approximately 5 counts/sec near the foil but the continuum dies away very quickly as the detector is moved downstream from the point of excitation. This continuum background is a function of the wavelength of the line being studied. The counting rate at the line center varied between 30 and 70 counts/sec, depending on the line strength and on the efficiency of the detector at that particular wavelength.

After subtracting these background sources, a further correction was made to allow for those atoms scattered outside the field of view of the monochromator despite the demagnification of the condensing optics. This correction is discussed in Appendix E. At the maximum distance from the foil (approximately 5 cm), the scattering reduced the counting rate by typically 15%, an amount that was always less than the statistical uncertainty of the data.

To convert from distance to time, the velocity of the beam must be known. The energy lost in the foil was calculated using the results of Lindhard et al. (1963) for the nuclear stopping power, $(dE/dx)_n$, and interpolating the results of Hvelplund and Fastrup (1968) to find the electronic stopping power, $(dE/dx)_e$, for Ni in carbon. We have used the relation that $(dE/dx)_e = kE^{0.7}$. The value of k was obtained by interpolating the results of Hvelplund and Fastrup for the cases of ${}_{27}Co^{59}$ and ${}_{29}Cu^{65}$ incident on carbon. The two contributions to the energy loss were then subtracted from the known incident energy to find the post-foil beam velocity. A typical value for the energy loss was approximately 5 keV/μgm/cm^2 at an incident beam energy of 350 keV.

The velocity of the beam was also measured directly using a paraxial optical system as shown in Figure 2a. A front surface aluminized mirror was inserted into the beam path and oriented at an angle of 45^0 so as to reflect the light emitted in the direction of motion into the detector. The optical path of this light makes it quite simple to view the emitted light at both 0^0 and 90^0 with only a slight translation of the detector between the two measurements. The alignment was such as to accept only that light emitted within a narrow cone of a few degrees from the optic axis. Since light rays emitted at an angle θ with respect to the direction of motion of the particles will suffer a Doppler shift given by

$$\Delta\lambda(\theta) = -\beta\lambda_0 \cos \theta \qquad (3.1)$$

correct to first order in the small quantity β (where $\beta = 0.0463$

$(E_{MeV}/A_{amu})^{1/2})$, then those rays emitted at an angle as large as 8^0 will show a shift only 1% less than that of rays in the forward direction. No significant effect is thus introduced by the finite angular aperture of the paraxial system. The strongest line observed in the BF spectrum, $\lambda3619$, was used for this measurement. The results of the two scans at 0^0 and 90^0 are shown in Figure 2b. From the displacement, $\Delta\lambda$, between the Doppler shifted and the unshifted lines, we obtain the beam velocity directly using equation (3.1).

The results of Doppler shift measurements made at different incident energies and using different foil thicknesses are shown in Table 2. They indicate that the directly measured post-foil beam velocity was the same as that obtained by subtracting the calculated energy loss, within the uncertainty (± 40%) introduced by the tolerances on the foil thicknesses. There is no systematic error in the time scale used for the lifetime determinations.

To analyze our light decay curves, the observed data were fitted to a sum of exponentials

$$I(t) = \sum_{k=1}^{n} C_k \, e^{-t/\tau_k} \tag{3.2}$$

using a standard nonlinear least squares computer code. The differential equation that governs the population, $N_i(t)$, of a given upper level, level i, at a time t is

$$\frac{dN_i(t)}{dt} = -N_i(t) \sum_{j=1}^{i-1} A_{ij} + \sum_{k=i+1}^{m} N_k(t) \, A_{ki} \tag{3.3}$$

This expression neglects the effects of self-absorption in the beam and collisional deexcitation, which are negligible for the beam-foil light source. The time, t, after excitation is related to the distance, x, downstream from the exciter foil by $x = vt$, where v is the particle speed. In the absence of the second (cascade) term, equation (3.3) yields the familiar exponential decay law

$$N_i(t) = N_i(0)\, e^{-t/\tau_i} \tag{3.4}$$

where equation (2.6) has been used to replace the summation $\sum_{j<i} A_{ij}$. Figure 1 of Appendix C (λ3566) exhibits the behavior described by (3.4).

When there is only one higher level (level k) which repopulates the upper level of interest (level i), the decay scheme is then $k \rightarrow i \rightarrow j$ with $E_k > E_i > E_j$. The population of level i as a function of time is

$$N_i(t) = N_i(0)\, e^{-t/\tau_i} \left\{1 + \frac{A_{ki} N_k(0) \tau_i \tau_k}{N_i(0)[\tau_i - \tau_k]}\right\} + \frac{A_{ki} N_k(0) \tau_i \tau_k}{(\tau_k - \tau_i)}\, e^{-t/\tau_k} \tag{3.5}$$

The most general solution to (3.3) has been shown by Curtis (1968) to be a sum of many exponentials; the number of terms depends on how many of the $N_k(t)$ are non-vanishing.

The quantity observed in a transition from level i to level j $(E_j < E_i)$ at λ_{ij} is the intensity $I_{ij}(t)$ in photons/sec, defined by

$$I_{ij}(t) = N_i(t)\, A_{ij} \tag{3.6}$$

The number of terms (n) used in (3.2) was varied from one to three to find the best fit to the observed intensity. Some of the decay curves were fit very well by a single exponential, as was the case for λ3566 shown in Figure 1 of Appendix C. Other decay curves required two exponentially decaying functions to obtain a good fit. An example of this type is shown in Figure 3. The data points have had all the sources of background subtracted, and the solid curve represents the sum of the two dashed curves. The transition wavelength is λ3492 ($a^3D_2 - z^3P^o_1$) . When a third exponential function was added to the fitting routine, no significant improvement was obtained, and the lifetime of the component with the largest intensity was not changed by more than 3% from the value obtained in the double exponential fitting procedure. The uncertainties in the fitted parameters increased as more exponential terms were added since the number of degrees of freedom (= number of data points - number of parameters) decreased.

Curtis et al. (1970) have defined the replenishment ratio, R(t), which can be expressed in terms of the fitted parameters C_k and τ_k by

$$R(t) = \sum_{k=2}^{n} (1 - \frac{\tau_1}{\tau_k}) C_k \, e^{-t/\tau_k} \Big/ \sum_{k=1}^{n} C_k \, e^{-t/\tau_k} \qquad (3.7)$$

which takes into account both the relative populations of the cascading levels and their lifetimes; these two factors together affect the reliability of analysis of light decay curves. R(t) is essentially the ratio of the cascade repopulation to the decay depopulation. Therefore R(t) is identically zero for a single exponential decay.

The cascading is simply characterized by the replenishment ratio, R(0), at $t = 0$ which, for a double exponential fit, becomes

$$R(0) = (1 - \frac{\tau_1}{\tau_2})(\frac{C_2}{C_1 + C_2}) \tag{3.8}$$

For the single cascade case described by equation (3.5), with $i = 1$ and $k = 2$, we obtain

$$N_1(t) = N_1(0) \{[1 - \frac{C_2}{C_1 + C_2}]e^{-t/\tau_1} + (\frac{C_2}{C_1 + C_2})e^{-t/\tau_2}\} \tag{3.9}$$

To see the relevance of the quantity $R(0)$, we can find the slope of the decay curve at $t = 0$, expressed in terms of $R(0)$. Differentiating (3.9), we obtain

$$\left.\frac{dN_1(t)}{dt}\right|_{t=0} = - \frac{N_1(0)}{\tau_1} [1 - R(0)] \tag{3.10}$$

If $R(0) << 1$, then the level is essentially unreplenished. The observed intensity will vary as a single exponential of mean life τ_1, and cascade effects are negligible. If $R(0) \sim 1$, repopulation causes the intensity variation to be multi-exponential and cascade effects are large. If $R(0) > 1$, the decay curve will rise initially and cascade effects will dominate the observed intensity. All of the decay curves which we observed for Ni I were of the type $R(0) << 1$.

The Ni I lines chosen for light decay measurements are listed in Table 3. The results of individual measurements are given with the incident energy of the beam and the foil thickness. For two of the upper levels, the mean lifetime has been determined by observing the decay curve for two different branches. A representative value of R(0) has been given for each upper level. The range of incident energies used was 282-486 keV, and the foil thickness was varied from 5 to 20 $\mu gm/cm^2$, although most of the data were taken with 10 $\mu gm/cm^2$ foils. No systematic variation of the mean lives with either the foil thickness or the beam velocity was observed.

3.5 DISCUSSION OF RESULTS

Our measured lifetimes are longer than those calculated from the tabulation of Corliss (1965) by a factor that ranges from 1.6 - 5.5. This discrepancy with earlier investigations, and in particular with the results of Corliss and Bozman (1962), is similar to the recent trend found in other iron group elements. The possible reasons for this trend have been discussed at great length, most recently by Takens (1970), and will not be repeated here.

Brand *et al*. (1973) have measured lifetimes for 7 of the levels for which we have values. They have used the beam-foil technique with incident ion energies in the range 65-100 keV. All of their values are longer than our measured lifetimes by almost a constant 14%. They also measured the beam velocity directly using the Doppler shift technique described in Section 3.4. Particle straggling in the foil renders this method more difficult at such low velocities. Kay (1972) has shown that the steepest slope of an intensity decay curve on a semilogarithmic plot gives an upper bound on the mean life, τ . The implication of his result is that if lifetime measurements are in error, then they will be too long rather than too short. Since our BF lifetimes are shorter than those of Brand *et al*., and since both measurements give at worst upper limits for the true value of the mean lives, then the differences between Brand's values and those obtained in this thesis suggest that the former are in error. Cocke (1974) has recently stated that there is a possibility that the Doppler shift method as used by Brand was incorrect. The velocity determinations were performed <u>after</u> the lifetime measurements and required that data be accumulated over time periods of about 30 minutes. Cocke believes that the thickness of the foils increases significantly in their vacuum of approximately 10^{-5}torr over such time intervals. If the foils were actually thinner than the subsequent Doppler shift measurement indicated, then the particles would have been moving at a larger velocity during the lifetime measurement, and Brand's lifetimes would all be too long. Cocke estimates that the correction required to convert to the correct time scale for the Ni work amounts to 10%-15%, which would bring Brand's values into close agreement with our results. It is important to note that all the comparisons of the CIT data with the results of Brand <u>et</u> <u>al</u>. are for levels at low excitation energies (3.5 - 4.0 eV). This point will be discussed later in this section with regard to cascading.

The measurements of Marek (1972) are phase-shift lifetime measurements which are based on the resonant light scattering process. They should be free of cascading complications. According to Cunningham and Link (1967), phase-shift measurements are capable of giving absolute lifetimes with ±3-7% accuracy under favorable circumstances and when performed properly. Marek's quoted uncertainties vary between ±2 and ±5%. For two of the three levels which have been measured by both Marek and CIT, the agreement is very good. For the

$z^3P_2^o$ level, τ_{CIT} is longer than τ_M (Marek) by about 20%. A light decay curve for λ3524 is shown in Figure 4. It may be that cascading is influencing our measured lifetime although the replenishment ratio, R(0), is only $0.05 \ll 1$. It should be noted here that although $R(0) = 0.15$ for the λ3492 transition (upper level $z^3P_1^o$) shown in Figure 3, our measured lifetime is in excellent agreement with Marek's value.

The fact that our measured lifetime for the $z^3P_2^o$ level is longer than Marek's immediately raises the suspicion of cascading which is the basic weakness of the BF method. We have consequently gone to some effort to investigate this discrepancy. A search was made to see which of the known transitions (from the RMT) into any of the upper levels for which lifetimes were measured were present in the survey spectrum (see Appendix C). The λ4855 transition which repopulates the $z^3P_2^o$ level was seen on the original spectrogram. None of the other transitions which feed either the $z^3P_2^o$ level or any other level studied were observed with a significant intensity.

The λ4855 transition originates in the e^3P_2 level. We have measured the lifetime of this level. The result, tabulated in Table 3, is 12.4 ± 2.0 ns. Since this lifetime is essentially the same as that value obtained for the $z^3P_2^o$ level (12.2 ± 2.5 ns), we should obtain the solution that corresponds to (3.5) for the case $\tau_i = \tau_k = \tau$. Taking the limit $\tau_k \rightarrow \tau_i$, we obtain

$$N_i(t) = N_i(0)\, e^{-t/\tau} \left[1 + \frac{N_k(0)\, A_{ki}\, t}{N_i(0)}\right] \tag{3.11}$$

In (3.11), i represents the $z^3P_2^o$ level and k the e^3P_2 level. The solution for τ_i close to τ_k but not exactly equal to it can be obtained trivially from (3.5) and is not particularly enlightening.

We must now appeal to the actual physical boundary conditions of the BF spectrum to pursue the discrepancy. Using the relative efficiency calibration of the McPherson detector system as a function of wavelength (performed in the course of the work described in Appendix B), the relative intensities of the two lines (λ3524 and λ4855) were found to be $I(\lambda4855)/I(\lambda3524) = 0.095$ when observed at the foil ($t = 0$). Using (3.6) and substituting in (3.11) yields

$$N_i(t) = N_i(0)\, e^{-t/\tau}\{1 + \frac{At\ I(\lambda4855)}{I(\lambda3524)}\} \tag{3.12}$$

where A is the transition probability for the λ3524 transition. Using our measured value for the relative intensities, and putting $A = 0.8 \times 10^8 \mathrm{sec}^{-1}$ ($A_{CIT} = 0.72 \times 10^8 \mathrm{sec}^{-1}$ and $A_{Marek} = 0.86 \times 10^8 \mathrm{sec}^{-1}$) we obtain

$$N_i(t') = N_i(0)\, e^{-t'/\tau'}\ (1 + 0.0076\ t') \tag{3.13}$$

where t' and τ' have the units of nanoseconds.

The expression (3.13) should then represent the observed decay curve for λ3524 as a function of time if the e^3P_2 level is the only level which significantly repopulates the $z^3P_2^o$ level (via the λ4855 transition). If there is another level which also cascades into the $z^3P_2^o$ level, then we should add another exponentially decaying term to the right side of (3.13). Functions of the form

$$N_i(t') = C_1 e^{-t'/C_2}(1 + t'/C_3) + C_4 e^{-t'/C_5} \qquad (3.15)$$

where the C_j are arbitrary constants, were fitted to the data. The computer program found a fit to the data but the uncertainties assigned to the fitted parameters were generally larger than the values given for the parameters themselves in the case of C_2, C_3, and C_4. None of the $\lambda 3524$ light decay curves were fit as well by functions of the form (3.14) as by a simple two exponential function (equation (3.2) with $n = 2$).

We have also attempted to reconstruct our light decay curve on the assumption that Marek's value of 9.91 ns is the correct mean life of the $z^3P_2^o$ level and that $\lambda 4855$ is the only cascading transition which feeds this level. We used our observed intensity ratio $I(\lambda 4855)/I(\lambda 3524) = 0.095$ and $A = 0.8 \times 10^8 \text{sec}^{-1}$ as before. Letting τ_k vary from 9.9 - 16 ns, the constructed curves resemble single exponential decays. Fitting these constructed curves to a single exponential yields $\tau_i = 10.5 - 10.7$ ns for the range $9.9 \text{ ns} < \tau_k < 16 \text{ ns}$. Thus we cannot reconstruct our observed light decay curves with Marek's lifetime for the $z^3P_2^o$ level.

It is interesting to ask what the second (cascading) term in equation (3.2) represents for the case of $n = 2$ which we have used in fitting our data. From Figure 3, it is clear that we must observe for a time long compared to the fast time constant, τ_1, to determine the slow (or cascade) lifetime τ_2 well. For all of the lines encountered in this work, it was not possible to observe far enough downstream to obtain an accurate value for τ_2 since the signal-to-noise ratio becomes too small at about $t = 4\tau_1$. The parameters τ_2 and C_2 are not well determined in the fitting routine, although the values of C_1 and τ_1 are "unique" to within ±1% regardless of the values of C_2 and τ_2 found in the fit. The data were analyzed by the computer program for several initial guesses at the parameters, and the final values for τ_1 and C_1 were always essentially identical. The various fitted values of τ_2 and C_2 are of course not independent and the calculated value of $R(0)$ was the same for different fits to the same data. We cannot exclude additional exponential terms from expression (3.2) higher than $n = 2$ with smaller C_k , but again τ_1 is not affected.

We conclude that little physical significance can be attached to the fitted values of the cascade lifetime (τ_2 in (3.2)). This is not surprising in view of the complexity of the solution to (3.3) for the general case of many cascading terms.

We have also attempted to estimate the $z^3P_2^o$ lifetime by comparing the summed intensities of all branches from this level with the corresponding sum for the branches from the $z^3P_1^o$ level. The result was inconclusive but the method can be useful in some instances and is described in Appendix F .

We have examined other phase-shift measurements of optical level mean lives in search of a possible source of error in Marek's method. Cunningham and Link (1967) have measured a lifetime in each of Na, Tl, In and Ga, with the quoted uncertainties in the range ±1.7 - 5.2%. Demtröder (1962) has measured the same lifetimes in Tl and Ga and gives his uncertainties as ±3.5% and ±2%. However, the two measurements differ by 13% and 27% respectively. Hulpke et al. (1964) have measured the Na and In lifetimes also by the phase-shift method. Although they agree on the Na level (upper level of the Na D lines), their measurement of the In level lifetime, with a quoted uncertainty of ±3.5%, disagrees with the value of Cunningham and Link by 13%. Marek states that his apparatus is similar to that of Demtröder, but the two works were not performed with the same experimental facilities. Because other phase-shift measurements show discrepancies among themselves that are much larger than the quoted uncertainties in the individual lifetime determinations, we do not know how reliable Marek's uncertainty of ±2-5% is likely to be. It is unlikely that the lack of agreement between our result and that of Marek for the $z^3P^o_2$ level represents a systematic error in the beam-foil measurements, since the two additional cases of overlap are concordant.

For the levels at high excitation energies, the lines used for light decay analysis were weak as can be seen from Table 2 of Appendix C. The beam dependent background, observed on both sides of the lines was of the order of 25% of the peak intensity at the line center at the foil, making its subtraction from the raw data more difficult. It is likely that in the cases of the e^3P_2 and e^5F_5 levels that the non-zero values of R(0) represent a contribution from the beam dependent background rather than from a higher cascading level. There are only two possible levels that can feed the e^5F_5 level, and the shorter of the two wavelengths is greater than 4μ. Since the transition probability, A_{ij}, is proportional to λ_{ij}^{-3} (see equation (2.1)), the A-value for these possible cascades will be negligibly small, making the contribution of the cascade term in equation (3.5) of little importance. Similarly, the e^3G_5 level is fed by a single higher level with a transition wavelength > 6μ , the e^3P_2 level is fed by five transitions with $\lambda > 3.8\mu$, and the g^3F_3 level has no levels above it that can decay to it via E1 transitions.

Although we cannot be sure that cascading is not affecting our measured lifetimes, particularly for the low-lying odd parity levels, there is good reason to believe that our measurements are not in error:

(i) there was no evidence that the measured lifetimes changed as a function of the foil thickness and the incident beam energy, as was found by Martinez-Garcia (1971a) for low-lying levels in Fe I;

(ii) none of our measured light decay curves exhibited initially increasing (positive) slopes at the origin ($t = 0$);

(iii) the agreement with the phase-shift measurements of Marek (1972) is satisfactory except in a single case; and

(iv) the abundance calculated from transitions originating in low-lying levels (see Section 6.5) is the same as that for branches from high levels.

3.6 UNCERTAINTIES IN THE LIFETIME MEASUREMENTS

For those lines where R(0) is significantly different from zero, a larger uncertainty has been assigned to the measured lifetime, as indicated in Table 3. This is to take account of the possible influence of cascades as discussed in Section 3.4. The statistical uncertainty assigned to each parameter in the data analysis computer program for individual measurements was of the order of a few percent. In those cases where $R(0) \neq 0$, the uncertainty is somewhat larger since more parameters are used in the fitting procedure. The uncertainty associated with the reproducibility of the measured lifetimes made with different foil thicknesses and with different incident ion energies was almost always less than ±10%. The results of the Doppler shift measurements indicate that the uncertainty in the beam velocity, including the ±40% uncertainty in the foil thickness, is of the order of ±2%.

The uncertainties are given in Table 3 for each of the lifetimes. They range between ±10-20%, and on the average are ±15%. The uncertainty in the lifetime will be combined with uncertainties in the branching ratios for individual lines (see Section 4.6) to determine an overall uncertainty in the absolute transition probabilities.

4. TRANSITION PROBABILITIES

4.1 INTRODUCTION

Since the lifetime of an excited atomic level is related to the absolute transition probabilities for all the channels out of that level by (2.6), then a measurement of the branching ratio, R_{if} , where

$$R_{if} = \frac{I_{if}}{\sum\limits_{f<i} I_{if}} \tag{4.1}$$

yields A_{if} . In (4.1), I_{if} represents the intensity of light emitted at the wavelength λ_{if} in photons/sec. Using the relation

$$I_{if} = N_i A_{if} \tag{4.2}$$

in (4.1) gives us the relationship between the measured lifetime, τ_i , and the measured branching ratio, R_{if} ,

$$A_{if} = \frac{R_{if}}{\tau_i} \tag{4.3}$$

Figure 4 shows the possible decay channels for the e^3G_5 level in Ni I. The transition wavelengths can be found in Table 12. The method of level designation is the same as in Moore (1971). The vertical height of each level represents its excitation energy above the ground state in units of kilokaysers (1 kayser = 1 cm^{-1}).

4.2 BRANCHING RATIO MEASUREMENTS

A schematic diagram of the 5 meter Paschen-Runge spectrometer used for the branching ratio (BR) measurements in the visible region

(λ < 8500Å) is shown in Figure 6. The calibration of the relative detection efficiency of the optical system is described in Appendix D.

The hollow cathode source used in this work was similar to the sources used by Martinez-Garcia (1971a), Smith (1972) and Cocke _et al._ (1973) in their studies of Fe I, Fe II and Cr I respectively. The details of the construction of the source are clearly illustrated in the works of Martinez-Garcia and Smith and will not be repeated here. In the case of Ni, the cathode was a cylinder, approximately 2 cm long and 5 mm in diameter, of spectroscopically pure Ni (99.99% pure) with a 3 mm central canal. Tolansky (1947) has described the behavior of these sources; atoms of the cathode material are sputtered off by collisions of the carrier gas ions with the cathode. Ionization and excitation occur by ion and electron bombardment. The nickel atoms constitute an impurity in the carrier gas. Neon, argon or helium were used as carrier gases because of the few lines that noble gases emit in the visible region. Also, the use of different carrier gases eliminated the possibility of blends in the Ni and gas lines. Conditions in the discharge were optimized by varying the voltage, current and gas pressure to produce the brightest and steadiest glow. The source was typically operated with a gas pressure of 2-3 torr and a discharge current of about 150-300 ma at a voltage of about 450-500v. The gas flow rate was about 3-4 cm^3/min.

The cathode canal was imaged onto the entrance slit (usually 40μ x 1 mm) of the spectrometer using a concave mirror 10 cm in diameter with a focal length of 52 cm. The image of the source was magnified by a factor of 4 to ensure that the entrance slit of the spectrometer was smaller than this image.

The Paschen-Runge spectrometer was equipped with two detecting channels. One channel, the monitor channel, was set on a strong, unblended line from the upper level under investigation and continuously monitored the excitation of that level in the source. The scanning detector then was scanned across each line (or branch) from the same upper level to measure its relative intensity. The scanning channel, a refrigerated RCA C31034 photomultiplier tube with fixed exit slits 20μ x 2 mm, could be moved anywhere along the track. The track is located on the Rowland circle of the apparatus, as discussed in Born and Wolf (1965). The scanning channel detects the spectrum on the left of the grating normal (see Figure 6) that is enhanced by the grating blaze. The monitor channel detector, an EMI 9783B photomultiplier tube, detected the spectrum on the right of the normal. This arrangement avoided the physical interference of the two detectors when two branches with almost the same wavelength were to be compared. The monitor exit slits were variable, and usually set at 100μ since an isolated line was chosen as the monitor wavelength.

The reciprocal dispersion of the spectrometer was 3.2Å mm at λ5000 in first order, and the observed full width at half maximum (FWHM) of the spectral lines was about 135 mÅ. The resolution was found to be sufficient for these measurements although it was not the maximum resolution attainable. The 40μ entrance slit width and 20μ exit slit width gave a trapezoidal line shape so that the peak height was proportional to the line intensity.

A two-channel strip chart recorder displayed the output current from both detectors simultaneously. The branching ratio could be read directly from the chart after correcting for the detection efficiency of the scan channel. The detection efficiency of the monitor channel need <u>not</u> be known.

Four transitions encountered in this study were located in the wavelength region $\lambda > 8500\text{Å}$. As can be seen in Figure 6, this region was inaccessible using the Paschen-Runge apparatus due to the geometry of the entrance slit.

In order to measure the relative strength of these red branches, we used the same McPherson 218 monochromator as used in the lifetime measurements (see Section 3.2) in place of the Paschen-Runge spectrometer. The monochromator was equipped with a refrigerated HTV R406 photomultiplier tube having an S-1 spectral response. A 600 line/mm grating blazed at λ10,000 was installed to detect the near infrared spectrum in first order. The relative detector efficiency was measured in this wavelength region in the manner described in Appendix D.

Some portions of the efficiency calibrations (see Appendix D) and BR measurements required the use of filters to eliminate scattered light and photons of unwanted (second and third) orders. Glass and gelatin color filters* were used. The transmission of all the filters used in this work was always greater than 70% at the wavelengths where they were employed. Although the filters had been calibrated for transmission as a function of wavelength by Martinez-Garcia (1971a)

---

*Corning Glass Works, Optical Products Dept., Corning, N.Y. 14830.
SCHOTT - Jena Glaswerk Schott + Gen., Mainz, West Germany.
Eastman Kodak Company, Rochester, N.Y. 14650.

and Smith (1972) in their study of Fe I and Fe II respectively, the calibrations were checked again in the course of the Ni measurements. The transmission was measured directly by observing the change in intensity of spectral lines when the filter was introduced in front of the detector. Several nearby lines were observed with the filter in and with the filter out. The correct transmission was obtained by taking the maximum ratio of the filter-in signal divided by the filter-out signal. The presence of second or third order lines occurring at the wavelength of a first order line would yield a transmission value less than its correct value; thus the choice of the maximum transmission for any line in the region of interest as representing the correct filter transmission.

Since the filters were used often in the course of the measurements, and since repeated measurements of their transmission yielded results in agreement at all wavelengths to within ±3%, the uncertainties associated with the transmission of a filter can be neglected (see Section 4.6).

Since the McPherson spectrometer has only one detection channel, it was decided to use the ABABA... method to compare the intensity of a transition at λ_A relative to that at λ_B , where both λ_A and λ_B are from the same upper level. One of the branches (λ_A or λ_B) had already been measured with the Paschen-Runge spectrometer system and was located in the visible region. Previous experience with the measurements in the visible had shown that the short term fluctuations in the hollow cathode source were not sufficiently large to hinder the ABABA... technique.

Preliminary scans in the current mode gave no indication of the near infrared lines we were seeking. We then employed standard pulse-counting techniques to increase the signal-to-noise ratio in order to obtain sufficiently small upper limits for the strengths of the red lines to justify their neglect in the sum (2.6).

The region around the RMT wavelength was scanned continuously by the McPherson monochromator at a speed of 2Å/min. The multi-channel analyzer, operated in the time mode, was stepped along at a rate of 4 sec/channel, continuously accumulating counts. Repeated scans were made alternately over the red line and over the visible line used for comparison. The data were stored separately in the analyzer. The wavelength scale in the near infrared was calibrated very accurately and reproducibly using second and third order Ni I and carrier gas lines that could be observed in the hollow cathode spectrum when the filter was removed. The filter used for these measurements was a Corning 2-64 filter with a short wavelength cutoff at λ6700. Since the comparison wavelength and the infrared wavelength usually differed by about a factor of two, a detector with a wide spectral response was necessary.

4.3 SEARCH FOR BRANCHES

As discussed in Section 2, the Multiplet Tables of Moore (1945,1950) were used to find the classified transitions that depopulate the levels for which we have measured lifetimes. To these were added any decay modes seen by other observers in the laboratory or in the sun. Table 4 lists all the branches from each of the upper levels studied, with the corresponding lower level designations and the excitation potentials (in cm^{-1}) from Moore (1971). The source of those wavelengths which do not have multiplet numbers is given in the caption to Table 4.

4.4 RESULTS OF BRANCHING RATIO MEASUREMENTS

The results of the branching ratio measurements for the 11 levels whose lifetimes had been measured (see Section 3) are discussed for each level individually. Branching ratios were also measured for the two levels ($z^5F^o_4$ and $z^3F^o_4$) whose lifetimes had been measured by Marek (1972) in order to obtain data for the empirical curve of growth as discussed in Section 5.4.

The absolute transition probabilities were calculated from the measured quantities using equation (4.3); the values of gf (and of log gf) were obtained using relation (2.5). The results are tabulated separately for each upper level. Also given are the branching ratios calculated from the results of Corliss and Bozman (1962) for comparison, and the log gf's taken from column 15 of Corliss (1965). The uncertainties are discussed in Section 4.6.

4.4.1 LEVEL $z^3D^o_2$

Table 5 shows the results of the branching ratio measurements for this level. Ni I has two transitions at λ3548.185, one from the $z^3D^o_2$ level and one from the $z^5F^o_1$ level. We have assumed that the contribution to our observed intensity for the branch from the $z^3D^o_2$ level was one-half of the total observed intensity, with an uncertainty of a factor of two. This uncertainty contributes an additional ±2%

uncertainty to all of the other branching ratios listed in Table 5. The relative strength of the two coincident lines is difficult to measure either in absorption or emission since they originate in upper levels having the same excitation energy. The same problem is applicable to their relative intensities in the solar spectrum.

4.4.2 LEVEL $z^1F^o_3$

All the decay branches are listed by Moore (1945) and are shown in Table 6. The upper limit for the strength of λ11196 was found by comparison with λ5709, a 1% branch, using the method described in Section 4.2. The near infrared transition at λ11196.70 has been observed only by Fisher et al. (1959) using an arc source and a lead sulfide detector. He observed a Ni line at λ11196.75. There is no evidence for the presence of this line in the solar spectrum. Its strength is negligible in comparison with the strengths of those lines in the visible. The upper limit was not included in the calculation of the A_{ij}'s for the other branches.

4.4.2 LEVEL $z^3P^o_2$

Table 7 lists the results for all the branches from this level. All branches are classified by Moore; all lie in the visible region and were observed in the hollow cathode source. One interesting feature of this level is the decay branch at λ7714. It is clear that Moore's wavelengths are not always the exact wavelength. Table 18 lists the observed wavelength for this transition found by other authors using various sources. It can be concluded with reasonable certainty that the true wavelength in air of this transition is closer to λ7714.31 than to the value λ7714.27 given by Moore (1945).

4.4.4 LEVEL $z^3P_1^o$

The results of the branching ratio measurements for all of the branches from this upper level are given in Table 8. All decay branches are classified by Moore and were visible in the hollow cathode spectrum. No specific problems were encountered during the measurements since all the branches are in the visible region.

4.4.5 LEVEL $z^3F_3^o$

Table 9 lists the results of the branching ratio measurements for this level. The predicted infrared transition at λ13849.64 has been observed only by Fisher _et al_. (1959) in the laboratory at λ13849.49. There is no evidence for its presence in the solar spectrum. No attempt has been made here to measure the strength of this transition since it is outside the range of our detector. Using the measured branching ratios for the other transitions from this upper level to lower levels of the same configuration, and the λ_{ij}^{-3} dependence of A_{ij} (equation (2.1)), we can estimate the magnitude of the branching ratio for λ13849. The estimated value is approximately 0.005% (upper limit). We have neglected this branch in calculating the A_{ij}'s for the other branches.

4.4.6 LEVEL $z^3F_2^o$

Table 10 shows the results for all the branches from this level. The transition at λ6716.14 has been listed by Corliss (1965), but was not observed in our hollow cathode spectrum. Its possible presence in the solar spectrum is obscured by a nearby Fe I line at λ6716.24 (RMT No. 1225).

4.4.7 LEVEL $z^1D_2^o$

The results of the measurements for this upper level are shown in Table 11. All transitions were seen in the hollow cathode spectrum and there were no particular complications to the branching ratio measurements. The branch at λ6364 has not been observed in the solar spectrum prior to the Kitt Peak Preliminary Solar Atlas (see Table 21).

4.4.8 LEVEL e^3G_5

Table 12 lists the allowed decay branches from this upper level. The decay scheme is also shown in Figure 5. There are only eight transitions classified by Moore. Of these eight, we observed only six in the hollow cathode spectrum used in this work, and upper limits were obtained for the strengths of λ4849 and λ4565. Neither of these two transitions appears in the solar spectrum, and the upper limits have been neglected in obtaining A_{ij}'s for the other branches. Mohler (1955) has observed an infrared transition in the solar spectrum at λ16945.47. The predicted location of this line is at λ16945.28. We were not able to measure the strength of the line since it is outside the range of our detector. Using Mohler's value of 22 mÅ for the equivalent width, and the Ni I empirical curve of growth derived in this experiment (see Section 5.4), an upper limit of approximately 1% is obtained for the branching ratio of λ16945. The upper limit has not been included in calculating the transition probabilities for the other branches. There is definitely a line in the solar spectrum at λ4633.037. This line was seen in our hollow cathode discharge, and its identification as a Ni I line has now been confirmed (see Appendix G).

4.4.9 LEVEL e^5F_5

Table 13 lists the branching ratio results for this level. The transition at λ6452 was not seen in the hollow cathode source nor is it observed in the solar spectrum.

4.4.10 LEVEL g^3F_3

The results for the many branches from this upper level are listed in Table 14. Upper limits were obtained for the strengths of the near infrared branches (λ > 9500Å) by the method described in Section 4.2. Figure 7 shows the results of the search for one of these branches, λ10061, using the branch at λ4838 as a comparison for normalization. There is no evidence for the presence of a transition at λ10061, and suitably small upper limits were obtained by counting for a sufficiently long time. The branch at λ10226 is not listed by Moore (1945) but Swensson _et al_. (1970) have seen a weak line in the sun at this wavelength (see Table 4) which they attribute to Ni I. This line was not observed in the hollow cathode spectrum, and its strength has been neglected.

The branch at λ4230 was not seen in our hollow cathode source. Moore (1966) finds a line in the sun at λ4230.402 (W^{NBS} = 2.5 mÅ) which she identifies as a Ni I line. We have examined the Kitt Peak Preliminary Solar Atlas (see Section 5.2) and find a line at λ4230.381

with $W^{KP} = 1.87$ mÅ. The predicted location of this line (see Section 2) is at λ4230.379. Using our curve of growth (see Section 5.4) and the Ni abundance found in this work (Section 6), we estimate the value of log gf for λ4230 to be -2.49 with $W = 1.87$ mÅ. This transition is not listed by Corliss (1965). Our measured upper limit of log gf < -2.12 is not in disagreement with the estimated value.

The strong branch (R = 17.7%) at λ5371 is not classified by Moore (1945), thus initiating the search for other unclassified lines that were not weak, as described in Section 2. The λ5371 transition was, however, the only transition omitted from the Multiplet Table which did not have a negligible strength.

The branching ratio for the λ4450.13 transition is given a large uncertainty because of the blend with another Ni I line (RMT No. 236) at λ4450.301. Both lines are very weak, and it was not possible to resolve them by using narrower slits since the resultant decrease in intensity made measurements above the background level impossible.

The contributions of those branches for which only upper limits on the strengths were obtained were not used to compute the A_{ij}'s for the other branches.

4.4.11 LEVEL e^3P_2

Table 15 lists the results of the branching ratio measurements for this upper level. The transitions at λλ4444, 4597, 5262 and 6666 are listed by Corliss (1965) but not by Moore (1945) in the Multiplet Table. We were only able to observe the λ5262 branch. Its possible presence in the solar spectrum is obscured by a nearby strong Fe I line. The branch at λ7960 was listed by Harrison (1939) but does not appear in his more recent compilation (Harrison 1969). The strengths of those branches observed by Mohler (1955) with $\lambda > 1.5\mu$ were not measured since the wavelengths were outside the range of our detector. We have estimated their strength using Mohler's observations and our empirical curve of growth (see Section 5.4), and their contribution to the sum (2.6) can be neglected. We have not included the upper limits in the calculation of the A_{ij}'s for the other branches.

4.4.12 LEVEL $z^5F^o_4$

The branching ratio measurements for the transitions from this level were normalized using the lifetime measurement of Marek (1972). The corresponding gf values were used only as a consistency check to supplement data for the empirical Ni I solar curve of growth (see Section 5.4). The results are shown in Table 16.

4.4.13 LEVEL $z^3F^o_4$

The branching ratio results are shown in Table 17. As with the $z^5F^o_4$ upper level, the lifetime for this level is taken from Marek (1972) and the derived gf values used for the same purpose. His lifetime for this level was also used in conjunction with the CIT lifetimes for the $z^3F^o_2$ and $z^3F^o_3$ levels to investigate the discrepancy in the $z^3P^o_2$ lifetime measurements as described in Appendix F. Brand *et al.* (1973) have also measured the lifetime of the $z^3F^o_4$ level using the beam-foil technique. In view of the discrepancies between their measured values and those measured in this thesis (see Section 3.5), we have chosen to use

Marek's result. In this instance, Marek's value is only 11% smaller than the value of Brand _et al_.

4.5 SELF-ABSORPTION

In any laboratory spectral source, there is always the possibility that some lines, in particular resonance emission lines, will be self-absorbed. Photons that are emitted in a transition from an upper level, i , to a lower level, f , may be absorbed by atoms in level f before the photons can escape from the source. If level f is the ground state, the number of atoms, N_f , in state f can be large. The number of upward transitions (or absorptions) from f → i, I^a_{fi} , is

$$I^a_{fi} \propto N_f \; B_{fi} \; I_{if}(\lambda_{if}) \tag{4.4}$$

where I_{if} is the intensity of radiation of wavelength λ_{if} and B_{fi} is the absorption coefficient defined in (2.3). If I_{if} is the emitted intensity of a spectral line at λ_{if} as defined in (4.2), then the observed intensity, I^{obs}_{if} , outside the source including the effect of self-absorption is

$$I^{obs}_{if} = N_i \; A_{if}(1 - k_{if} \; A_{if} \; N_f \; \alpha_f) \tag{4.5}$$

where $k_{if} = g_i \; \lambda^3_{if}/(8\pi h g_f)$ is the factor in (2.3) relating B_{fi} to A_{if} and α_f is a constant which gives some measure of the self-absorption by atoms in level f . Self-absorption will decrease the observed intensities of strong lines more than that of weak lines, causing a systematic error in the direction to make the measured branching ratios for strong lines too small and those for weak lines too large.

In the hollow cathode source described in Section 4.2, the intensities of the emission lines were observed to depend on the source operating conditions. Variations in the discharge current and the gas pressure produced changes in the excited state populations.

We have observed the change in the relative intensities of both a strong line λ_{i1} and a weak line λ_{i2} from the same upper level as a function of the source operating parameters. Using (4.5), we obtain for the relative intensity ratio

$$\frac{I_{i1}^{obs}}{I_{i2}^{obs}} = \frac{A_{i1}(1 - k_{i1}\, A_{i1}\, N_1\, \alpha_1)}{A_{i2}(1 - k_{i2}\, A_{i2}\, N_2\, \alpha_2)} \tag{4.6}$$

which is a function of the lower level populations N_1 and N_2 only. Unfortunately, for the case of Ni I the large J-value of the ground state (a^3F_4) inhibits strong transitions from excited states. We have observed the change in the relative intensities of the strong line λ_{i1} 3619.392 and the weak line λ_{i2} 5709.559. Both transitions originate in the common upper level $z^1F_3^o$ (see Table 6) and the measured branching ratios differ by a factor of 645. When the discharge current was varied in such a way as to change the intensity of each line by about a factor of 2 (for instance, by increasing the discharge current from about 150 ma to about 230 ma), the resultant decrease in the observed ratio (4.6) was less than 10%.

In order to be able to observe changes in relative intensity ratios for larger intensity variations, we observed the intensities of

λ_{i1} 3619.392 as before and λ_{i2} 3315.663. Table 6 shows that the observed branching ratios differ by about a factor of 15. Now the intensities were varied by a factor of 4-5 by increasing the discharge current and the gas pressure. The intensity ratio (4.6) was the same to within ±10%, which is approximately the uncertainty in reading the individual intensity values.

Although the above observations should be made for branches from all of the levels studied, the results of Martinez-Garcia (1971a) and Smith (1972) had both indicated that there was no self-absorption for the hollow cathode source in their studies of Fe I and Fe II respectively. Further investigation of this effect was not undertaken in the light of the comparison of our branching ratios with those of other workers for five of the strongest lines in the Ni I spectrum. Columns 3 and 4 of Table 19 show the CIT results and those taken from Marek (1972). Marek's results were obtained by taking a mean of the results of Corliss and Bozman (1962), van Driel (1935), King (1948), Allen and Asaad (1957), Bell *et al.* (1966), Garz *et al.* (1970) and Laurent and Weniger (1970). In actual fact, Marek's quoted values are only *upper limits* for the branching ratios since in most cases the weakest branches from the upper levels involved were not measured. *All* of our branching ratios for these strong lines are larger than Marek's values by 5.8% ± 2.4%, where the uncertainty is simply the sample variance from the individual values. If self-absorption were affecting our results, then we would have measured branching ratios that were too small for the strong lines, which does not appear to be the case from the values given in Table 19. Our branching ratios for weak lines would be too large, and the abundance derived from the gf values (see Section 6) would then be too small. The results of the abundance determination in Section 6 suggest that self-absorption has not affected our results for the weak lines.

4.6 UNCERTAINTIES IN THE TRANSITION PROBABILITIES

Since the absolute transition probabilities are obtained from the measured lifetimes and branching ratios using equation (4.3), then the fractional uncertainty ΔA_{if} in A_{if} is given by

$$\frac{\Delta A_{if}}{A_{if}} = \sqrt{\left(\frac{\Delta\tau_i}{\tau_i}\right)^2 + \left(\frac{\Delta R_{if}}{R_{if}}\right)^2} \tag{4.7}$$

which is the same as the fractional uncertainty in gf, from equation (2.5). The uncertainties in the lifetimes are given in Table 3.

The observed relative intensity, I_{if}, of a given branch, λ_{if}, from upper level i is

$$I_{if} = \frac{i_s(\lambda_{if})}{i_m(\lambda_m)} \cdot \frac{1}{\varepsilon(\lambda_{if})} \cdot \frac{T_m(\lambda_m)}{T_s(\lambda_{if})} \tag{4.8}$$

where $i_s(\lambda_{if})$ = scan channel signal current at the transition wavelength λ_{if} ,

$i_m(\lambda_m)$ = monitor channel signal current at the monitor wavelength λ_m ,

$\varepsilon(\lambda_{if})$ = relative detection efficiency of the scan detector system at the wavelength λ_{if} (see Appendix D),

$T_s(\lambda_{if})$ = transmission of the filter(s) used in front of the scan detector, and

$T_m(\lambda_m)$ = transmission of the filter(s) used in front of the monitor detector.

The usual method of combining uncertainties in quadrature yields

$$\frac{\Delta I_{if}}{I_{if}} = \sqrt{\left(\frac{\Delta i_s}{i_s}\right)^2 + \left(\frac{\Delta i_m}{i_m}\right)^2 + \left(\frac{\Delta\varepsilon}{\varepsilon}\right)^2 + \left(\frac{\Delta T_m}{T_m}\right)^2 + \left(\frac{\Delta T_s}{T_s}\right)^2} \tag{4.9}$$

where $\Delta Q/Q$ = fractional uncertainty in the quantity Q.

As discussed in Section 4.2, the uncertainties in the transmission of the filters were small and will be neglected from further discussion. The uncertainty, Δi_m, in the quantity, i_m, was also small, since the source stayed constant for periods long compared to the time taken to perform the measurement of i_s. We will also neglect this source of uncertainty in the following discussion.

Using relation (4.1), we find for the fractional uncertainty ΔR_{if} in R_{if}

$$\frac{\Delta R_{if}}{R_{if}} = \frac{1}{(\sum\limits_k I_{ik})} \left\{ \sum_k{}' \Delta I_{ik}^2 + \left(\sum_k{}' I_{ik}\right)^2 \left(\frac{\Delta I_{if}}{I_{if}}\right)^2 \right\}^{1/2} \tag{4.10}$$

where $\sum\limits_k$ is a sum over <u>all</u> the branches (including the branch at λ_{if}) and $\sum\limits_k{}'$ is a sum over all branches <u>except</u> λ_{if}. The quantity $\Delta I_{if}/I_{if}$ is defined in equation (4.7).

The uncertainty $\Delta R/R$ can be much smaller than the uncertainty $\Delta I/I$. For example, if there is only one branch out of an upper level, or if one of the branches dominates the decay, then the uncertainty in R for this branch will be small even if the quantity I is measured imprecisely.

The uncertainty in the relative detection efficiency of the spectrometer is discussed in Appendix D and has a value of approximately ±15% in the wavelength region λλ3200-8000. It is important to note, however, that this uncertainty is of little importance in some cases. For all except the g^3F_3 level, more than 90% of the decaying strength is emitted at a few wavelengths that are only a few hundred angstroms apart. Since the detector efficiency does not change rapidly with wavelength in the visible region, the difference in the efficiency at two wavelengths within 100Å of each other is negligible and there will not be a ±15% uncertainty in the relative efficiency.

Let us consider a simplified example. Suppose an upper level has only three branches at $\lambda 3500$, $\lambda 3600$ and $\lambda 3700$. Since the detector efficiency changes by only 3% over this region of the spectrum, we do not have to know the efficiency at all in order to measure the relative strengths of the three decay channels. Of course, we really have to measure the efficiency in order to make certain that it does not change significantly in the region $\lambda\lambda 3500$-3700.

We have assumed that the uncertainty $\Delta\varepsilon(\lambda_{if})$ in the relative detection efficiency $\varepsilon(\lambda_{if})$ is related to the distance $D_{if}(\text{Å})$ from the wavelength λ_{if} to the wavelength where most of the strength is emitted, by the equation

$$\frac{\Delta\varepsilon(\lambda_{if})}{\varepsilon(\lambda_{if})} = 0.15\left(\frac{D_{if}}{2000}\right) \tag{4.11}$$

If D_{if} is greater than 2000Å, then we have taken $\Delta\varepsilon/\varepsilon = 0.15$.

There are two contributions to the uncertainty in the quantity i_s : the uncertainty in the reading of the intensity above the local continuum level, and the consistency or reproducibility uncertainty when a line is scanned more than once. The first of these two uncertainties is significant only for weak lines.

All of the branches were scanned more than once during a given set of measurements on a given day. The quantity i_s was typically constant to within ±5% for the stronger lines ($R \geq 2\%$) and ±15% for the weaker lines ($R < 2\%$). Branching ratios for all of the levels have been measured on two or three different occasions. For those measured more than twice, the third measurement was made by W. A. Zajc, an undergraduate summer employee. The differences in measurements made at different times by a different observer give an estimate of the uncertainty in the quantity i_s. The uncertainties in i_s range from ±5% to ±25%, depending on the strength of the branch. We have estimated the uncertainty in i_s for each branch, and evaluated the subsequent uncertainties in R_{if} and in A_{if} using equations (4.7), (4.9) and (4.10). For the very strong branches, the uncertainty in the value of A_{if} is dominated by the uncertainty ($\sim$ ±15%) in the lifetime value. For the weaker branches, the uncertainties in the branching ratios are larger than the uncertainties in the lifetime.

The uncertainties in the branching ratios, in the transition probabilities and in the values of log gf are listed for each line in Tables 5-17.

4.7 COMPARISON OF RESULTS WITH OTHER WORKS

In view of the vast amount of data tabulated by Corliss and Bozman (1962), we have compared our branching ratios with their results in Tables 5-17. In general, they include most of the branches out of the low energy levels. For lines whose branching ratios are larger than about 3%, the values quoted by Corliss and Bozman (denoted

CB) are in agreement with our results within ±20%. For the very weak branches, the CB values are generally too large by a factor that ranges from 2-5. In calculating their branching ratios, we have used only those branches for which they have measured values to construct a partial sum corresponding to equation (2.6). The CB branching ratios are therefore upper limits to the correct values. We have not corrected the CB values to include those weak branches which they did not observe.

For the four levels at high excitation energies, the CB compilation is very incomplete, as is the case of the g^3F_3 level for which CB have observed only the branch at λ5664 (see Table 14). Thus, it is not a fair comparison for these levels.

Corliss (1965) has summarized all the experimental work done on Ni I transition probabilities prior to 1965. Since that time, Lawrence *et al*. (1965) have made absolute measurements in absorption for six lines in Ni I using the atomic beam method. Bell *et al*. (1966) have measured relative transition probabilities for 16 Ni I lines using a wall-stabilized arc. Garz *et al*. (1970) have measured relative transition probabilities for 50 Ni I lines using an electrical arc burning in an argon atmosphere. Both Bell *et al*. and Garz *et al*. normalize their relative values to the absolute scale determined by Lawrence *et al*. Laurent and Weniger (1970) have measured photographically relative gf values for 33 Ni I lines in absorption using a high pressure noble gas discharge. They have normalized their relative data to the absolute scale of Corliss (1965).

Table 20 shows the comparison of $\log gf_{CIT}$ (this work) with the results of Bell *et al.*, which are denoted $\log gf_{BPW}$, for the 7 lines measured in common by both groups. The average deviation is found to be $< \log gf_{BPW} - \log gf_{CIT} > = 0.051 \pm 0.060$, where the uncertainty is due only to the scatter in the individual differences and does not include experimental uncertainties of measurement. The agreement between Bell's values and those measured in this thesis is satisfactory, although our values for $\log gf$ are smaller in all instances.

Of the 50 gf values reported by Garz *et al.*, 13 have also been measured in this work. Figure 8 shows a comparison of the two works. The dashed straight line is not a fit to the data points but is a plot of $\log gf_{CIT} = \log gf_{GHR}$ which has been drawn to aid the reader in comparing results. The mean value of the difference $< \log gf_{GHR} - \log gf_{CIT} >$ is found to be 0.026 ± 0.034 which is also consistent with zero. The uncertainty has been computed in the same manner as above.

Since Corliss' compilation is an extensive summary of previous results for Ni I, we have compared our gf values with his values in order to find the source of the discrepancies in the Ni abundance determinations (see Table 1). Figure 9 is a plot of $\log gf_{CIT}$ against $\log gf_{CORLISS}$. The data for high energy (even parity) levels ($E_u > 6$ eV) are plotted with solid diamonds and those for the low-lying (odd parity) levels ($3.4 < E_u < 4.3$ eV) with solid sqares. The solid straight line has a slope of unity and passes through the origin, as does the dashed line in Figure 8.

The discrepancies between our Ni I data and those of Corliss are greater for the levels at high excitation energies than for the levels at low excitation energies. Our gf values are smaller than Corliss' values by approximately a factor of 3.0 for the low energy levels and by a factor of 4.6 for the high energy levels.

In order to ascertain if there is a systematic error in the wavelength calibration of the detector efficiency (see Appendix D) used in our measurements, we have compared our gf values to those of Corliss as a function of the wavelength, λ, of the transition. Figure 10 shows a plot of $\log(gf_C/gf_{CIT})$ against wavelength, where the subscript "C" refers to Corliss. The same plotting symbols have been used as in Figure 9. There is no apparent variation of this ratio in the wavelength region λλ3000-8000. We find this result encouraging since any systematic errors in the individual works upon which Corliss has based his compilation should be effectively washed out in his chosen "best" values.

We have compared our gf values to those of Laurent and Weniger (1970) to see if their results form a reliable set of relative gf values. Although there are only 6 lines measured in common by both groups, there is a serious discrepancy in the case of λ3458.474 (RMT No. 19). Our measured value is $\log gf_{CIT} = -0.37 \pm 0.05$ while Laurent and Weniger obtained $\log gf_{LW} = -0.94$. No uncertainty has been given for their result. Since Bell <u>et al</u>. and Garz <u>et al</u>. have both measured log gf for this transition and obtained -0.28 and -0.46 respectively, we find the value of Laurent and Weniger to be in error. A discrepancy of the same magnitude but in the opposite direction (that is, $\log gf_{LW}$

being too large) was found in comparing the GHR and LW gf values for the λ3624.733 (RMT No. 2) transition. Even if the LW relative data were normalized to the scale of Lawrence et al. (1965) as was the case with the GHR and BPW data, there is still a large scatter in their results in comparison with those reported in this thesis and with those of GHR and BPW. We therefore conclude that the LW data are unreliable.

The comparison of our results with those of Corliss (1965) reveals a systematic difference in log gf that is a function of the excitation energy of the upper level involved in the transition. A similar problem in the transition probabilities measured for other iron group elements has been discussed by Smith and Whaling (1973) for Fe II and by Cocke et al. (1973) for Cr I. It has been the subject of many other attempts to introduce a temperature correction to the work of earlier investigators. Since Corliss' data are a summary of many other works, we would not expect to find a simple relationship that would correct his values as a function of excitation potential.

The particular energy level structure of Ni I makes it difficult to attempt to correct Corliss' data. Ni I has three main groups of energy levels: the even parity levels that are near the ground state ($E_{ex} \sim 0$ eV), the low-lying odd parity levels that have been mentioned earlier (3.4 eV $< E_{ex} < 4.2$ eV), and the high energy even parity levels ($E_{ex} > 6$ eV). We feel that any attempt to use the CIT gf value data, supplemented perhaps by the GHR and BPW data, to obtain an empirical correction to Corliss' data based on essentially two values of excitation energy is dangerous and unwarranted.

5. SOLAR DATA

5.1 INTRODUCTION

Since the purpose of this work was to determine the solar abundance of Ni using the gf values measured in the laboratory, we must now turn to an analysis of the solar spectrum to relate the number of atoms to the solar line intensities.

There are many published spectra which record the emergent intensity of radiation from the sun in various wavelength regions. Rowland (1895-97) published a "Preliminary Table of Solar Spectrum Wavelengths" which spanned the visible region, λλ2935-7330. Rowland estimated the line intensities but the results were not precise enough to be used as direct measurements of equivalent widths. The equivalent width, W, of a Fraunhofer absorption line is defined as the width of a hypothetical line which, being perfectly black and having infinitely sharp edges, would absorb from the neighboring continuum the same amount of energy as the real line. W is then an integrated value for the strength of an absorption line.

The results of all earlier investigations were summarized by Moore _et_ _al_. (1966) in her publication of a compendium of solar wavelengths, identifications and W's for approximately 24,000 lines in the wavelength range λλ2935-8770. This work is essentially a second revision of Rowland's tabulation, except that it makes extensive use of the Utrecht photometric atlas (Minnaert _et_ _al_. 1940) for the quantitative measures. The introduction to Moore's work discusses the sources of the measurements. Equivalent widths given in Moore's tabulation will be denoted by W^{NBS}.

Mohler has also recorded the solar spectrum photoelectrically, but only that part in the near infrared has been published (Mohler *et al*. 1950). However, the unpublished spectrum, recorded at the McMath-Hulbert Observatory of the University of Michigan, has been referred to often in the literature (Cowley and Cowley 1964; Holweger 1967) and W's obtained from this so-called Michigan Atlas will be denoted by W^{Mich}.

A very recent spectrum (Delbouille *et al*. 1973) was recorded photoelectrically with the double-pass solar spectrometer installed at the Jungfraujoch Scientific Station (Switzerland). The new Kitt Peak Preliminary Solar Atlas (Testerman 1973) was recorded in the same manner as the Swiss spectrum. Both show substantially better resolution than has been previously attained. Although the Kitt Peak data have not been published, the spectrum is available on film upon request from the Kitt Peak National Observatory.

5.2 EQUIVALENT WIDTHS FOR SOLAR Ni LINES

Stars like the sun have a large number of metallic lines, increasing in both number and strength towards shorter wavelengths and thereby depressing the continuum. Iron, nickel and other metals with similar first ionization potentials are 10-20 times more abundant in the singly ionized state than in the neutral state at the temperature of the middle photosphere. As atoms are ionized, their spectra shift towards the blue region, thus making the blue spectrum quite crowded and difficult to analyze. For wavelengths shorter than about λ4000, essentially all lines become blended and it is not easy to establish the true location of the continuum. Equivalent widths for lines with $\lambda < 4000\text{Å}$ are difficult to measure accurately and are less reliable.

In this work, the equivalent widths for most of the lines with $\lambda > 4000\text{Å}$ have been obtained from the Kitt Peak Preliminary Solar Atlas, and will be denoted by W^{KP}. The details of the method used to record the spectrum can be found in the literature (Brault _et al_. 1971).

To obtain W's from the Kitt Peak (KPNO) data, a region of the spectrum within approximately ±1Å of the line in question was synthesized by a sum of Voigt profiles. Figure 11 shows a typical synthesis for the Ni I line at λ5157.993 (RMT No. 111). The solid spectrum on the left is the actual observed solar spectrum. The dots show the spectrum obtained by the synthesis method. Above the left plot is the residual (difference between observed and calculated) plotted on the same scale as the spectrum below it. The plot on the right shows the individual lines used in the synthesis to obtain the best fit. The particular Ni line of interest is shaded in the plot at the right. Note that some of the lines are broader than others, and that the insertion of a broad line for which there is no physical explanation is somewhat of an "ad hoc" assumption. The computer program minimizes the residual between the calculated spectrum and the observed spectrum in the vicinity of the line of interest. The "ringing" of the residual at the line centers is caused by slight asymmetries in the line profiles, since the synthesized (Voigt) profiles are symmetric functions. Although the fits to the observed spectrum are usually very good, we must consider the W value uncertain by an amount that is difficult to estimate when such fits require unknown opacity sources.

Figure 12 shows the synthesis for the Ni I line at 4009.984 Å (RMT No. 150). This is an example of how the spectrum becomes more crowded as the wavelength gets shorter in the ultraviolet. It also illustrates the unblending of lines which are close together in the synthesis analysis.

Table 21 shows the values of W determined in this work, with other values given in the last column. Primarily the other W's are from Moore _et al_. (1966) unless otherwise indicated. Figures 13 and 14 show $\log(W^{KP}/W^{NBS})$ plotted as functions of wavelength and W^{NBS} respectively. There appears to be no systematic dependence of this value on the solar line intensity itself. However, it appears that the differences between W^{NBS} and W^{KP} decrease with increasing wavelength. This can probably be explained by the fact that the continuum is much easier to establish in the redder wavelength region where the spectrum is not complex. In the bluer region (λλ4000-5000) there are overlapping lines, and the tendency in determining W's has been to use the highest point within a few angstroms of the line of interest as the continuum level. For the Kitt Peak spectrum, the continuum was located in the following manner: for each 100Å (approximately) long portion of the spectrum, the continuum was approximated by the parabola with the minimum area but whose intensity was at _every_ point greater than or equal to the actual observed intensity. Also, each portion was overlapped with that before and after it to ensure that the continuum was indeed continuous over the entire spectrum. Thus, the continuum level near a particular line is determined by the highest intensity point within about ±50Å of that line. Since most sources of continuous opacity, by their very definition, are broad on a wavelength scale, this parabolic approximation should be representative of the true opacity. In any case, the continuum level assumed for the KP spectra will be equal to or higher than that assumed by taking the highest point close to a line. Our results are that the KP W's are on the average 7% larger than W^{NBS}. This systematic difference is probably due to the different methods of placing the continuum.

There are, of course, cases where serious discrepancies exist in comparing the two values of W. The most obvious of these is $\lambda5371$, where $\log(W^{KP}/W^{NBS}) = -0.34$. The only explanation for this disagreement is that the Ni I line is blended with a strong Fe I line at $\lambda5371.493$ (RMT No. 15). Figure 15 illustrates our unblending of the spectrum for this line. The fit is not good.

The original impetus for obtaining more reliable W values came from the Ni I $\lambda3367.892$ (RMT No. 20) line, which was severely blended in the spectrum used by Moore with a Zr II line at $\lambda3367.81$ (RMT No. 11). Figure 16 shows this blend as observed by Brückner (1960), by Mohler in the Michigan Atlas (unpublished) and in the KPNO preliminary atlas. The synthesis of the spectrum in this region yielded $W^{KP}(\text{Ni I } 3367) = 84.4$ mÅ and $W^{KP}(\text{Zr II } 3367) = 44.3$ mÅ. Moore gives each a W of 39 mÅ. There is no clear explanation of the discrepancy in her value for this line. It is clear from both the Michigan tracing and the KP data that the Ni I line is significantly stronger than the Zr II line.

Holweger (1967) has determined W's from the Michigan Atlas for 11 lines of Ni I for which we have obtained W^{KP}. Figure 17 shows a plot of $\log(W^{KP}/W^{Mich})$ against wavelength (λ) for these 11 lines. Again the KP values are all larger by 5 (±6)%, where the uncertainty is due to the scatter of the individual values. This difference will be discussed with respect to our solar curve of growth for Ni I in Section 5.4. Garz (1971) has used Holweger's values of W^{Mich} for 21 lines in his abundance determination. A comparison of W^{Mich} with W^{NBS} for these 21 lines indicates that both W's are the same within approximately 1-2%. Cowley and Cowley (1964) obtained the same results in their comparison of W^{NBS} with W^{Mich} for a number of lines of iron group elements.

5.3 UNCERTAINTIES IN THE EQUIVALENT WIDTHS

An estimate of the reliability of the W's obtained by spectrum synthesis may be obtained by comparing measurements made by different persons on the same spectra. L. Testerman of Kitt Peak has synthesized the spectrum for 28 of the same lines as we did earlier. His results are 1 (±1)% larger. This difference indicates that the reproducibility uncertainty in the W^{KP} values is negligible. Since the KP values are about 7% larger than both the NBS and the Michigan values, the uncertainty associated with measurements taken from different spectra is about ±7%.

The "accidental" uncertainties in equivalent width measurements due to unrecognized blends are more difficult to assess. It may be that the W for a line is correct although its identification is wrong. This type of uncertainty will always mean that the true W is less than the measured W since there may be another element with a spectral line at exactly the same wavelength which is contributing to all or part of the absorption. As an example, Ni I has a transition encountered in this study at λ9689.35 (RMT No. 295) for which we have measured an upper limit for log gf . Table 14 shows that $\log gf < -0.97$. The measured W for this line is $W^{KP} = 62.6$ mÅ . Using the curve of growth analysis (see Section 5.4), we would determine a <u>lower</u> limit for the solar Ni abundance from this line $A_{Ni} > 7.75$ using the upper limit for log gf. However, Si I also has a line at λ9689.41 (RMT No. 65). Since Si is twenty times more abundant than Ni in the sun, it is most likely that most (or all) of the contribution to the solar absorption intensity can be attributed to Si. We have assumed that gross errors caused by unrecognized blends have been eliminated by the curve of growth analysis discussed in the next section (Section 5.4).

An error in the location of the continuum by ±1% of the central depth of a line will lead to an error in the W value by about ±5% since the lines are broader at the continuum level. There is no way of reducing this uncertainty.

The uncertainty in the measured value of W for a given line, especially for a weak line where an error in locating the continuum by even a small amount can drastically affect W , is a sensitive function of the nature of the nearby portion of the spectrum. Since all of the lines employed in the abundance determination (see Section 6) are weak with $W < 100$ mÅ, we have assigned a probable uncertainty of ±10%. It is also felt that further analysis of the uncertainties in the W values would not be worthwhile in view of uncertainties in the lifetime and branching ratio measurements.

5.4 SOLAR CURVE OF GROWTH FOR Ni I

A curve of growth is a two-dimensional plot which relates the equivalent width (W) of a Fraunhofer line to the various atomic and atmospheric parameters that enter into the formation of the line. Specifically, it is a plot of $\log(gf\,\Gamma)$ against $\log(W/\lambda)$ for many lines of an element. Γ is a function of the ionization potential of the element, the wavelength (λ) of the absorption line, the excitation energy (E_ℓ) of the lower level involved in the transition and the particular stellar model. Excellent reviews of the construction of such a curve can be found in Aller (1963) and in Unsöld (1955).

In our work the main function of the construction of an empirical curve of growth was as a consistency check on the gf and W values for the lines being studied. It was through this curve that we first were made aware of the gross error in the W value for the λ3367 line as it appeared in Moore et al. (1966) as discussed in Section 5.2. Until recently, it was the practice to derive elemental abundances from these curves (see Section 6.3). With the development of high speed computers, the practice is now to perform fine analysis model atmosphere calculations using current stellar models.

A solar curve of growth for Ni I has been constructed using the solar model of Cayrel and Jugaku (1963) to obtain $\Gamma_\odot$ (hereafter denoted simply Γ). The empirical data are shown in Figure 18 with solid dots. The solid curves are theoretical curves of growth taken from Hunger (1956) for specific choices of the damping parameter, a .

Only those 82 data points with abscissae ($\log(gf\,\Gamma)) < 4.5$ were used in obtaining the best fits to the theoretical curves. A computer code was developed to minimize the function

$$\chi_\nu^2 = \sum_{i=1}^{\nu+2} \left[\left(\frac{y - y_i}{\sigma_{y_i}}\right)^2 + \left(\frac{x - x_i}{\sigma_{x_i}}\right)^2\right] \tag{5.1}$$

where $y_i = \log(W/\lambda) + 12$, $x_i = \log(gf\,\Gamma)$, σ_{y_i} and σ_{x_i} are the probable uncertainties associated with the gf and W values, and y and x are the coordinates of the theoretical function. Table 21 gives the coordinates of the data points shown in Figure 18. The best fit to the data was obtained for $a = 0.010$, yielding a normalized $\chi^2 (= \chi_\nu^2/\nu)$ of 1.3. The fit was only slightly worse with $a = 0.032$ and much poorer with $a = 0.0032$.

It is convenient to divide the curve of growth into three distinct regions depending on the strength of the lines which fall into each.

(i) The weak lines, which for Ni I appear to be those with $W/\lambda < 10^{-6}$. They absorb radiation only in the Doppler-broadened line core. In this region (see Goldberg et al. (1960))

$$\log(W/\lambda) = \log(gf\,\Gamma) + \log(N_{Ni}/N_H) \tag{5.2}$$

Therefore, $W/\lambda = gf\Gamma\, N_{Ni}/N_H$; these lines may be employed to determine the Ni abundance directly (see Section 6.3).

(ii) The medium-strong lines which fall in the flat or transition region. For these lines the increase of W with

N_{Ni} is due to incipient absorption in the line wings since the core of the line is beginning to saturate. Radiative transfer theory (see Mihalas 1970) predicts that $W/\lambda \propto \sqrt{\log(N_{Ni}gf)}$ in the transition region.

(iii) The strong lines which fall in the so-called damping region. All the increase in W results from absorption in the line wings. In this damping region, $W/\lambda \propto \sqrt{N_{Ni}gf}$.

For regions (ii) and (iii) it is always true that

$$\log(W/\lambda) < \log(gf\ \Gamma) + \log(N_{Ni}/N_H) \tag{5.3}$$

A plot of $\log(W/\lambda)$ against $\log(gf\ \Gamma)$ therefore has a slope of 1 in region (i), a slope of 1/2 in region (iii), and a slope of almost zero in region (ii).

There has been much discussion (Wright 1948; Cowley and Cowley 1964; and Foy 1972) concerning the damping portion (iii) of the curve of growth. Wright finds a slope of 0.57 instead of 0.50 in this region, but he used 212 lines of <u>two</u> different elements, Fe I and Ti I, and had to shift the abscissae of their individual curves of growth in order to superpose all the points onto the same curve. Cowley and Cowley find a visually estimated slope of approximately 0.60 using 612 lines of neutral iron group atoms. Foy concludes that the damping part of the curve is unquestionably split into several branches, each of which corresponds to a different value of the damping parameter, a . Roberts <u>et al</u>. (1973c) use lines from upper levels having the same excitation energy in Ti II to construct an empirical plot which they fit to a theoretical curve having $a = 0.0040$. We do not here attach any significance to the value of $a = 0.01$ which best fits our data, nor do we draw any conclusions from the fact that all the strong lines seem to lie above the fitted curve, except to note the qualitative agreement with these other works. Therefore, Figure 18 shows a dashed line for the region where $\log(gf\,\Gamma) \geq 4.5$, since data points in this region were not used to establish the fit to the theoretical curve. Since no use has been made of the strong line data in the abundance determination (see Section 6), they will not be discussed further.

The open squares in Figure 18 are data from Garz (1971), which were not used in obtaining the best fitted theoretical curve. These points are those lines on which his abundance value is based (see Section 6.2). The fact that his data all lie below the best fit solid curve corroborates the suspicion that W's taken from the Michigan Atlas (which is the source of his W values) are slightly smaller than the recent KP values (see Section 5.2 and Figure 17). The differences in these W measurements are such as to raise Garz' data points and thus improve the agreement between the solid curve and his data.

The data point plotted with an open circle is that for λ3722.484 (RMT No. 18) which also has not been included in the fit. We do <u>not</u> believe Moore's value of 204 mÅ for the equivalent width of this line, since we have checked our gf value of 0.0049 and do not believe it to be substantially in error. This is a good example of the usefulness of a curve of growth to test the reliability of our W values. We have not been able to successfully synthesize the spectrum in this region because of its complexity, as shown in Figure 19. The Ni I line is badly blended with a strong Fe I line (W^{NBS} = 694 mÅ) at λ3722.564

(RMT No. 5). Figure 19 also shows the proximity of the Ni line to the very strong Fe I resonance line at λ3720, which makes the problem of locating the continuum very difficult and uncertain. The scientific yield from further analysis of this line is out of proportion to the effort required.

6. SOLAR ABUNDANCE OF NICKEL

6.1 INTRODUCTION

Theories concerning the evolution of stars must devise some mechanism to explain the formation of the heavy elements from lighter ones. One of the crucial tests of any such theory is the comparison of predicted relative abundances with those observed. The strength of elemental absorption lines in stellar spectra is a function of the number of atoms of that element acting to produce the absorption. In this way, the abundance of an element in a star can be inferred from a detailed examination of the line spectrum of that star.

It is natural that such studies should be directed towards that star which is most easily observed with high spectroscopic resolving power—our sun. The primary observational quantities are the equivalent width and shape of solar emission and absorption lines. The actual numerical value of an abundance is obtained only after a lengthy and intricate analytical process involving some assumptions concerning stellar atmospheres, mechanisms of line formation and broadening and atomic transition probabilities.

The availability of relatively accurate model atmospheres in recent years would appear to make such analysis feasible. Ross and Aller (1972) claim that there are available at this time a large number of "satisfactory" model atmospheres for the sun. The value of the derived abundance will depend in some small way on the particular choice of model, but for lines that are formed in the intermediate layers, such as moderately weak metallic lines with intermediate to high ionization potentials, the practical differences in models is only about ±0.1 dex in log N. All plane parallel stratified model solar atmospheres are in good accord in intermediate photospheric layers. They may differ, however, in the shallow layers where lines of easily ionized elements such as potassium and sodium are formed and where the very strong lines are formed.

There are other problems which hinder a definitive determination of solar elemental abundances. Even for those elements (approximately sixty-five) which are represented by unblended spectral lines observable from the earth's surface, it is unlikely that reliable gf values will be available. Departures from local thermodynamic equilibrium (LTE) may prove to be important for lines formed in the upper photosphere. It is by now a well known fact that lines of different excitation and ionization potentials originate at different depths in the atmosphere because of the temperature and pressure gradients.

6.2 Ni ABUNDANCE FROM MODEL ATMOSPHERE CALCULATIONS

The details of a model atmosphere calculation will not be cited here. Aller (1963) has outlined the method whereby one can construct a realistic atmospheric model for the sun. Elemental abundances for the sun are always given in terms of the number of atoms relative to hydrogen

$$A_{el} = \log_{10}(N_{el}/N_H) + 12.00 \tag{6.1}$$

where A_{el} is the elemental abundance and N_{el} and N_H are the total number of atoms (per gram) of the element and of hydrogen respectively.

The total number of atoms is related to the number of atoms in a given level of a given ionization stage through the Saha and Boltzmann equations, assuming LTE. All of the calculations described here have been carried out assuming LTE.

The analysis of the solar Ni abundance has been accomplished by determining the theoretical profiles which best fit the unblended profiles for a number of Ni I lines for which we have measured absolute transition probabilities. The fitting was carried out by L. Testerman at the Kitt Peak National Observatory using our gf values and the solar data discussed in Section 5. His analysis is a continuation of the study by Evans and Testerman (1974) on the ability of several microturbulence models to fit Fe I and Fe II absorption line profiles from center to limb.

The particular Ni I lines chosen for the abundance analysis were those which (i) did not appear blended in the line core, (ii) did not have a large asymmetry, and (ii) had an equivalent width less than 100 mÅ.

Three different temperature models were tried to test their consistency: that of Holweger (1967); the Elste Solar Model 10 (Elste 1967); and the Harvard-Smithsonian Reference Atmosphere (Gingerich _et al_. 1971) which is denoted HSRA. The systematic differences among these models had been found to be small by Evans and Testerman from their Fe work. They found that $A(\mathrm{HSRA}) - A(\mathrm{Elste}) \simeq 0.03$ and $A(\mathrm{Holweger}) - A(\mathrm{HSRA}) \simeq 0.06$ averaged over 16 Fe lines with $W \leq 100$ mÅ. Since the HSRA yields results between the other two models, it has been used to derive the Ni abundance values in this thesis. Cocke _et al_. (1973)

have stated that for Cr, the HSRA model yields results approximately 0.02 dex higher than the Elste model, which is consistent with the Fe results.

The results of Testerman's analysis for 20 Ni I lines are shown in Table 22. They are based on data from the center of the solar disc. In finding the mean value, $A_{Ni} = 6.29 \pm 0.14$, we have taken the mean of the logarithms. The uncertainty given is due only to the scatter of the individual values from the mean.

Testerman's results show that the abundance is almost independent of the microturbulent velocity. Variation of the macroturbulent velocity serves to improve the fitted profiles without changing the abundance. Since Evans and Testerman have not yet completed their study of the effects of micro- and macroturbulence on fitting observed profiles, it will not be discussed in this thesis. It was also found that the abundance obtained by fitting profiles observed at the solar limb was approximately 0.1 dex lower than the value derived from the observed profiles at the center of the disc. No explanation for this behavior has been found.

We can determine an independent value for the solar Ni abundance using Holweger's (1967) analysis of solar Ni. Holweger has measured W's for 84 Ni I lines from the unpublished Michigan Atlas. Using his solar model, he has tabulated the quantity $\log(gf\ \varepsilon_{Ni})$ where the symbol ε_{Ni} refers to the Ni abundance value. Using our notation, his tabulated quantity is $\log(gf\ \varepsilon_{Ni}) = A_{Ni} + \log gf$. We have measured gf values for 11 of the 84 lines which he has analyzed. Table 23 shows the A_{Ni} values derived from Holweger's $\log(gf\ \varepsilon_{Ni})$

using our gf values. The mean value obtained from these 11 lines is $A_{Ni} = 6.29 \pm 0.09$, where the uncertainty is due to the scatter in the individual values. The excellent agreement with Testerman's values indicates that Holweger's model and the HSRA model are consistent.

Garz (1971) has made a similar use of Holweger's analysis. She obtained a value $A_{Ni} = 6.25 \pm 0.13$ using $\log gf_{GHR}$ for 21 Ni I lines which appeared in Holweger's tabulation. The excellent agreement with our value confirms the conclusion drawn in Section 4.7 that gf_{CIT} and gf_{GHR} are in good accord (see Figure 8).

It should be noted here, in reference to the values shown in Table 1 for A_{Ni}, that previous results obtained using incorrect gf values may be corrected by using our new values. For instance, Grevesse (1969) has determined A_{Ni} using 21 Ni I lines. We have measured a gf value for only one of these lines, λ6108.121 (RMT No. 45). He obtained $A_{Ni} = 6.01$ using $\log gf = -2.50$. Using our value $\log gf = -2.78$ (see Table 5), we obtain $A_{Ni} = 6.29$ based on Grevesse's work, which is in good agreement with the values found by Testerman's and Holweger's analyses.

Table 24 summarizes the results of the abundance determinations. The values of A_{Ni} derived from the different analyses are in excellent agreement.

6.3 Ni ABUNDANCE FROM THE CURVE OF GROWTH

The empirical curve of growth technique has previously been used (Goldberg et al. 1964; Foy 1972) to determine the solar abundance of Fe. From Section 5.4, we see that the Ni abundance, A_{Ni}, for weak lines is given by

$$\log(W/\lambda) = A_{Ni} + \log(gf\Gamma) - 12.00 \tag{6.2}$$

(see equation (5.2)). A_{Ni} is obtained by extrapolating the weak line portion of the curve of growth with unity slope to the point where $\log(gf\,\Gamma) = 0$.

All three of the theoretical curves of growth that were fitted to our data as described in Section 5.4 can be seen to coalesce in this weak line region in Figure 18. The extrapolation described above yields a value $A_{Ni} = 6.26 \pm 0.13$. The uncertainty is derived from the uncertainties in the fitted parameters for the case yielding the best fit, $a = 0.010$. This result, which is then based on the model of Hunger (1956), compares favorably with the value $A_{Ni} = 6.29 \pm 0.14$ obtained by the model atmosphere calculations described in Section 6.2.

6.4 ADOPTED VALUE FOR THE SOLAR Ni ABUNDANCE

The values of A_{Ni} derived from model atmosphere calculations and from the curve of growth analysis are summarized in Table 24. From the scatter in the values obtained, we obtain a sample variance (see Bevington 1969) of approximately 0.14 dex. The uncertainties in the transition probabilities (see Tables 5-17) are never larger than ±40%, or ±0.14 dex in log gf , for the lines used in the abundance determination. The estimated uncertainty in the equivalent widths (see Section 5.3) is ±10%. Thus, the <u>maximum</u> uncertainty in the A_{Ni} value due to uncertainties in the measured gf and W values is ±0.15 dex for any line tabulated in Table 22 or Table 23. We would expect that an increase in the number of lines used to determine the abundance would lead to a corresponding decrease in the sample variance, σ, obtained from the results. Normally, $\sigma \propto (n)^{-1/2}$ where n is the number of individual values used to obtain a mean value. Since the sample variance obtained from the scatter in the individual values is much larger than we expect, it is probable that the main contribution to the variance comes from uncertainties in the solar model parameters.

Assuming the above value of 0.14 dex for the uncertainty in the reliability of the solar model, and adding a small uncertainty for the gf and W values, we adopt a value for the solar Ni abundance

$$A_{Ni} = 6.29 \pm 0.2 \tag{6.3}$$

based on this experiment.

6.5 USE OF ABUNDANCE VALUE TO CHECK THE LIFETIME VALUES

In Section 3.4, the cascading problem introduced the possibility that the measured lifetimes of low lying levels might be too long. From the relation between A_{ij} and τ_i (2.6), it is clear that if the lifetime τ_i were too long, then the value of A_{ij} would be too small, and thus gf is too small also. Since the quantity $g_j f_{ji} N_{Ni}$ is a free parameter to be determined in model atmosphere calculations (the equivalent width W is assumed to be known), a change in the laboratory value of gf would mean a corresponding change in the abundance N_{Ni} in the opposite direction.

If our measured lifetimes of low lying levels are systematically too long, caused perhaps by the cascading complexities in the light decay curves discussed in Section 3.4, then the abundance derived from branches emanating from these levels would be too large. This conclusion is valid if we assume that (i) the uncertainties in the branching ratio measurements and in the equivalent width determinations are purely random in nature, and (ii) the solar models used have no systematic uncertainties associated with the excitation energy of the lower level of the transition. It is difficult to assess the validity of either of these assumptions. Since lines having the same wavelength but originating from upper levels at different excitation energies are formed at different optical depths in the atmosphere, assumption (ii) is questionable. Assumption (i) is probably valid for our measurements.

Using the Testerman results (HSRA model) of Table 22, the mean abundance determined from the 15 branches out of the low-lying levels is 6.25. The corresponding mean for the 5 branches from high excitation energy levels is 6.40. A similar analysis of the Holweger data (Table 23) yields $\langle A_{Ni}(\text{high energy branches})\rangle = 6.31$ (average for 3 lines) and $\langle A_{Ni}(\text{low energy branches})\rangle = 6.31$ (average for 8 lines).

The Holweger results clearly show no difference between the two sets of levels. The Testerman results show a marked difference of 0.15 dex, with the low energy levels yielding a lower mean abundance. If there is a systematic error in the lifetime measurements, it is in the direction to make the low energy mean lives too short or the high energy mean lives too long, or both. We consider this possibility unlikely on the basis of the discussion in Section 3.4. Our agreement with the recent work of Garz (1971) for the value of A_{Ni} , and the agreement in the mean lives for two of the cases of overlap with Marek (1972) suggest that there are no large systematic errors in the lifetime values.

APPENDIX A

PHYSICAL REVIEW A VOLUME 6, NUMBER 3 SEPTEMBER 1972

Hydrogenic Transitions in Multiply Charged Fe and Ni Ions*

W. N. Lennard, R. M. Sills, and W. Whaling
California Institute of Technology, Pasadena, California 91109

(Received 1 May 1972)

Ten lines in the range $3880 \leq \lambda \leq 5666$ Å in the beam-foil spectrum of iron have been identified with specific hydrogenic transitions in Fe IV–VIII. The same transitions were observed from Ni and Ar beams. Deviations from the hydrogenic wavelengths are shown to be consistent with that expected from core polarization. The absence of these lines in astrophysical sources is discussed. A wavelength table is presented for identification of hydrogenic transitions to be expected in beam-foil spectra.

I. INTRODUCTION

In the visible radiation from a beam of iron ions excited by passage through a thin foil, Whaling *et al.*[1] found that the strongest lines in their spectrograms had wavelengths not previously reported for any iron ion. In this paper we describe a measurement of the charge of the ions radiating the ten strongest visible lines from a 1.5-MeV Fe ion beam. We propose transitions that will account for all of these wavelengths, and suggest that these same wavelengths will be seen in other heavy-ion beams when excited by the beam-foil method.

II. EXPERIMENTAL METHODS

The charge of the ion radiating the unknown wavelength was determined by measuring the displacement of the beam in a transverse electric field. An Fe^+ beam was accelerated to 1.3-MeV energy and then further ionized and excited by passage through a thin (10-$\mu g/cm^2$) carbon foil. Collimating slits (0.25×8 mm) located both ahead of and behind the foil defined a narrow ribbon beam. This radiant beam was deflected normal to its wide dimension in a transverse electrostatic field extending 10 cm downstream from the foil.

A monochromator with a 10-Å passband was placed to accept radiation from a 1-cm length of an arbitrarily selected beam trajectory in the deflecting field. Radiation from any other trajectory was blocked by a mask. A narrow (1 cm × 1 mm) slit in the mask, tangent to the selected trajectory, permitted radiation from the beam to reach the monochromator only if the beam was deflected along the selected trajectory. The deflecting voltage was varied to sweep the radiant beam across the slit. The product (deflecting voltage) × (ion charge)/(ion energy) is constant for a particular trajectory, and the value of this constant for the selected trajectory was determined by observing the voltage required to deflect a 0.65-MeV N^{2+} (λ4379) beam along this trajectory.

III. RESULTS

In Table I we present the charges measured for the ten strongest lines in the visible spectrum of the 1.5-MeV iron ion beam. The wavelengths listed in the first column were measured from the iron spectrogram in Fig. 1. In scanning these lines with the monochromator preparatory to measuring the ion charge, it was found that most of the lines are composed of two or more components with a spacing of a few Å. The wavelengths measured from the spectrogram are therefore an average over the several unresolved components. We estimate an uncertainty of ±2 Å in this average wavelength, even though the components may be spread over several Å about this average.

The measured charge is listed in the third column. The low efficiency of our photon detector (EMI 6256S) for wavelengths beyond 6000 Å made it impossible to measure the charges of the last four lines in the table, and the assignments of an ionic charge to these transitions are based on the analysis described below.

Once the charges were known, it was observed

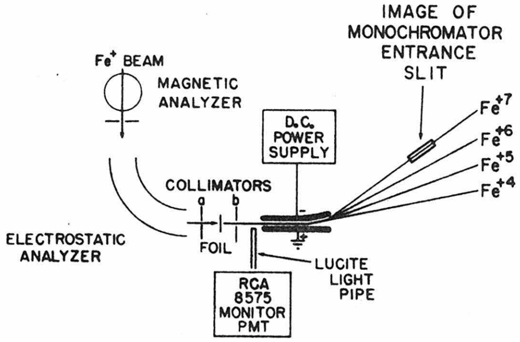

FIG. 1. Schematic diagram of the charge-deflection apparatus. The monochromator is positioned to receive light emitted out of the plane of the paper. Only light emitted from the 1-cm segment of the trajectory labeled "image of monochromator entrance slit" can reach the entrance slits of the monochromator. The deflection of the various charge states is greatly exaggerated in this figure: An actual off-axis deflection was 2 mm.

that the measured wavelengths were very close to those for $\Delta n = 1$ and $\Delta n = 2$ transitions between states of a single electron moving in a hydrogenlike orbit around a central charge $(Q+1)e^+$, where Qe^+ is the ion charge. In column 4 we list the wavelengths computed from the hydrogenic terms $T = -R(Q+1)^2/n^2$ for transitions between states with the principal quantum numbers listed in column 6. The last four wavelengths in column 1 and λ4658 were then classified by their near coincidence with transitions expected for ions with charge 3+ to 7+, the major components of our beam. The wavelengths listed in column 4 include *all* of the $\Delta n = 1$ and 2 transitions in our wavelength range $3500 \le \lambda \le 6500$ Å and charges $3+ \le Q \le 7+$.

To confirm our identification, we substituted a Ni beam for the Fe beam and repeated our measurements. The Ni spectrum is shown in the upper-half of Fig. 1. The striking similarity between the spectra of two different elements is convincing proof of the origin of these lines in common hydrogenic levels. We have seen the same lines from an argon beam, and we should expect to see the same lines in any ion beam containing ions of the same charge. Wavelengths measured from the Ni spectrogram appear in the second column of Table I.

The one-electron states excited in our experiment are expected to be more tightly bound than the Rydberg formula predicts for a one-electron ion because of (a) polarization of the ion core by the outer electron, (b) penetration of the core by the outer electron, and (c) the spin-orbit interaction. All of these interactions increase the electron binding and depend on n and l in a way that will shift transitions in which n and l decrease to the blue of the hydrogenic value, as observed in our spectra. According to Edlén,[2] the polarization effect is much the largest of these three corrections to the binding energy for states with large n

TABLE I. Identification of transitions in the Fe and Ni beam-foil spectra. The wavelengths are measured from spectrograms of Fig. 1 by comparison with an Fe reference spectrum.

λ_{obs} Fe (Å)	Ni (Å)	Measured Ion Charge	λ_{calc} (Å)	Ion Charge	Δn
3879	3883	6+	3888	6+	8 → 7
4336	4338	7+	4342	7+	9 → 8
4497	4497	5+	4500	5+	10 → 8
4516	4515	4+	4521	4+	9 → 7
4553	4553	6+	4557	6+	11 → 9
4625	4630	3+	4660	3+	6 → 5
4658	4658	...	4660	7+	12 → 10
4680	4682	3+ or 4+	4687	3+	8 → 6
4903	4904	...	4946	4+	7*h* → 6*g*
4934	4935	4+	4946	4+	7*i* → 6*h*
5283	5286	5+	5292	5+	8 → 7
5665	5666	6+	5671	6+	9 → 8
6063	6065	...	6070	7+	10 → 9
6079	6079	...	6086	6+	12 → 10
6197	6197	...	6202	5+	11 → 9
6475	6474	...	6480	4+	10 → 8

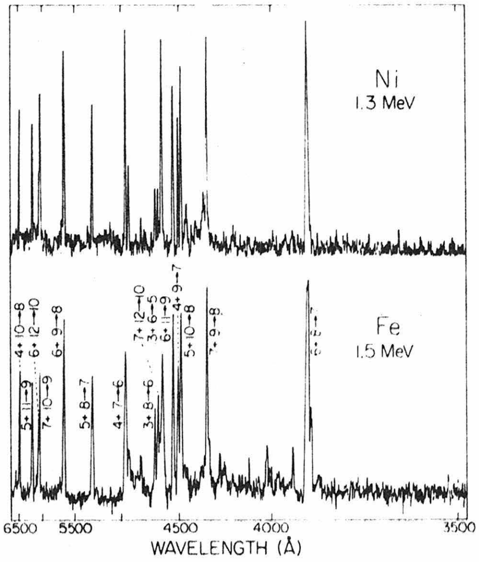

FIG. 2. Densitometer tracings of spectrograms of Ni and Fe beams excited by passage through 10-$\mu g/cm^2$ carbon foils. The angle of observation is 90°. The Fe spectrum is reproduced from Ref. 1, in which details of the exposure may be found.

and l. Edlén gives formulas for computing the wavelength shift due to polarization, but these depend on the polarizability of the core which is in general not known. For large n and l, the polarization correction approaches zero and the term values approach those given by the Rydberg formula.

The polarization of the core removes the degeneracy between states of the same n but different l and splits the hydrogenic lines into several components, and one expects the lines to exhibit a multiplet structure as well as a shift to the blue. For most of the transitions that we observed, this structure is too close to be evident in the spectrograms of Fig. 1. As mentioned above, many of the lines that appear single in the spectrograms have been found to have two or more components, separated by a few Å, but our measurements are not sufficiently precise to permit a detailed comparison of the observed structure and theoretical predictions. The only evidence for this splitting apparent in Fig. 1 is the weak line at 4903 Å which may correspond to the $7h-6g$ satellite of the $7i-6h$ line at 4935 Å. This weak line appears in both the Fe and Ni spectra, and there are no other likely hydrogenic transitions close to the observed wavelength. If one uses the observed shift of the 4935-Å line to compute a dipole polarizability for the Fe^{5+} core, one can then compute the expected position of the $7h-6g$ component. In this way, we find $\alpha_d(\mathrm{Fe}^{5+}) = 1.0a_0^3$ and compute $\lambda(7h-6g) = 4906$ Å, close to the observed value of 4903 Å. Supporting this interpretation is the fact that one expects the reddest component of the multiplet to be strongest, since states with maximum $l = n-1$ are favored as the electron cascades down from states with high-n values. One feature that is not accounted for in this analysis is the fact that λ4935 is actually a doublet, with two nearly equal components separated by 6 Å. This spacing is too large to be accounted for by spin-orbit splitting and must reflect some coupling of the outer electron with the Fe^{5+} core.

IV. DISCUSSION

Hydrogenic transitions between states of large n in multiply charged ions have been reported in many beam-foil (BF) spectra, but they are rarely observed in other laboratory sources and not at all in astrophysical sources. Gabriel[3] has observed such transitions in a high-density plasma pinch, and in particular has observed λ5280 in O^{5+}, the same line we have seen with Fe, Ni, and Ar beams. This same transition and several others between high-n levels have been reported from C^{5+} in the plasma generated when a high-intensity laser beam strikes a solid surface.[4] However, there is no other light source in which hydrogenic transitions are so prominent as they are in Fig. 1, and only in BF spectra have they been observed with ions as heavy as Fe or Ni.

It is interesting to inquire why these states are so readily excited in the BF interactions, and why they are seldom seen in other sources. Turning to the latter question first, their high excitation energy, hundreds of eV, is responsible for their weakness in a low-density plasma such as the solar corona, where Huang[5] has shown that excitation by electron capture is negligible compared to excitation by collision. The upper levels of identified coronal lines are typically at only a few eV of excitation energy. Dalgarno[6] has pointed out that the relatively long radiative lifetime of the hydrogenic states, increasing roughly as $n^{4.5}$, combined with their large cross section for collisional destruction, account for their weakness in a local thermodynamic equilibrium (LTE) plasma.

The same argument explains their absence in beams excited by passage through a gas. Brown *et al.*[7] have compared the radiation from a 900-keV sodium beam excited by passage through a carbon foil with the radiation from the same beam passing through helium at a pressure of 0.1 torr. The strongest line observed in the BF spectrum, λ4649, was not seen at all in the gas-excited spectrum. The charge of the ion radiating this strong line was measured by Brown, and later by Dufay *et al.*,[8] to be 3+. The $n = 6-5$ transition in the 3+ ion is at 4660 Å. From our estimate of the dipole polarizability of the seven-electron core, $\alpha_d = 0.51a_0$,[3] we would expect a wavelength shift of −12 Å, in good agreement with the observed shift of −11 Å.

The absence of this line in Brown's gas-excited spectrum can be understood by comparing the mean time between collisions, 1.5×10^{-10} sec, on the assumption of $\sigma_{\mathrm{coll}} = \pi(n^2 a_0/Z)^2$, with the radiative lifetime of the hydrogenic state, 24×10^{-10} sec.[9] The large collision cross section favors nonradiative deexcitation of the state. It would be of interest to repeat Brown's experiment with the gas pressure reduced by a factor of 100 to see if the hydrogenic line appears.

The prominence of hydrogenic transitions in BF spectra suggests that electron capture makes an important contribution to the excitation of the beam. In the usual picture of the passage of a charged particle through matter, the moving ion continually loses and recaptures its more loosely bound electrons in repeated encounters with the atoms of the absorber. The charge on the ion emerging from the surface is the net result of this sequence of many capture and loss events. The excitation of the emerging ion is brought about either by the last capture into an excited state, or by the last collision before the ion emerges into

TABLE II. Hydrogenic wavelengths: $\lambda^{-1}=R(Q+1)^2\,[1/n^2-1/(n+\Delta n)^2]$. Values in the table are for mass $A=46$, $R=109\,736\ \mathrm{cm}^{-1}$. For other masses, $\lambda_A=\lambda_{46}\,[1+1.2\times10^{-5}(46-A)/A]$. Table includes all transitions with $\Delta n=1$, 2, or 3, in the wavelength range 1000–8000 Å.

Ion	n	$(n+1)$	$(n+2)$	$(n+3)$
X^{+}	2	1640	1215	1085
	3	4687	3204	2734
	4	10125	6561	5412
X^{2+}	3	2083	1424	1215
	4	4500	2916	2406
	5	8284	5168	4154
	6	13739	8332	6561
X^{3+}	3	1172	801	683
	4	2531	1640	1353
	5	4660	2907	2337
	6	7728	4687	3691
	7	11907	7064	5472
	8	17368	10125	7738
X^{4+}	4	1620	1050	866
	5	2982	1861	1495
	6	4946	2999	2362
	7	7621	4521	3502
	8	11115	6480	4952
	9	15540	8931	6749
X^{5+}	4	1125	729	601
	5	2071	1292	1038
	6	3435	2083	1640
	7	5292	3140	2432
	8	7719	4500	3439
	9	10791	6202	4687
	10	14585	8284	6200
X^{6+}	5	1522	949	763
	6	2524	1530	1205
	7	3888	2307	1787
	8	5671	3306	2527
	9	7928	4557	3443
	10	10716	6086	4555
	11	14089	7923	5881
	12	18104	10094	7439
X^{7+}	5	1165	727	584
	6	1932	1172	923
	7	2977	1766	1368
	8	4342	2531	1934
	9	6070	3489	2636
	10	8204	4660	3487
	11	10787	6066	4502
	12	13861	7728	5695
	13	17468	9668	7081
X^{8+}	6	1527	926	729
	7	2352	1395	1081
	8	3431	2000	1528
	9	4796	2757	2083
	10	6482	3682	2756
	11	8523	4793	3558
	12	10952	6106	4500
	13	13802	7639	5595
	14	17108	9408	6852
X^{9+}	6	1237	750	591
	7	1905	1130	876
	8	2779	1620	1238
	9	3885	2233	1687
	10	5251	2982	2232
	11	6904	3882	2882
	12	8871	4946	3645
	13	11180	6188	4532
	14	13858	7621	5550
	15	16932	9259	6710
X^{10+}	6	1022	620	488
	7	1575	934	724
	8	2297	1339	1023
	9	3211	1845	1394
	10	4339	2465	1845
	11	5705	3208	2381
	12	7331	4088	3012
	13	9239	5114	3745
	14	11453	6298	4587
	15	13993	7652	5546
	16	16885	9186	6629
	17	20148	10913	7843
X^{11+}	7	1323	785	608
	8	1930	1125	860
	9	2698	1551	1172
	10	3646	2071	1550
	11	4794	2696	2001
	12	6160	3435	2531
	13	7764	4297	3147
	14	9623	5292	3854
	15	11758	6430	4660
	16	14188	7719	5570
	17	16930	9170	6591
	18	20005	10791	7728
X^{12+}	7	1127	669	518
	8	1644	959	733
	9	2299	1321	998
	10	3107	1765	1321
	11	4085	2297	1705
	12	5249	2927	2157
	13	6615	3661	2681
	14	8200	4509	3284
	15	10019	5479	3971
	16	12089	6577	4746
	17	14426	7813	5616
	18	17046	9195	6585
	19	19965	10731	7660
X^{13+}	8	1418	827	632
	9	1982	1139	861
	10	2679	1522	1139
	11	3522	1981	1470
	12	4526	2524	1860
	13	5704	3157	2312
	14	7070	3888	2832
	15	8639	4724	3424
	16	10424	5671	4092
	17	12439	6737	4842
	18	14698	7928	5678
	19	17215	9252	6605
	20	20004	10716	7626
X^{14+}	8	1235	720	550
	9	1727	992	750
	10	2334	1325	992
	11	3068	1725	1281
	12	3943	2198	1620
	13	4969	2750	2014
	14	6159	3387	2467
	15	7525	4115	2982
	16	9080	4940	3565
	17	10835	5869	4218
	18	12803	6907	4946
	19	14996	8060	5753
	20	17425	9335	6643
	21	20104	10737	7621

the vacuum.

The excited levels observed in this experiment have very large mean radii, 10–20 Å, whereas the mean spacing between atoms of the foil is ~2 Å. They have excitation energies of several hundred eV, whereas the electron energy at the ion velocity is only 14 eV. It seems clear that these levels are populated by the last capture event at the surface, not by collisional excitation. There is a high electron density at the surface, and the surface can absorb energy to permit nonradiative capture.

Different models of electron capture at a surface lead to different distributions of population of the excited levels. (a) If one assumes, following Bohr,[10] that the states favored in the capture process are those for which the electron velocity $[2\times(\text{binding energy})/m_0]^{1/2}$ is close to the velocity of the moving ion, one expects an ion of charge Q to show large initial population in states with

$n \approx (Q+1)[24.8A_{\text{ion}}/E_{\text{ion}}(\text{keV})]^{1/2}$. (b) If one adopts Oliphant and Moon's[11] assumption that capture is favored into states bound to the ion by an amount close to the work function of the surface, one would expect the primary population to be concentrated in states with $n \sim 1.7(Q+1)$, assuming a work function of 4.6 eV for the C surface. (c) Free-electron recombination that takes place after the ion has escaped from the influence of the surface would lead to an initial population that decreases with increasing excitation energy as $1/n^3$. We have examined our own results and the published observations of others and conclude that the third assumption is favored by the meager information presently available. The pertinent observations are these:

(i) The levels that are observed are limited only by the wavelength range of the experiment. For the ions which compose the major components of the beam, every $\Delta n = 1$ and 2 transition lying within the wavelength range of the detector is observed. There seems to be no upper bound on the excitation energy of the initial states populated.

(ii) For a given ion, transitions from levels of lower n appear to be stronger. Cascading contributes to this behavior and obscures the initial population.

(iii) Light decay curves for the level with quantum number n_u typically indicate cascading into the upper level from still higher levels with $n \geqq n_u + 1$, consistent with our conclusion from observation (i). However, there are no observations of *increasing* decay curves that would indicate a population in the $n_u + 1$ level much greater than that in the n_u level. Observations (ii) and (iii) suggest an initial population that is either independent of n or decreases with increasing n.

One is led to the conclusion that only assumption (c) is consistent with the observations. However, it is surprising that levels with $n \sim 10$ are seen at all if the population falls off as rapidly as n^{-3}. Jordan *et al.*[12] observed a population in He^+ that falls off more rapidly than n^{-3}, but it has been suggested that the behavior of helium and of heavy ions are qualitatively different. Dmitriev *et al.*[13] report that "electron capture by ions with $Z \geqq 4$ (unlike protons) occurs mainly in excited states." Further study of the initial populations should provide a valuable insight into the excitation process.

In conclusion, it should be noted that observation (i) above should aid experimenters in identifying unknown lines in their spectra. Hydrogenic lines appear in many published spectra without identification. As an aid to identification we list in Table II the wavelengths computed from the Rydberg formula for ions of charge 1^+–14^+. We list transitions for $\Delta n = 1$, 2, and 3, although $\Delta n = 3$ transitions in heavy ions are rare.[14]

ACKNOWLEDGMENTS

The authors are indebted to Alan Gabriel, L. C. Cocke, and S. Bashkin for helpful disucssions and access to unpublished results.

---

*Supported in part by NSF Grant No. GP-28027 and the Office of Naval Research Grant No. N00014-67-A-0094-0022.

[1] W. Whaling, R. B. King, and P. L. Smith, in *Beam-Foil Spectroscopy*, edited by S. Bashkin (Gordon and Breach, London, 1968), Vol. I, p. 81.

[2] B. Edlén, in *Handbüch der Physik*, edited by S. Flügge (Springer-Verlag, Berlin, 1964), Vol. 27, p. 80.

[3] A. H. Gabriel, in *Proceedings of the Fourth International Conference on Ionization Phenomena in Gases*, edited by N. R. Nilsson (North-Holland, Amsterdam, 1960), p. 829.

[4] B. C. Boland, F. E. Irons, and R. W. P. McWhirter, J. Phys. B 1, 1180 (1968).

[5] K. Huang, Astrophys. J. 101, 187 (1945).

[6] A. Dalgarno, in *Proceedings of the First International Conference on Atomic Physics*, edited by B. Bederson (Plenum, New York, 1969), p. 169.

[7] L. Brown, W. K. Ford, V. Rubin, W. Trachslin, and W. Brandt, in Ref. 1, p. 45.

[8] M. Dufay, M. Gaillard, and S. M. Carré, Phys. Rev. A 3, 1367 (1971).

[9] H. A. Bethe and E. E. Salpeter, in Ref. 2, Vol. 35, p. 88.

[10] N. Bohr, Phys. Rev. 59, 270 (1941).

[11] M. L. E. Oliphant and P. B. Moon, Proc. Roy. Soc. (London) A127, 388 (1930).

[12] J. A. Jordan, Jr., G. S. Bakken, and R. E. Yager, J. Opt. Soc. Am. 57, 530 (1967).

[13] I. S. Dmitriev, Y. A. Teplova, and V. S. Nikolaev, Zh. Eksperim. i Teor. Fiz. 61, 1359 (1971) [Sov. Phys. JETP 34, 723 (1972)].

[14] R. Hallin, J. Lindskog, A. Marelius, J. Pihl, and R. Sjodin, in Proceedings of the Second European Conference on Beam-Foil Spectroscopy, Lyon, 1971 (unpublished).

APPENDIX B

NUCLEAR INSTRUMENTS AND METHODS 110 (1973) 137–142; © NORTH-HOLLAND PUBLISHING CO.

ABSOLUTE BEAM-FOIL EXCITATION PROBABILITIES OF HYDROGEN-LIKE STATES IN IRON*

W. N. LENNARD† and C. L. COCKE+

California Institute of Technology, Pasadena, California, U.S.A.

By measuring the absolute intensities of hydrogen-like spectral lines, we have deduced absolute foil-excitation probabilities for several levels of high principal quantum number (n) and several emerging charge states of a 1.5-MeV iron beam. Core polarization allows the partial resolution of transitions involving different l-values for the same initial and final n. The probability that an iron ion emerging from the foil with charge state q is in a state characterized by n is found to be of order 10^{-3} for $n = 6$–9 and $q = 4^+$–7^+. For a given n, population of high l appears to be favored. A discussion of the overall state population distribution among high n states following foil excitation will be presented.

1. Introduction

There exists to date very little quantitative information on the process whereby a fast projectile emerging from a solid foil is left with outer shell excitations. An understanding of this process and resulting states of excitation of the outer shells bears not only on problems in beam-foil spectroscopy, but also on those in perturbed angular correlations which involve nuclei recoiling into a vacuum and in de-excitations whose decay might be influenced by properties of the outer shell of the emerging ion. In spite of much qualitative work on the subject, few hard numbers are available on either absolute probabilities for producing outer shell excitations in the emerging ion or even on the distribution among the outer shells of the excitations. An earlier paper[1]) has shown that the visible spectrum of foil-excited iron at 1.5 MeV is dominated by hydrogen-like transitions between shells of high principal quantum number ($n \approx 6$–9) in high charge states ($q = 4^+$–7^+) of the iron ions ($n \approx q$). We have undertaken a measurement of the absolute excitation

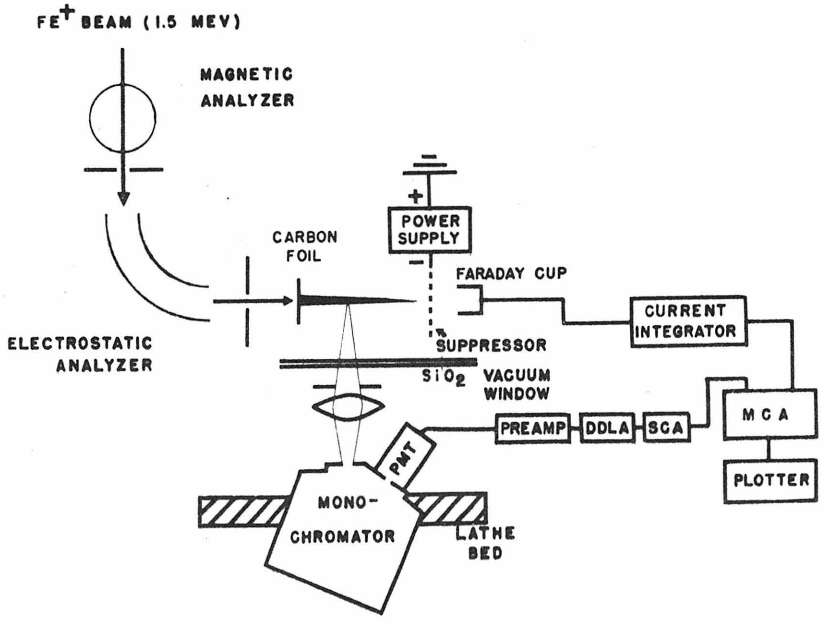

Fig. 1. Schematic diagram of excitation probability measurement apparatus.

---

* Supported in part by the Office of Naval Research [N00014-67-A-0094-0022] and the National Science Foundation [GP-28027].

† Presented the paper.

+ Present address: Physics Department, Kansas State University, Manhattan, Kansas 66502, U.S.A.

probabilities for these states with the hope that such numbers might suggest a mechanism for the excitation process. By measuring absolute intensities of these hydrogenic lines immediately adjacent to the foil with a spectrometer whose absolute calibration was known, we have deduced probabilities per emergent iron ion for the excitation of corresponding upper states, and report here the results of such measurements.

2. Experimental approach

The experimental arrangement, shown in fig. 1, was similar to that used in ref. 1. The beam was collected in a Faraday cup located 6" downstream from the exciter foil. Light from the excitated levels was dispersed with a 0.3 m McPherson monochromator (Model No. 218) equipped with a refrigerated EMI 6256S photomultiplier tube. The spectral scans used to deduce the excitation probabilities were taken at 90° to the particle beam. To determine the wavelength difference between closely-spaced lines, the beam was also viewed in the end-on configuration (0°), which reduced the Doppler width.

In order to extract population probabilities, one must determine the absolute intensities of spectral lines immediately beyond the foil, before cascading re-arrangements occur. We made measurements at 0.010" intervals over the first 0.2" of the decay curve and extrapolated to the origin. We then used theoretical hydrogenic transition probabilities to extract the probabilities, neglecting alignment effects in our analysis. (See appendix for detail.)

The absolute efficiency of the entire optical system was measured with a G.E. incandescent tungsten ribbon-filament lamp over the wavelength region included in this experiment (2500–6000 Å). Since different slit widths were used for scanning different lines, depending on the resolution required and on their strength, we checked that the quantity (intensity)/(slit width)^2 was constant. This was found to be the case as long as the slit width was greater than 50 μm. All the runs were performed using a spectral slit width greater than 2.7 Å.

In order to normalize our results to the number of emerging ions, thereby converting to a probability measurement, we measured the ratio ($\bar{Q}$) of the average current delivered to the Faraday cup with the foil in position to that with no foil. We found $\bar{Q} = 4.28 \pm 0.1$, in good agreement with the value 4.27 ± 0.06 calculated from equilibrium charge state data of Smith et al.^{2}).

3. Interpretation of spectra

In order to isolate states with the same n and different l, we must take into account the core polarization. Polarization of the ion core by the outer electron increases the binding energy of the one-electron Rydberg states in such a way as to shift the wavelengths of transitions going from $l \to l-1$ to the blue of their hydrogenic values. For transitions considered here the polarization was sufficient to allow partial resolution of $\Delta n = 1$ transitions into different l-components, or satellites. According to Edlén^{3}), the term value T can be expressed as:

$$T = T_{\mathrm{H}} + \Delta_{\mathrm{p}}, \tag{1}$$

where T_{H} is the hydrogenic value and Δ_{p} is the polarization energy.

$$T_{\mathrm{H}}(n, l) = \frac{\mathrm{Ry}\,\zeta^2}{n^2}\left[1 + \frac{\alpha^2\zeta^2}{n^2}\left(\frac{n}{l+\frac{1}{2}} - \frac{3}{4}\right)\right], \tag{2}$$

where Ry is the Rydberg constant (a function of the atomic mass A), ζ is the net charge on the atomic core, and α is the fine structure constant. The quantity Δ_{p} can be written as:

$$\Delta_{\mathrm{p}} = \alpha_{\mathrm{d}}\zeta^4\,\mathrm{Ry}\,\langle r_{nl}^{-4}\rangle, \tag{3}$$

where α_{d} is the dipole polarizability of the core and $\langle r_{nl}{}^{-4}\rangle$ is the expectation value of $1/r^4$ for an electron in a hydrogen atom state characterized by the quantum numbers n and l. Theoretical values for the core polarizabilities were not in general available for our cases. However, we were able to deduce experimental values by measuring deviations of observed wavelengths from theoretical hydrogenic ones. Our values for α_{d} are shown in table 1. α_{d} is given in units of $a^3{}_0$, where a_0 is the radius of the first Bohr orbit in hydrogen. Table 2 gives the observed wavelengths (λ_{obs}), the predicted wavelengths using the values of

TABLE 1

Experimentally derived values for the dipole polarizabilities, α_{d} (in units of $a^3{}_0$), for the ion core studies. The core charge is equal to the ion charge +1.

Core	α_{d}
Fe^{5+}	1.00
Fe^{6+}	0.80
Fe^{7+}	0.73
Fe^{8+}	0.51

TABLE 2

Calculated and observed wavelengths for Fe^{4+}–Fe^{7+} ions. λ_H = hydrogenic wavelength (no polarization correction); λ_{obs} = wavelengths observed in this experiment; λ^{calc}_{pol} = theoretical wavelengths with polarization correction.

Ion	Transition	λ_H (Å)	λ_{obs} (Å)	λ^{calc}_{pol} (Å)
Fe^{6+}	7i – 6h	2523.4	2514.5	2514.4
Fe^{7+}	8k – 7i	2976.2	2971.5	2972.4
	8h – 7g		2939.5	2942.0
Fe^{4+}	6h – 5g	2981.3	2956.5	2956.3
Fe^{5+}	9k – 7i	3138.9	3135.5	3136.5
Fe^{6+}	10l – 8k	3305.1	3303.0	3303.8
Fe^{5+}	7i – 6h	3434.1	3425.0	3423.9
	7h – 6g		3393.0	3400.3
Fe^{7+}	11m – 9l	3488.0	3487.0	3487.4
Fe^{4+}	10k – 7i	3501.0	3500.5	3499.1
Fe^{6+}	8k – 7i	3887.0	3882.5	3881.7
	8i – 7h		3870.5	3871.8
	8h – 7g		3839.5	3839.0
Fe^{7+}	9l – 8k	4340.8	4338.0	4338.4
	9k – 8i		4335.0	4334.8
	9i – 8h		4323.5	4324.8
Fe^{5+}	10l – 8k	4498.7	4496.8	4497.2
Fe^{4+}	9k – 7i	4518.7	4514.5	4515.8
Fe^{6+}	11m – 9l	4555.8	4553.0	4554.9
Fe^{4+}	7i – 6h	4944.8	4934.0	4932.6
	7h – 6g		4903.0	4901.8
Fe^{5+}	8k – 7i	5290.7	5285.5	5284.7
	8i – 7h		5274.0	5274.3
Fe^{6+}	9l – 8k	5669.6	5667.5	5666.0
	9k – 8i		5660.0	5661.0

α_d from table 1 (λ^{calc}_{pol}), and the theoretical hydrogenic wavelengths (λ_H) calculated from eq. (1), with no polarization correction. As an example of the spectra, fig. 2 shows the $n = 7 \to 6$ and $n = 6 \to 5$ transitions in Fe^{5+}. For $\Delta n = 1$ transitions, we denote the component from $l = l_{max} = (n-1)$ as λ_1, the satellite from $l = (l_{max} - 1)$ as λ_2, and so forth. If one interprets the major peaks as λ_1 transitions, a value of $\alpha_d = 0.8$ ($a^3{}_0$) gives values for ($\lambda - \lambda_H$) which are in agreement with ($\lambda_{obs} - \lambda_H$) within the experimental uncertainty. Evidence for the λ_2 satellites is clear for both cases, although λ_2 at 3393 Å appears to have considerable structure. In fact, all of the data show linewidths that are greater than the instrumental resolution, and several show resolvable structure beyond the l-splitting.

A recent calculation[4]) of α_d for the ground state of an 18-electron system with $Z = 26$ gives a value of 0.36 ($a^3{}_0$). Our measured value of (0.51 ± 0.1) ($a^3{}_0$) is too large to be consistent with this calculation, and suggests that the ion core is not in its ground state upon emerging from the foil. It is possible that the structure which we observe for the satellite lines may also be attributed to such an effect. Apparently, the interaction of the excited atomic core with the outer electron is not entirely described by the polarization concept based on a core with a well-defined, single polarizability.

The extraction of yields for λ_2 and higher l-satellites is particularly treacherous in view of the large range of wavelength over which their structure distributes the transition strength and the resulting low peak-to-background ratio. We have thus placed major emphasis on our results for λ_1, nothing however that the lower l-satellites (λ_2, λ_3, ...) are surprisingly weak.

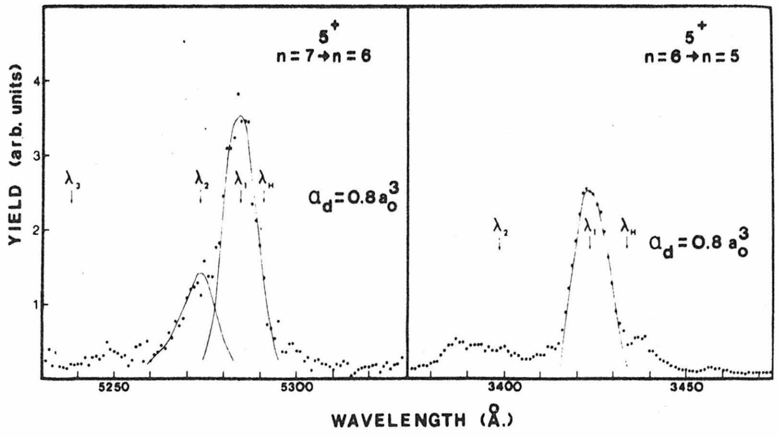

Fig. 2. The spectra of the $n = 7 \to 6$ and $n = 6 \to 5$ transitions in Fe^{5+} produced by foil excitation at an incident beam energy of 1.5 MeV. The solid curve indicates a visual fit to extract the transition strength. λ_H = wavelength computed using eq. (2) of text. λ_l ($l = 1, 2, \ldots$) = wavelengths computed using eqs. (1) – (3) of text for the different $l \to l-1$ components and α_d's from table 1.

4. Results

Fig. 3 shows the excitation probability, $P(n, l = n-1, q)$, for an ion with charge q to emerge from the foil in the hydrogenic state with principal quantum number n and orbital quantum number $l = n-1$, plotted as a function of n. P is normalized to the total number of ions emerging from the foil in charge state $(q+1)$, using the data from ref. 2, and is thus the excitation probability per emerging ion in the next higher charge state. We choose this normalization in order to facilitate comparison of our results with those from an electron capture model, as discussed below. The major source of error comes from the uncertainty in how to apportion the yields among closely-spaced l-satellites. The uncertainty in the relative efficiency calibration of the optical system is $\pm 30\%$ for $\lambda < 3500$ Å and $\pm 10\%$ for $\lambda > 3500$ Å, in addition to an overall $\pm 30\%$ uncertainty in the absolute calibration. The dashed lines show a variation with n of $1/n^3$.

In fig. 4, we show $P(n, l, q)$ as a function of l for a given n and q, normalized in the same manner as the data of fig. 3. The solid lines join data points having the same n. The uncertainties for the $l < n-1$ data are greater than those in fig. 4, due to the difficulties mentioned above. Typical error bars are shown on the data for $q = 4^+$, and are omitted for the rest of the data. The dashed lines show a probability proportional to $(2l+1)$, and the predominant feature to be noticed is that P generally increases with l faster than $(2l+1)$.

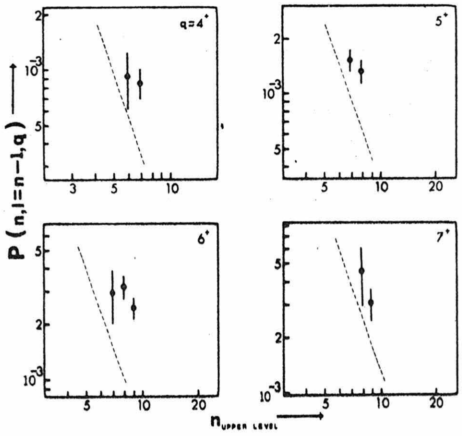

Fig. 3. Absolute excitation probabilities for Fe hydrogenic states at 1.5 MeV. The ordinate is the probability for an ion with charge q to emerge from the foil in a state with principal quantum number n_{upper}. Only the results for $\Delta n = 1$ transitions are shown. The dashed lines do not represent a fit to the data, but indicate a $1/n_u^3$ variation for comparison. The probabilities are normalized to the number of ions emerging from the foil with charge $(q+1)$.

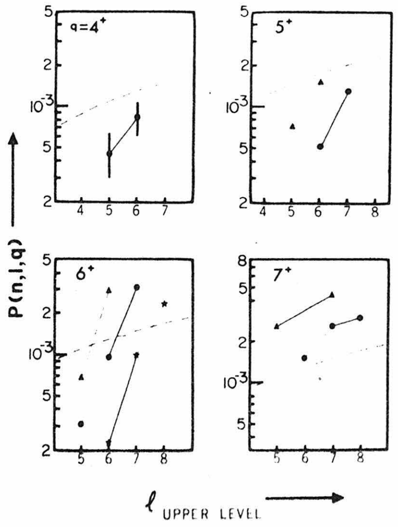

Fig. 4. Absolute excitation probabilities for Fe hydrogenic states at 1.5 MeV. The abscissa is l_{upper}. The solid lines join points having a common n_{upper}. The dashed lines indicate a $(2l+1)$ dependence. The errors are generally larger than in fig. 3, and are shown only for the case $q = 4^+$. The normalization is the same as in fig. 3.

5. Discussion

It has been suggested that[1]), since the mean radii of the high-n orbits encountered here are much larger than the interatomic spacing of the target atoms, such states are unlikely to have been formed within the foil but are more likely to have been produced at the surface. The very high multipolarity which a one-step surface excitation would require to move an electron to such high l suggests further that one look first to surface electron capture mechanisms.

On the basis of Born approximation calculations for electron capture of bound electrons by fast projectiles[5]), one would expect the excitation distribution among final states to follow a $1/n^3$) distribution. In the high velocity limit, such a distribution would also result from radiative capture of free electrons[6]). Trubnikov and Yavlinskii find this result also on the basis of an electron tunneling calculation[7]). We find it constructive to consider two simple models for electron capture: the first based on radiative recombination with free electrons at the foil surface, the second on capture from bound-state target atoms.

The cross-section for radiative capture of electrons by projectiles of charge Z is given by:

$$\sigma_{\text{cap}}(n, l) = 4.11 \times 10^{-20}\, g(n, l)\, \frac{(2l+1)}{n^5}\, \frac{Z^4}{E_\gamma E_e}\ [\text{cm}^2] \tag{4}$$

(deduced using the cross-section for photoionization and detailed balance), where $g\,(n, l)$ is a Gaunt factor defined in ref. 8, E_γ is the energy of the emitted photon (in eV), and E_e the energy of the captured electron (in eV) in the center-of-mass system (14.6 eV for 1.5 MeV Fe). If one asks that the capture takes place from an electron gas of density n_e by an ion with $Z = 6$ into a state $(n, l) = (6{,}5)$ with a probability of the order of 10^{-3} over a distance of 1 Å, then the required n_e is of order $10^{28}/\text{cm}^3$, which is quite unrealistically high. Even in the favorable case where we allow the gas to move with the ion, as has been observed by Harrison and Lucas with protons[9]), we must have $E_e \approx 10^{-3}$ in order to obtain $n_e \approx 10^{23}/\text{cm}^3$. For these reasons, we feel that the cross-section for radiative recombination in a free electron gas is too small to be able to account for our observed probabilities by such a process.

Non-radiative electron capture from bound atomic states has a much higher cross-section than does free electron capture. Nikolaev[10]) discusses non-radiative capture into states of high n (summed over l) by protons from various gases[11,12]). He also quotes experimental values for the cross-sections, and finds that the value of $\sigma_n n^3$ is roughly independent of the target atom from He to Ne for a projectile velocity (v) of 2.3×10^8 cm/s, the velocity of a 1.5 MeV Fe ion in our experiment. We have then calculated non-radiative capture probabilities using the following assumptions:

1) capture occurs during passage through the last row of carbon atoms;
2) the cross-section for electron capture by a proton is given by

$$\sigma_n n^3 = 1.6 \times 10^{-16}\ \text{cm}^2\ ^{10)}\,;$$

3) for ions of different Z and different v, the capture cross-section may be scaled following Nikolaev's semi-empirical scaling law[13]) for $\sigma_{Z \to (Z-1)}$:

$$\sigma_{Z \to (Z-1)} = \sigma_{1 \to 0} Z^2 \left(\frac{v}{2v_0}\right)^3;$$

this expression has been found to work well for *total* electron capture cross-sections[13,14]);

4) the distribution among l of the captures is proportional to $(2l+1)$ for fixed n, so that the capture probability summed over l is related to that for $l_{\max} = (n-1)$ by $P_{\text{TOT}}\ (n, q)\ \approx \frac{1}{2}n\, P\ (n, q, l_{\max})$.

TABLE 3

Comparison of measured population probabilities with the calculated surface capture probabilities for hydrogenic states (n, l) and different ion core charges (Z).

Z_{core}	n	Surface capture $= 0.06\, Z^2/n^3$	$\frac{1}{2}n \times P(n, l = n-1, Z = q+1)$
5	6	7.0×10^{-3}	2.5×10^{-3}
	7	4.4	2.7
6	7	6.3	4.9
	8	4.2	4.8
7	7	8.6	10.1
	8	5.7	13.3
	9	4.0	9.0
8	8	7.5	18.0
	9	5.3	7.0

Assumption (4) is doubtful in view of our results of fig. 4. Our calculated values for $P(n, q)$ are given in this simple model by the product of the scaled σ_n with the surface density of one layer of carbon atoms. The result is $P(n, q, Z = q+1) = 0.06\, Z^2/n^3$. This expression has been evaluated and compared with the corresponding experimental values in table 3. It is hardly surprising that close agreement is not obtained; however, we feel that it is significant that the proper order of magnitude for the probabilities is obtained. Although it is clear that a more detailed model calculation is needed, one which would include, for example, the l-dependence of the capture cross-section, we feel that this comparison supports the idea that such Rydberg states may be formed by electron capture at the foil surface.

The authors wish to acknowledge the many helpful discussions with the staff of the Kellogg Radiation Laboratory, in particular W. Whaling, A. Huffman and P. L. Smith.

Appendix

In order to calculate absolute excitation probabilities, we need a number of quantities:

1) the area under the wavelength scan corresponding to the line of interest, denoted by $Y(nl \to n'l')$, per unit electronic charge collected by the Faraday cup,

2) the efficiency, $\varepsilon(\lambda)$, of the optical system in the number of counts observed per photon emitted from an isotropic source,
3) the charge state fractions, $\phi_q(v)$, present in the post-foil beam, where $\sum \phi_q(v) = 1$,
4) the pass band of the monochromator, $\Delta\lambda$,
5) the velocity of the beam, v,
6) the theoretical transition probability for the particular transition being observed, $A\,(nl \rightarrow n'l')$,
7) the slit width, s, of the spectrometer, and
8) the magnification, M, of the condensing optics.

Since the length of the beam viewed was much smaller than the mean decay length of the states studied, we obtain

$$\frac{N_{nl}(q)}{N_0(q+1)} = \frac{Y(nl \rightarrow n'l')\bar{Q}(v)Mv}{A(nl \rightarrow n'l')s\,\phi_{q+1}(v)\,\varepsilon(\lambda)\,\Delta\lambda} = P(n, l, q),$$

where the yield, Y, has been extrapolated back to the foil ($t = 0$). $N_0\ (q+1)$ is the total number of ions in the charge state $(q+1)$, $N_{nl}(q)$ is the number of ions in the state (n, l) of charge q, and $\bar{Q}(v) = \sum_q q\phi_q(v)$.

References

1) W. N. Lennard, R. M. Sills and W. Whaling, Phys. Rev. **A6** (1972) 884.
2) P. L. Smith and W. Whaling, Phys. Rev. **188** (1969) 36.
3) B. Edlen, *Handbuch der Physik*, vol. 27 (ed. S. Flügge; Springer Verlag, Berlin, 1964) p. 80.
4) P. Vogel, private communication.
5) M. Brinkman and H. A. Kramers, Proc. Acad. Sci. Amst. **33** (1930) 973.
6) H. A. Bethe and E. E. Salpeter, *Handbuch der Physik*, vol. 35 (ed. S. Flügge; Springer Verlag, Berlin, 1957) p. 408.
7) B. A. Trubnikov and Yu. N. Yavlinskii, Zh. Eksperim. i Teor. Fiz. **52** (1967) 1638 [Soviet-Phys. JETP **25** (1967) 1089].
8) W. J. Karzas and R. Latter, Astrophys. J. Suppl. **6** (1961) 167.
9) K. G. Harrison and M. W. Lucas, Phys. Letters **33A** (1970) 142.
10) V. S. Nikolaev, Zh. Eksperim. i Teor. Fiz. **51** (1966) 1263 [Soviet-Phys. JETP **24** (1967) 847].
11) R. N. Il'in, V. A. Oparin, E. S. Solov'ev and N. V. Fedorenko, JETP Letters **2** (1965) 310 [p. 197 transl.].
12) R. N. Il'in, B. I. Kikiani, V. A. Oparin, E. S. Solov'ev and N. V. Fedorenko, Soviet-Phys. JETP **20** (1965) 835.
13) V. S. Nikolaev, Usp. Fiz. Nauk **85** (1965) 679 [Soviet-Phys. Usp. **8** (1965) 269].
14) J. R. MacDonald, S. M. Ferguson, T. Chiao, L. D. Ellsworth and S. A. Savoy, Phys. Rev. **A5** (1972) 1188.

Discussion

STONER: Can you tell me what minimum linewidths you were able to observe?

LENNARD: You mean end-on? About 3 Å, 4 Å, and 5 Å.

STONER: I see. One other question, concerning these states which were referred to as doubly-excited states earlier. Can you tell me whether you have looked at the possibilities for low-lying excited states of these cores, whether such states are likely, or whether this is just a hypothesis that needs more testing?

LENNARD: It is certainly true that the story is not over. In other words, the structure to the lines implies that there is another interaction that is the cause of the broadening. For everything other than the Fe^{7+}, that is with an 8^+ core, there would be low-lying states, and you would expect that this would possibly lead to a broadening of the lines, although quantitatively we haven't tried to make an estimate. We do not feel that it would be broad enough to give enough of a contribution. For Fe^{7+}, the lines are the narrowest, and the Fe^{8+} core will have the highest excitation. The lowest-lying excitation would be high because the core is closed. So that seemed reasonable. But we have not made a quantitative estimate of whether we could account for the splitting with some interaction energy of this kind.

GABRIEL: I think the model that you propose is in fact very close to the one that I was trying loosely to describe in a discussion comment earlier. One extension, I think, would get it even closer and that would be to consider the interaction not with the one lattice atom on the way out, but the interaction with the sea of lattice atoms and electrons. This of course would be very difficult theoretically, but I think it must be closer to the truth since the orbits of these iron ions that you are talking about I believe are somewhat larger than the lattice spacing of the atoms. Then if you incorporate this you have what I was loosely referring to as recombination. I did not intend this to imply radiative recombination.

LENNARD: I think you are right about that. I am sorry Dr. Garcia is not here. We were talking to him yesterday and he has some interesting ideas. This was somewhat of a crude theory. We were just trying to get the order of magnitude for the probabilities. That is, the reason we measured them was to see if they were of the order of 10^{-8} or something smaller. They are obviously not, and I am sure a lot more work could be done that could have a more realistic or more detailed theoretical basis.

BERRY: Did your relative excitation rates change with beam energy?

LENNARD: We did not vary the beam energy during this experiment. However, I have myself followed the intensity of the line as a function of energy and found that is just closely follows the charge-state curve. That is, it is as if the excitation function is either independent of energy or only weakly dependent upon energy.

COCKE: I would just like to make one comment. The reason for our taking such a simple model was primarily because we could do a calculation with it. I would like to ask Dr. Gabriel if he is optimistic on the possibility of doing calculations with more sophisticated pictures including the continuum in foil.

GABRIEL: I think perhaps you can approach it from the other end, and treat it as a statistical problem.

PEGG: We have studied the excitation functions for even high-lying states (the metastable autoionizing states) and we find that they follow the charge state cross section curves for helium-like iron, indicating the possibility of a capture to get the lithium-like iron. So this generally supports what you are saying. We believe it is a capture process, possibly from a metastable state in the helium-like iron.

NUCLEAR INSTRUMENTS AND METHODS 110 (1973) 385–390; © NORTH-HOLLAND PUBLISHING CO.

APPENDIX C

ABSOLUTE TRANSITION PROBABILITIES IN Ni I*

W. N. LENNARD†, W. WHALING, R. M. SILLS and W. A. ZAJC

California Institute of Technology, Pasadena, California, U.S.A.

The lifetimes of eight levels in Ni I have been measured by the beam-foil method with the aim of redetermining the solar abundance of nickel. Branching ratio measurements are in progress and absolute transition probabilities will be reported for 50 transitions from six levels in Ni I. Comparison with other recent measurements indicates (1) a gross discrepancy with the values of Corliss that increases with increasing excitation energy, similar to the discrepancy observed earlier for Fe I; (2) a 30% discrepancy with precise measurements by Marek that suggests cascading in our measurements of low levels; (3) support for the higher photospheric Ni abundance reported by the Kiel and Liège groups.

1. Introduction

This paper is a preliminary report on measurements in progress of the absolute transition probabilities for Ni I. After iron, nickel is the second most abundant of the iron-group elements and it is important to establish its abundance accurately. There is some disagreement among the recently published values displayed in table 1. We are remeasuring absolute transition probabilities in Ni I by an independent method to check the higher abundance that seems to be indicated by the most recent results.

2. Lifetime measurements

The method of measuring lifetimes by the beam-foil method is by now familiar. A description of our particular experimental arrangement may be found in the literature[1,2]). We mention below only those details peculiar to these nickel measurements.

Singly-charged Ni^+ ions were extracted from a thermal ion source containing either spectroscopically pure Ni metal, or later $NiCl_2$ when it was discovered that the molten nickel alloys with and corrodes the molybdenum walls of our ion source. Ni^+ beams of energy between 200 and 500 keV were used. The neutral fraction is greater at the lower energy but higher energies were also used to make certain that our lifetime measurements were independent of velocity. Carbon foils of nominal thickness 5–20 $\mu g/cm^2$ were used to make sure that our results were independent of foil thickness.

Spectrograms of the 500 keV beam covering the wavelength range 3400–6500 Å contained 98 lines (see table 2), of which 24 have been identified with known transitions in Ni I. We can identify no Ni II lines in this wavelength range even though the Ni II fraction is four times larger than the Ni I component at this beam energy. The two strongest lines in our spectrograms come from hydrogenic transitions, and in all we see seven such transitions in Ni^{3+}, Ni^{4+} and Ni^{5+}. The line identifications are based on wavelength. To qualify as certain, we require that at least one other line from the same upper level, or in the same multiplet, be observed with the proper relative intensity. For the hydrogenic transitions, identification also requires proper variation of intensity with beam energy over the range 500–1300 keV.

TABLE 1

Recent values for the photospheric nickel abundance: log ($N_{\mathrm{Ni}}/N_{\mathrm{H}}$)+12.

Abundance	Spectrum	Transition probability	Author
5.90±0.17	Ni I	Corliss[3]) reduced by factor 0.62 to fit Lawrence et al.[4])	Grevesse (1969), ref. 5
6.25±0.51	Ni I	Garz, Heise and Richter[6]) [normalized to Lawrence et al.[4])]	Garz et al. (1971), ref. 7
3.9 − 5.7 (may vary with λ)	Ni II	Warner[8])	Grevesse (1969), ref. 5
6.30±0.30	[Ni II]	Garstang[9])	Grevesse and Swings (1970), ref. 10

---

* Supported in part by the Office of Naval Research [N00014-67-A-0094-0022] and the National Science Foundation [GP-28027].

† Presented the paper.

TABLE 2

Wavelengths observed in the spectrum of a 444 keV Ni beam emerging from a $10\,\mu g/cm^2$ carbon foil. Identifications in parentheses are uncertain. Intensity estimates are by eye. Wavelengths in column 3 are from Moore[11]).

λ_{obs}(Å)	Int.	Identification (multiplet)	
3446.1	1	3446.3	Ni I (20)
3458.7	2	3458.5	(19)
3493.4	3	3493.0	(18)
3510.6	1	3510.3	(18)
3515.3	4	3515.1	(19)
3524.7	6	3524.5	(18)
3566.5	5	3566.4	(36)
3619.4	8	3619.4	(35)
3815.0	2		
3826.4	1		
3844.9	2	[3844.6	(181)]
		[3844.3	(137)]
3858.7	3	3858.3	(32)
3867.8	3	broad	
3881.7	2	[3881.9	Ni II (13)]
3889.3	3	[3889.7	Ni I (180)]
		[3889.7	(15)]
3897.6	4		
3900.0	4		
3905.7	1	3904.6	(29)
3917.2	4		
3928.5	1		
3934.2	3		
3940.2	3	[3938.8	(240)]
3949.5	3		
3957.3	1		
3964.3	1	broad	
3973.1	1	3973.6	(31)
4025.3	1	[4024.0	(170)]
		[4025.1	(240)]
4030.7	2	[4029.3	(170)]
4089.3	2		
4108.1	1		
4138.4	2	[4138.5	(237)]
4143.1	2	[4142.2	(212)]
		[4142.3	unclass.]
4183.4	2	broad	
4192.9	3	broad	
4279.6	2		
4288.5	2	4288.0	(178)
4296.6	3	4295.9	(178)
4306.3	1		
4313.1	4		
4327.4	5	[4325.6	(86)]
4333.1	1	[4331.6	(52)]
4342.6	4		
4357.5	6	[4355.9	(149)]
	blend	[4357.9	(256)]
		[4359.6	(86)]
4382.2	4	[4384.5	(186)]
4401.0	4	4401.5	(86)
4410.7	1	[4410.5	(88)]
4417.9	1		
4459.4	3	4459.0	(86)
4496.0	3		
4515.3	3	$n = 9–7$	Ni V
4547.1	1	4546.9	Ni I (261)
4630.0	9	$n = 6–5$	Ni IV
4646.6	3	[4647.4	Ni I (148)]
4665.1	3	[4664.3	(147)]
		[4666.9	(146)]
4679.7	4	$n = 8–6$	Ni IV
4702.6	1	[4701.5	Ni I (235)]
		[4703.8	(133)]
4714.9	2	4714.4	(98)
4755.4	1	[4754.7	(141)]
		[4756.5	(98)]
4855.1	3	4855.4	(130)
4903.2	6	7h – 6g	Ni V[a]
4910.4	5		
4935.4	8	7i – 6h	Ni V[a]
4959.6	1		
4981.8	4	4980.1	Ni I (112)
4991.2	2		
5018.8	4	5017.6	(111)
5039.9	4	5035.4	(143)
	blend	5039.2	(142)
5049.2	4	[5048.8	(195)]
		[5051.5	(144)]
5057.2	4	5058.0	(141)
5082.3	5	5081.1	(194)
	blend	5080.5	(143)
5104.8	2	[5102.9	(49)]
5143.3	4	[5142.7	(161)]
5170.8	2	5168.6	(112)
5184.1	1	5184.5	(159)
5199.0	1	[5197.1	(204)]
5227.7	1		
5286.0	5	$n = 8–7$	Ni VI
5332.2	3		
5351.4	3		
5444.2	4		
5480.8	4	[5480.8	Ni I (191)]
5509.8	1	5510.0	(190)
5528.5	5		
5540.8	1		
5579.2	5	5578.7	(47)
5630.3	2	[5628.3	(215)]
5662.8	2	5664.0	(272)
5686.6	1		
5712.2	2	5709.5	(46)
5753.5	1	5754.6	(68)
5764.9	1	[5760.8	(231)]
5799.3	1	[5796.0	(68)]
6344.0	2		
6370.9	1		
6400.8	4		
6441.0	1		
6471.6	4	$n = 10–8$	Ni V
6555.2	1		

---

[a] For identification of this line, see ref. 2.

Nine of the strongest well-resolved lines were selected for light-decay measurements. The light-decay curve for λ 3566.372 Å is shown in fig. 1. The upper curve indicates the photon counting rate at the peak of the line profile, corrected for a time-dependent background of ≈ 2 counts/s. The lower curve shows the counting rate 10 Å away from the peak where we measure the continuous background that must be subtracted to find the yield from the line alone. After subtracting this background, a further correction was made to allow for ions scattered outside the field of view of the monochromator. At the maximum distance from the foil, scattering reduced the counting rate by 15%. This counting loss due to scattering was always less than the statistical uncertainty of the data points. The energy loss in the foil was calculated using Lindhard's[12]) value for the nuclear contribution, and interpolating the results of Hvelplund[13]) to find the electronic stopping.

The light-decay curves, corrected and converted to the time variable, were fitted using a standard non-linear least squares computer fit to a one- or two-exponential function. Our values for the mean lifetimes are shown in table 3. Some of the mean lifetimes have been measured only once at this time and are enclosed in parentheses; subsequent measurements may alter these results slightly. The 15% uncertainty assigned to the mean lifetimes takes into account the statistical uncertainty from the least square fit, the spread of different values obtained in repeated measurements, and the velocity uncertainty due to uncertain foil thickness. The replenishment factor $R(0)$ is defined[14]) as $(1-\tau_1/\tau_2)\,C_2/(C_1+C_2)$, where the light-decay curve is fitted to the expression $C_1 \exp(-t/\tau_1) + C_2 \exp(-t/\tau_2)$. $R(0)$ is a measure of the cascading contribution; $R(0) = 0$ indicates a one-exponential fit.

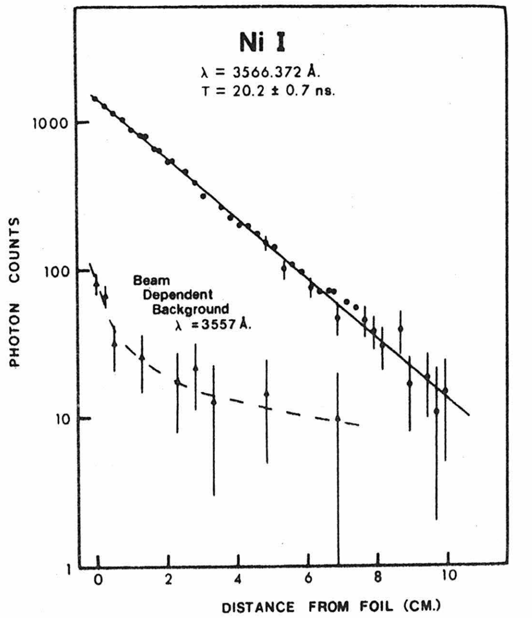

Fig. 1. Light-decay plot for λ 3566.372 Å at 400 keV incident beam energy, 350 keV beam energy emerging from 10 μg/cm^2 carbon foil. Angle of observation is 90°, and pass band of the monochromator is 2.7 Å fwhm. The 1 cm-length of entrance slit is normal to the beam velocity. The lower curve is taken 10 Å off the peak and is a measure of the continuous background that has been subtracted from the upper curve to find the yield due to the line alone.

TABLE 3

Mean lifetimes of nine levels in Ni I are listed in column 3. The cascade parameters τ_2 and $R(0)$ are defined in the text. Values from Marek[15]) are listed in column 6.

λ(Å)	Level	τ_1 (ns)	Cascade parameters		
			τ_2 (ns)	$R(0)$	τ_{Marek} (ns)
3525	$z^3P_2^0$	13.2	59 ± 20	0.034	9.91 ± 0.2
3515	$z^3F_3^0$	14.4 ± 2	39 ± 23	0.055	12.26 ± 0.25
3493	$z^3P_1^0$	(9.8 ± 1.5)	35 ± 6	0.15	9.72 ± 0.19
3458	$z^3F_2^0$	(16.4 ± 2)	44 ± 20	0.037	
3619	$z^1F_3^0$	13.8 ± 2	29 ± 11	0.049	
3566	$z^1D_2^0$	20.4 ± 3	0	0	
5018	e^5F_5	(9.2 ± 1.5)	58 ± 16	0.17	
4980	e^3G_5	(19.1 ± 3)	0	0	

The very precise values measured by Marek[15]) by the resonant light-scattering method are also listed in table 3. For two of the three levels the agreement is satisfactory but for the $z^3P_2^0$ level our value is 33% greater than Marek's. One is tempted to suspect that cascading into this level is increasing the beam-foil value. This suspicion is strengthened by the fact that the λ 4855.414 Å transition which populates the $z^3P_2^0$ level is present with intensity 3 in table 2. None of the other transitions which populate our other levels appears in table 2 with this strength. Consequently it may be that for this level cascading is influencing our measured lifetime even though the replenishment ratio is not unusually large. We intend to measure the lifetime of the λ 4855.414 Å transition to see if it will shed any light on this discrepancy. For the moment we consider our lifetime for the $z^3P_2^0$ level preliminary and do not assign an uncertainty to it.

3. Branching ratios

The 5 m Paschen–Runge spectrometer used to

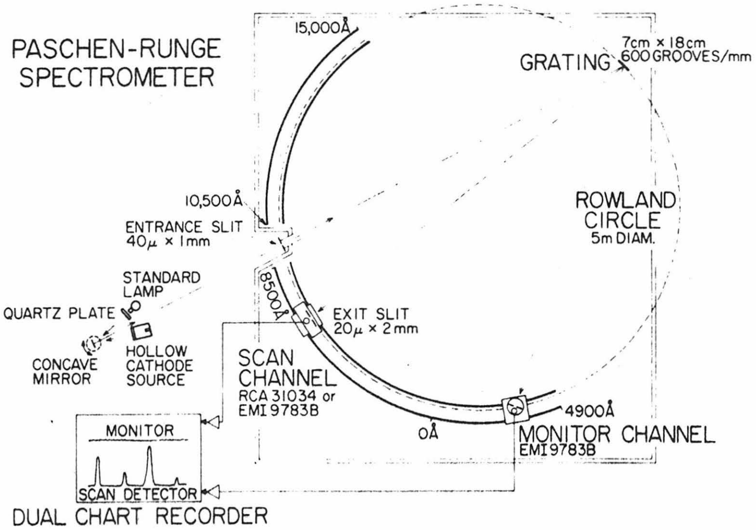

Fig. 2. Two-channel Paschen–Runge spectrometer and source arrangement used for branching ratio measurements. Both monitor channel and scanning channel move along the circular track. The monitor channel is shown in its position to detect the spectrum diffracted to the right of the grating normal, while the scanning channel detects the left spectrum which is enhanced by the grating blaze.

measure branching ratios is shown in fig. 2. This spectrometer has two detecting channels: The monitor channel is set on a strong, unblended line from the upper level under investigation and monitors continuously the excitation of that level in the source. The scanning detector then scans across each line from the upper level to measure the relative intensities. The monitor channel can move anywhere along the track but is normally placed to detect the spectrum on the right of the grating normal while the scan channel detects the left spectrum that is enhanced by the grating blaze. This arrangement avoids mechanical interference when two close wavelengths are to be compared.

A two-channel strip chart records the current from both photomultipliers simultaneously. The branching ratio can be read directly from the chart after correcting for the detection efficiency of the scanning channel. The detection efficiency is measured by imaging the tungsten-strip filament of our standard lamp on the entrance slits of the spectrometer and observing the response of the scanning detector to the known radiance of the standard lamp at different wavelengths. The efficiency of the monitor need not be known. The quartz plate in front of the standard lamp is identical to the window on the hollow cathode source and equalizes the optical paths.

Once the detector sensitivity has been calibrated, the hollow-cathode of our source may be focussed on the entrance slits by rotating the concave mirror. The source is similar to that described earlier[16]) for iron measurements, except that the cathode is spectroscopic Ni electrode with a 3 mm diam. × 25 mm long cavity on its axis. With He or Ar at about 1 torr to maintain the discharge, we have been able to detect all of the transitions with $\lambda < 8500$ Å from the levels we have studied. At present, our scanning is limited to

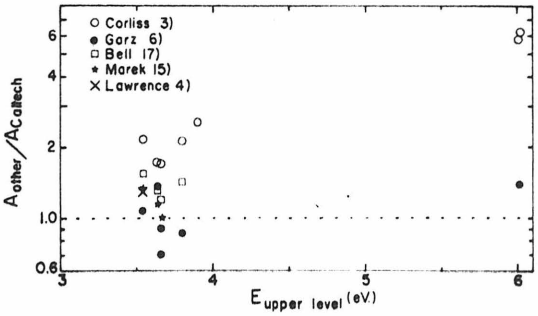

Fig. 3. Other measurements of the transition probability are compared with our results in this plot of $A_{other}/A_{Caltech}$ as a function of the excitation energy of the upper level. For Corliss[3]) and Marek[15]) we compare the total transition probability ΣA, summed over all of the transitions out of the upper level.

TABLE 4

Branching ratios and transition probabilities for six levels in Ni I. Wavelengths in column 3 are from Moore[11]). The other values in the last column are from Corliss[3]) except as noted by superscripts: (a) Garz et al.[6]); (b) Bell et al.[17]); (c) Laurent and Weniger[18]); (d) Lawrence et al.[4]).

Upper level (energy)	τ (10^{-9} s)	λ (Å)	Lower level	Branching ratio (%)	Trans. prob. (10^8 s^{-1})	Other values (10^8 s^{-1})
$z^3P^0_2$ (3.54 eV)	13.2	3524.541	a^3D_3	88	0.66	1.45, 1.03^b, 0.76^c 0.86^b
		3610.462	a^3D_2	10	0.076	0.15, 0.083^a, 0.095^c
		3670.427	a^3F_3	0.83	0.0063	0.018
		3722.484	a^3D_1	0.58	0.0044	0.015, 0.0065^c
		3793.608	a^3F_2	0.15	0.00110	0.0046
		3973.562	a^1D_2	0.30	0.0023	0.0013
		6643.641	b^1D_2	0.14	0.00108	0.0042
		7714.27	a^3P_2	0.13	0.00098	0.0056
		7788.95	a^3P_1	0.083	0.00063	0.0034
$z^3F^0_3$ (3.64 eV)	14.4	3409.578	a^3F_4	0.39	0.0027	0.0096
		3433.558	a^3D_3	18	0.124	0.26, 0.18^a, 0.22^c
		3515.054	a^3D_2	53	0.37	0.63, 0.49^b, 0.13^c
		3571.869	a^3F_3	20	0.138	0.11
		3688.415	a^3F_2	0.47	0.0032	0.012
		3858.301	a^1D_2	8.4	0.059	0.18
		6327.603	b^1D_2	0.052	0.00036	0.00024
		7291.48	a^3P_2	0.032	0.00022	0.00068
$z^3P^0_1$ (3.66 eV)	9.8	3492.956	a^3D_2	82	0.83	1.3, 0.58^a, 1.0^b, 0.63^c
		3597.705	a^3D_1	15.1	0.154	0.29, 0.14^a, 0.15^c
		3664.095	a^3F_2	1.36	0.0139	0.49
		3831.690	a^1D_2	1.13	0.0115	0.037
		6256.365	b^1D_2	0.176	0.00180	0.0041
		6767.778	a^1S_0	0.30	0.0030	0.012
		7197.07	a^3P_2	0.079	0.00080	0.0039
		7261.94	a^3P_1	0.074	0.00075	0.0038
		7414.51	a^3P_0	0.093	0.00095	0.0040
$z^3F^0_2$ (3.80 eV)	16.4	3286.946	a^3D_3	0.49	0.0030	0.011
		3361.556	a^3D_2	6.1	0.037	0.086
		3413.478	a^3F_3	6.4	0.039	0.078
		3458.474	a^3D_1	78	0.47	1.00, 0.39^a, 0.65^b, 0.13^c
		3519.766	a^3F_2	5.8	0.035	0.12
		3674.15	a^1D_2	3.7	0.022	
		5847.010	b^1D_2	0.018	0.00011	0.00036
$z^1D^0_2$ (3.90 eV)	20.4	3200.423	a^3D_3	0.14	0.00069	0.0045
		3271.118	a^3D_2	0.82	0.0040	0.020
		3320.257	a^3F_3	6.6	0.032	0.099, 0.10^c
		3362.806	a^3D_1	0.179	0.00088	0.0045
		3420.741	a^3F_2	0.171	0.00084	0.0024
		3566.372	a^1D_2	87	0.43	1.12
		5578.734	b^1D_2	0.088	0.00043	0.0025
		6314.666	a^3P_2	4.9	0.024	0.0045
		6364.597	a^3P_1	0.055	0.00026	0.00095
e^5F_5 (6.01 eV)	9.2	4401.547	$z^5D^0_4$	31	0.33	2.27
		4714.421	$z^5G^0_6$	37	0.40	2.17, 0.56^a
		4786.541	$z^5G^0_5$	14.6	0.159	0.84
		4900.97	$z^5G^0_4$	0.41	0.045	0.023
		5017.591	$z^5F^0_5$	16.3	0.178	0.94
		5157.993	$z^5F^0_4$	0.48	0.0052	0.035
		5265.748	$z^3F^0_4$	0.30	0.0033	0.016
		6452.77	$y^3F^0_4$	$<$ 0.03	0.00032	0.0061

wavelengths below 8500 Å because of the geometry of the entrance slit. Two of the Ni levels that we have lifetimes for have branches between 8500 and 11 500 Å. We intend to measure these with the McPherson 218 spectrometer equipped with an S-1 phototube.

4. Results and discussion

Preliminary results for the branching ratios and transition probabilities for the levels completed so far are listed in table 4. Also listed in the table are other recent measurements, and these are compared with our results in fig. 3 in which we plot ($A_{\text{other}}/A_{\text{CIT}}$) as a function of the excitation energy of the upper level. To compare our results with those of Corliss³), we have plotted $\sum A_{\text{C}}/\sum A_{\text{CIT}}$ rather than the individual ratios to suppress the spread. The discrepancy between our results and those of Corliss appears to increase with increasing excitation energy, similar to the discrepancy found earlier for Fe I. Lifetimes for additional high energy levels are needed to confirm this conclusion. The values of Bell, Pacquette, and Wiese¹⁷), plotted as open squares, and the values of Garz et al.⁶), plotted as closed circles, are relative values normalized to the same absolute values of Lawrence et al.⁴). It would appear that these sets of values are 10 to 20% higher than our values and Marek's. Our disagreement with Marek from the $z^3\text{P}_2^0$ level is also evident on the figure.

We conclude that the higher abundance derived by Garz⁷) is based on correct transition probabilities, while the lower value derived by Grevesse⁵) is based on transition probabilities that are too large. We will derive an abundance value from our data when our measurements are complete.

References

1) W. Whaling, R. B. King and M. Martinez-Garcia, Astrophys. J. **158** (1969) 389.
2) W. N. Lennard, W. Whaling and R. M. Sills, Phys. Rev. **A6** (1972) 884.
3) C. H. Corliss, J. Res. Nat. Bur. Std. **A69** (1965) 87.
4) G. M. Lawrence, J. K. Link and R. B. King, Astrophys. J. **141** (1965) 293.
5) N. Grevesse, Ph. D. Thesis (University of Liège, 1969).
6) T. Garz, H. Heise and J. Richter, Astron. Astrophys. **9** (1970) 296.
7) T. Garz, Astron. Astrophys. **10** (1971) 175.
8) B. Warner, Mem. Roy. Astron. Soc. **70** (1967) 165.
9) R. H. Garstang, Monthly Notices Roy. Astron. Soc. **118** (1958) 238.
10) N. Grevesse and P. J. Swings, Solar Phys. **13** (1970) 19.
11) C. E. Moore, Nat. Bur. Std. Tech. Note 36 (1959).
12) J. Lindhard, M. Scharff and H. E. Schiott, Kgl. Danske Videnskab. Selskab, Mat. Fys. Medd. **33**, no. 14 (1963).
13) P. Hvelplund and B. Fastrup, Phys. Rev. **165** (1968) 408.
14) L. J. Curtis, H. G. Berry and J. Bromander, Phys. Scripta **2** (1970) 216.
15) J. Marek, Astron. Astrophys. **17** (1972) 83.
16) W. Whaling, M. Martinez-Garcia, D. L. Mickey and G. M. Lawrence, Nucl. Instr. and Meth. **90** (1970) 363.
17) G. D. Bell, D. R. Pacquette and W. L. Wiese, Astrophys. J. **142** (1966) 559.
18) J. Laurent and S. Weniger, J. Quant. Spectrosc. Radiative Transfer **10** (1970) 315.

APPENDIX D - SPECTROMETER CALIBRATION

D.1 INTRODUCTION

In order to measure the relative intensities, or branching ratios (defined in equation (4.1) of all the transitions which depopulate an upper atomic level, the relative detection efficiency, $\varepsilon(\lambda)$, of the detector system must be known as a function of wavelength, λ . The term "system" refers to the spectrometer itself, a photomultiplier tube, and any optical components such as lenses that may be required.

As discussed in Section 4, two separate detection systems were used in this work: the Paschen-Runge system (see Figure 5) was used in the visible wavelength region $3200Å \leq \lambda \leq 8000Å$, and the McPherson system, using the monochromator and associated components described in Section 4.2, was used in the near infrared region $\lambda \geq 9600Å$. The McPherson spectrometer had been calibrated <u>absolutely</u> with a different grating, photomultiplier and geometry as described in Appendix B.

In order to measure the response of a detector system to incident light, a standard light source of known spectral radiance is required. For the wavelength region $2500Å < \lambda < 12000Å$, a tungsten filament lamp is the most commonly used source and was used in this work.

D.2 STANDARD LAMP SOURCE

An incandescent tungsten ribbon-filament lamp was used for the calibration of both optical systems. This source is a General Electric Type 30A/T24/17 commercial lamp having a tungsten ribbon filament

(SR-8A type) centered about 8 to 10 cm behind a fused silica window 3 cm in diameter. Our lamp, serial number EPUV-1130, was calibrated for operation at a current of 35 amp a.c. by the Eppley Laboratory, Inc., Newport, R.I. Initially, for the Paschen-Runge system, the lamp was calibrated from 2500Å to 7500Å. For the McPherson measurements, it was necessary to have the lamp recalibrated from 2500Å to 15000Å . The lamp calibrations were performed by Eppley by comparing the lamps to standards which in turn had been calibrated against National Bureau of Standards (NBS) lamps. Stair *et al.* (1960) have asserted that the uncertainty in the calibration of the NBS standards is approximately 8% at λ2500 and 3% at the upper wavelength limits. We have assumed that the Eppley calibrations have these same uncertainties.

Smith (1972) has illustrated a typical plot of the spectral radiance of these tungsten filament lamps as a function of wavelength. The monochromatic brightness, expressed in microwatts/ steradian/ nanometer/(cm^2 of source), was converted to the units of photons/sec/ steradian/nanometer/(cm^2 of source); the peak lamp output in these units corresponds to a wavelength of about 11,270Å (which implies a blackbody temperature of 2570°K).

The ammeter used to measure the current through the lamp was calibrated to ±0.1% by R. G. Marcley (Caltech). The regulated lamp power supply and the associated electrical equipment have been discussed in detail by Smith (1972).

D.3 CALIBRATION PROCEDURE

The number of photons $n(\lambda)$ detected by the spectrometer system per unit time at a wavelength λ is given by

$$n(\lambda) = I(\lambda)\ \varepsilon_0(\lambda)\Omega \qquad (D.1)$$

where $I(\lambda)$ = intensity of the source in units of photons/sec/steradian/Å/(cm^2 of source),

$\varepsilon_0(\lambda)$ = absolute detection efficiency of the spectrometer system (a dimensionless quantity) which is a measure of the number of photons counted as a fraction of the number of incident photons, and

Ω = a geometrical factor which determines how many photons actually enter the spectrometer relative to the number that are emitted by the source in all directions; Ω includes such quantities as the spectrometer slit widths and the magnification of the detector optical elements. The individual terms which make up Ω are listed by Martinez-Garcia (1971a).

Since only the <u>relative</u> efficiency $\varepsilon(\lambda)$ is required, we define

$$\varepsilon_0(\lambda) = C_1\ \varepsilon_1(\lambda) \qquad (D.2)$$

where C_1 is a constant independent of wavelength. For both systems, the calibrations were performed using the photomultiplier tubes in the current mode. The observed current at a particular wavelength $i(\lambda)$ is proportional to the number of photons reaching the detector so long as the photomultipliers are operated in the linear regions ($i < 1\ \mu$amp). If we define

$$i(\lambda) = C_2\ n(\lambda)\ \varepsilon_2(\lambda) \qquad (D.3)$$

where $\varepsilon_2(\lambda)$ is the efficiency of the photomultiplier tube itself for a given set of operating conditions, then we obtain, using (D.2) and (D.1),

$$\varepsilon(\lambda) = \frac{i(\lambda)}{I(\lambda)} \tag{D.4}$$

where $\varepsilon(\lambda) = C_1 C_2 \Omega\, \varepsilon_1(\lambda)\, \varepsilon_2(\lambda)$ is the desired quantity. The right side of (D.4) contains the observable quantity $i(\lambda)$ and the known quantity $I(\lambda)$ obtained from the Eppley calibration. Since we are interested in comparing intensities at two different wavelengths, λ_1 and λ_2, the relative detection efficiencies are related by

$$\frac{\varepsilon(\lambda_1)}{\varepsilon(\lambda_2)} = \frac{i(\lambda_1)\, I(\lambda_2)}{i(\lambda_2)\, I(\lambda_1)} \tag{D.5}$$

The constants and the geometrical factor cancel out in comparing efficiencies at different wavelengths.

Care was taken to ensure that the geometry of the detecting systems was the same for both the efficiency calibrations and the branching ratio measurements. The quartz plate shown in Figure 6 in front of the standard lamp is identical to the window on the hollow cathode sources and acts to equalize the optical path lengths.

It is desirable to overfill the grating with light to ensure that the results are independent of local grating defects and of variation in the solid angle subtended by the grating as a function of wavelength. Although this was possible for the Paschen-Runge system, it was not for the McPherson system. The particular source geometry allowed only about 85% illumination of the grating. A mask was inserted to cover 20% of the grating so that the exposed area was the limiting factor in the subtended solid angle. Since the geometry used in the calibration was duplicated in the measurements, the results of the efficiency determination are valid.

For both optical systems, the image of the source was magnified by about a factor of 4-5 to ensure that the entrance slit of the spectrometer was smaller than this image.

If there is excessive water vapor in the laboratory atmosphere, errors may result at the wavelengths of water vapor absorption bands. This absorption could be a serious problem for measurements made in the near infrared region of the spectrum. For the McPherson system, the path length between the standard lamp and the detector was the same as between the hollow cathode source and the detector. The relative humidity in the laboratory was monitored and found to be 49(±5)% throughout the time that measurements were being made. The source-detector path length was about 220 cm. For the strongest water vapor absorption band in our wavelength range, which occurs at about 12,000Å, the total transmission along the optical path was determined to be 98.6 ± 0.1% using the data given in Allen (1964). The uncertainty is due to the variation of the relative humidity during the measurements. We can safely conclude that there is no systematic error in the near infrared results caused by atmospheric water vapor absorption.

The Paschen-Runge system was calibrated in first order using the RCA C31034 photomultiplier tube in the wavelength region $\lambda\lambda 3000$-8000. The detector response, $\varepsilon(\lambda)$, is a slowly varying function of λ, reaching its maximum at about $\lambda 4500$. The values of $\varepsilon(\lambda 3000)/\varepsilon(\lambda 4500)$ and $\varepsilon(\lambda 8000)/\varepsilon(\lambda 4500)$ were found to be 0.74 and 0.27 respectively.

The relative detection efficiency measurement is probably accurate to ±15% for $3000Å < \lambda < 8000Å$, which is the range spanned by the branching ratio measurements in the visible region described in Section 4.

The standard lamp emits 13 times as many photons per unit time at 11,000Å as it does at 5000Å. For the calibration of the McPherson system, it was necessary to change the entrance slit width to ensure that the photomultiplier current did not exceed 1 μamp for the very long wavelengths. In order to make the calibration independent of slit width, measurements were made at the intermediate wavelength of 7400Å with different slit widths to allow normalization of the data taken with $\lambda < 6000$Å to that with $\lambda > 9500$Å.

The McPherson system was <u>not</u> calibrated over the entire wavelength region λλ4500-11,300 because it was felt that future use of this detector system would entail a recalibration with a somewhat different geometry. The near infrared lines for which branching ratios were needed (see Table 4) were located far from the nearest line in wavelength from the same upper level to which the intensities were normalized. Thus, the system was calibrated only for selected wavelength regions of particular interest to this work.

The results of the measurement of the relative detection efficiency for the McPherson system are shown in Figure 20. The dashed curve has been drawn only to aid the reader. All of the near infrared wavelengths for which branching ratio measurements were made (see Sections 4.4.2 and 4.4.10) were located in regions between the data points shown in Figure 20. The solid curve represents the typical spectral response of the HTV R406 photomultiplier tube itself in the absence of the auxiliary spectrometer components such as lenses and the grating.

The accuracy of the efficiency measurements for the McPherson system is about ±15%. The use of a Corning 2-64 filter (see Section 4.2) to eliminate second order lines with $\lambda < 6000Å$ introduces a further ±5% uncertainty when comparing very red lines, for which the filter was used, to the lines in the visible region, for which it was not used. The transmission of the 2-64 filter as a function of wavelength was accomplished by using lines produced by Pen-Ray lamps filled with Xe, Ne, Kr and Ar, and by using a commercial Fe-Ne hollow cathode source. The transmission varied smoothly from 90% ± 3% at λ7400 to 84% ± 4% at λ11200. Since only upper limits were obtained for the strengths of the near infrared transitions (see Tables 6 and 14), further analysis of uncertainties in the efficiency determination for the McPherson system does not seem worthwhile.

APPENDIX E - BEAM SCATTERING

An ion beam impinging on a thin exciter foil will be scattered at a small angle from the incident direction due to encounters with the atoms in the target material. When the light radiated by the excited atoms or ions is viewed at 90^0 to the beam direction downstream from the foil, some correction must be made to account for those particles which have been scattered outside the field of view of the detector system.

The atomic collisions within the foil have two effects on the moving beam particles: (i) the moving particles lose kinetic energy in the collisions, and (ii) the direction of motion of the moving particles is changed through a scattering angle ϕ (laboratory angle). The correction to the light decay measurements to take account of the effect (i) above is discussed in Section 3.4.

Blaugrund (1966) has calculated the expectation value of $\cos \phi$, denoted $\langle \cos \phi \rangle$, using the energy loss theory of Lindhard _et al_. (1963) and the scattering theory of Lewis (1950). We have modified Blaugrund's results to include the electronic energy loss measurements of Hvelplund and Fastrup (1968), as discussed in Section 3.4, for the particular case of Ni incident on C. The theoretical results of Lindhard _et al_. (1963) have been used for the specific nuclear energy loss rate, $(dE/dx)_n$.

The maximum scattering angle in the laboratory frame is 12^0 for Ni on C in a single collision. If we denote the beam axis as the z axis, x and y are then the transverse directions. We have approximated the angular distribution in one of the transverse directions, which we call the x direction, by a Gaussian function

$$P(\phi_x) = \frac{1}{\sqrt{2\pi}\,\sigma_\phi} \exp(-\,\phi_x^2/2\,\sigma_\phi^2) \tag{E.1}$$

where $\sigma_\phi = \langle\phi_x^2\rangle^{1/2}$ and $\langle\phi_x^2\rangle = \langle\phi^2\rangle/2$ because of the cylindrical symmetry of the beam. We can relate the small angle ϕ to $\langle\cos\phi\rangle$ by the relation $\langle\cos\phi\rangle = 1 - \langle\phi^2\rangle/2$.

Blaugrund's result is

$$\langle\cos\phi\rangle = \exp(G(r)I/2r) \tag{E.2}$$

where $r = M_1/M_2$ is the ratio of the masses of the incident and target particle, $G(r)$ is a slowly varying analytic function of r which can be easily calculated, and

$$I = \int_{E_0}^{E_f} \frac{\left(\frac{dE}{dx}\right)_n}{E\left(\frac{dE}{dx}\right)}\, dE \tag{E.3}$$

The numerator of the integrand in (E.3) is the theoretical specific nuclear loss rate of Lindhard <u>et al</u>., and $dE/dx = (dE/dx)_n + (dE/dx)_e$ is the <u>total</u> energy loss rate as a function of the instantaneous energy, E . The subscript "e" refers to the electronic contribution to dE/dx . The limits of integration extend from the initial particle energy E_0 to the final energy E_f after traversing the foil. The integral (E.3) must be evaluated numerically.

The results of Blaugrund have been compared to those obtained by a Monte Carlo calculation (Currie 1969) and good agreement was found

Page 98 is missing.

A further correction which averages the projected path lengths (and times) for those particles scattered at a finite angle onto the path direction $\phi_x = 0$ could have been made. Since this would introduce only a very small change, of order $<\phi_x^2>$, no correction has been made.

APPENDIX F - FURTHER INVESTIGATION OF THE LIFETIME OF THE $z^3P_2^o$ LEVEL IN Ni I

The relationship between the lifetimes of different levels within the same term permits a further investigation of the discrepancy between our measured value of τ for the $z^3P_2^o$ level with the value reported by Marek (1972). Marek's values for the lifetimes of the $z^3P_1^o$ and $z^3P_2^o$ levels are shown in Table 3 along with our results. The measurements agree very well for the $z^3P_1^o$ level.

In this appendix, we discuss a method by which we can determine the ratio of the two lifetimes $\tau(z^3P_1^o)/\tau(z^3P_2^o)$. This quantity will be compared to the CIT and Marek's experimental ratios in order to find an inconsistency in either set of values.

We have used the method suggested by Roberts _et al_. (1973a) to relate the lifetimes of levels within the same term, $\tau(SLJ_1)$ and $\tau(SLJ_2)$. Combining expressions (2.6) and (4.2), we obtain

$$\frac{\tau_{J_1}}{\tau_{J_2}} = \frac{N_{J_1} \sum_{J_k} I_{J_2J_k}}{N_{J_2} \sum_{J_i} I_{J_1J_i}} \qquad \text{(F.1)}$$

where the summations extend over all branches $\lambda_{J_1J_i}$ and $\lambda_{J_2J_k}$ which depopulate the levels J_1 and J_2 respectively.

In order to relate the population densities N_{J_1} and N_{J_2} for different levels within a term, we have assumed that $N_J \propto 2J + 1$. Although the population mechanism in the hollow cathode source may depend on L and S in a complex manner, the assumption of a statistical population among levels that differ only in the quantum number J is probably a good one.

It is also necessary to postulate the population distribution as a function of excitation energy. The distribution that has been assumed is

$$\frac{N_{J_1}}{N_{J_2}} = \frac{g_{J_1} \exp(\alpha E_{J_1})}{g_{J_2} \exp(\alpha E_{J_2})} \tag{F.2}$$

where α is a parameter to be experimentally determined for the hollow cathode source, $g_{J_1} = 2J_1 + 1$ and $g_{J_2} = 2J_2 + 1$ are the statistical weights of the two levels within the same term having excitation energies E_{J_1} and E_{J_2} above the ground state. By combining expressions (F.1) and (F.2) we obtain the desired result

$$\frac{\tau_{J_1}}{\tau_{J_2}} = \frac{g_{J_1} \sum\limits_{J_k} I_{J_2J_k}}{g_{J_2} \sum\limits_{J_i} I_{J_1J_i}} \exp[\alpha(E_{J_1} - E_{J_2})] \tag{F.3}$$

Since the branching ratios for all the decays that depopulate the levels of interest have been measured as described in Section 4, it is only necessary to measure the relative intensities of <u>one</u> branch from each upper level to obtain the summation factors. Specifically, using (4.1)

$$\sum_{J_i} I_{J_1J_i} = \frac{I_{J_1 1}}{R_{J_1 1}} \tag{F.4}$$

where $I_{J_1 1}$ is the observed intensity of the branch at wavelength $\lambda_{J_1 1}$ and $R_{J_1 1}$ is the branching ratio. <u>Any</u> branch from level J_1 may be used.

The emitted intensity of a spectral line is

$$I_{JJ'}(\lambda_{JJ'}) = K\, g_J\, A_{JJ'}\, \exp(\alpha\, E_J) \tag{F.5}$$

The factor K is a function of the partition function, the total number of atoms or ions in the source, a gemoetrical factor characteristic of the spectrometer, the optical depth within the source and the source operating conditions. We have shown in Section 4.5 that self-absorption in our hollow cathode source is negligible, thus making the optical depth factor unimportant. If the source operating conditions are held constant, the other factors mentioned above will be the same for the two levels (SLJ_1) and (SLJ_2). The constant factor K will cancel out in taking the ratio (F.1).

If we plot $\ln(I_{JJ'}/g_J A_{JJ'})$ as a function of E_J (the excitation potential of the upper level), the slope of the curve will be given by α from equation (F.5).

The particular energy level structure of Ni I (discussed in Section 4.7) has made it possible to measure $I_{JJ'}$ as a function of E_J only for levels with $3.54\text{ eV} \leq E_J \leq 3.90\text{ eV}$. The results are shown in Figure 22. Each datum point represents an average over a few of the branches from the same upper level in order to avoid scatter due to uncertainties in the branching ratio data. The source was run at large currents and gas pressures to make the lines as intense as possible, but taking care to maintain the discharge as steady as possible. Frequent checks were made to see that the observed intensities did not change as a function of time by more than ±5%. It was found convenient to observe branches that were not far separated in wavelength since this would avoid systematic errors caused by uncertainties in the relative detector efficiency calibration (see Appendix D).

The solid line in Figure 22 shows the best straight line fit to the data, yielding a value of $\alpha = -2.36 \pm 0.50\ \text{eV}^{-1}$. The uncertainty has been visually estimated. If we were to associate the quantity α with the Boltzmann "temperature" expression $-(kT)^{-1}$, we would obtain a "temperature" of $4920 \pm 1000^{\circ}$K.

In order to test this method of determining lifetime ratios for levels within a term, we have applied the technique to the three levels of the z^3F^o term $(J = 2,3,4)$ in Ni I for which Marek has measured two lifetimes $(J = 3$ and $J = 4)$ and we have measured two lifetimes $(J = 2$ and $J = 3)$.

The results for both the z^3F^o and z^3P^o terms are shown in Table 25. The uncertainties in the results for the actual lifetime measurements are obtained from the values given in Table 3. The uncertainties in the ratios determined from the technique described in this appendix are due to the uncertainty in the empirically derived value of α (see Figure 22).

The results for the z^3F^o levels indicate that this method yields ratios in good agreement with the values obtained from the lifetime measurements. In fact, we could have obtained a value for α by fitting our observations to the actual lifetimes, but we would then have not had a consistency check on the technique.

It should be noted that the only significant assumption in this technique is that concerning the statistical population of the levels within a term. The functional dependence of the population distribution on excitation energy described by equation (F.2) could have been chosen to be a multi-parameter one. In that case, our data would have been fitted to a different functional form, but the derived parameters would yield approximately the same result for the lifetime ratios.

For the $z^3P^o_{1,2}$ levels, τ_1(Marek) = 9.72 ± 0.19 ns and τ_1(CIT) = 9.7 ± 1.5 ns as shown in Table 3. The 20% discrepancy in the measurements of τ_2 has <u>not</u> been resolved by this technique. The empirically determined ratio of the two lifetimes $\tau_1/\tau_2 = 0.91 \pm 0.06$ indicates that the lifetime of the $z^3P^o_2$ level is 10.7 ± 0.7 ns, which is between the measured values of Marek and this thesis.

The method described here to determine the lifetime of the $z^3P^o_2$ level in Ni I yields a result which is in agreement with both Marek's and CIT's measured values within the uncertainties of the measurements.

APPENDIX G - SEARCH FOR UNCLASSIFIED LINES IN THE SPECTRUM OF Ni I

The line spectra of elements are important tools in spectrochemical and astrophysical studies. Using the technique outlined in Section 2 to isolate those as yet unclassified transitions most likely to be present in the Ni I spectrum, a search of the hollow cathode spectrum was made to confirm or negate their presence in our source. The Kitt Peak Preliminary Solar Atlas (Testerman 1973) was also searched to determine if such transitions were present in the solar spectrum.

The results of this investigation are shown in Table 26. The wavelengths in column 1 are predicted wavelengths in air computed from equation (2.7). Only upper limits were determined for the strengths of all of the lines except for λ4633.

The measured equivalent width of λ4633 is $W^{KP} = 3.17$ mÅ. Using our measured gf value of 0.0028 (see Table 12), we obtain a solar Ni abundance of $A_{Ni} = 6.13 \pm 0.15$ using equation (5.2) which assumes that the line is weak enough to be on the linear part of the curve of growth (see Section 5). In actual fact, the curve of growth analysis actually gives a lower limit on the abundance since the straight line portion of the curve is approached asymptotically by the weak lines. We consider this value to be in agreement with the abundance 6.29 ± 0.2 found in Section 6.4. The predicted wavelength, λ4633.031, is very close to the solar line observed at λ4633.037. The above evidence is sufficient to positively identify λ4633 as a new transition in Ni I.

To make positive identifications for those very weak lines with solar intensities smaller than 1 mÅ would be a questionable practice. Since only upper limits for the transition probabilities of these "lines" have been determined, no other certain assignments can be made.

REFERENCES

1. C. D. Allen and A. S. Asaad, Mon. Not. Roy. Astron. Soc. 117, 36 (1957).
2. C. W. Allen, Astrophysical Quantities (Oxford University Press, Inc., New York, 1964).
3. L. H. Aller, Astrophysics--The Atmospheres of the Sun and Stars, 2nd ed. (Rowland Press, New York, 1963).
4. H. D. Babcock and C. E. Moore, The Solar Spectrum: λ6600-λ13495, Carnegie Inst. Wash. Publ. 579 (1947).
5. B. Baschek, T. Garz, H. Holweger and J. Richter, Astron. and Astrophys. 4, 229 (1970).
6. S. Bashkin, Nucl. Instr. and Meth. 90, 3 (1970).
7. G. D. Bell, D. R. Paquette and W. L. Wiese, Astrophys. J. 143, 559 (1966).
8. F. Bernhard, P. Krygel, R. Manns and S. Schwabe, in Atomic Collisions in Solids IV, S. Andersen, K. Björkqvist, B. Domeij and N. G. E. Johansson, eds. (Gordon and Breach, New York, 1972).
9. P. R. Bevington, Data Reduction and Error Analysis for the Physical Sciences (McGraw-Hill, Inc., 1969).
10. A. E. Blaugrund, Nucl. Phys. 88, 501 (1966).
11. M. Born and E. Wolf, Principles of Optics, 3rd (revised) edition (Pergamon Press, 1965).
12. R. P. Boyle, Bull. Amer. Astron. Soc. 4, 268 (1972).
13. J. H. Brand, C. L. Cocke and B. Curnutte, Nucl. Instr. and Meth. 110, 127 (1973).
14. J. W. Brault, C. D. Slaughter, A. K. Pierce and R. S. Aikens, Solar Phys. 18, 366 (1971).
15. G. Brückner, Photometric Atlas of the Near Ultraviolet Solar Spectrum, 2988Å-3629Å (Göttingen, Vandenhoeck & Ruprecht, 1960).

16. A. G. W. Cameron, Explosive Nucleosynthesis, D. N. Schramm and W. D. Arnett, eds. (University of Texas Press, Austin, Texas, 1973).

17. R. Cayrel and J. Jugaku, Annales d'Astrophys. 26, 495 (1963).

18. C. L. Cocke, A. Stark and J. C. Evans, Astrophys. J. 184, 653 (1973).

19. C. L. Cocke, private communication (1974).

20. M. Cohen and A. Dalgarno, Proc. Roy. Soc. A 280, 258 (1964).

21. C. Corliss and W. Bozman, Natl. Bur. Std. Monograph, No. 53 (1962).

22. C. H. Corliss, J. Res. Natl. Bur. Std. 69A, 87 (1965).

23. C. R. Cowley and A. P. Cowley, Astrophys. J. 140, 713 (1964).

24. C. Cowley, Astrophys. J. 143, 352 (1966).

25. R. J. S. Crossley and A. Dalgarno, Proc. Roy. Soc. A 286, 510 (1965).

26. P. T. Cunningham and J. K. Link, J. Opt. Soc. Am. 57, 1000 (1967).

27. W. M. Currie, Nucl. Instr. and Meth. 73, 173 (1969).

28. L. J. Curtis, Amer. J. Phys. 36, 1123 (1968).

29. L. J. Curtis, H. G. Berry and J. Bromander, Physica Scripta 2, 216 (1970).

30. K. S. de Boer, H. Olthof and S. R. Pottasch, Astron. and Astrophys. 16, 417 (1972).

31. L. Delbouille, L. Neven and G. Roland, Photometric Atlas of the Solar Spectrum from λ3000 to λ10000 (Institut d'Astrophysique de l'Université de Liège, 1973).

32. W. Demtröder, Z. Physik 166, 42 (1962).

33. B. Edlén, Physica Scripta 7, 93 (1973).

34. G. Elste, Astrophys. J. 148, 857 (1967).

35. G. Elste, Solar Phys. 3, 106 (1968).

36. J. C. Evans and L. Testerman, to be published in Solar Phys.(1974).

37. R. A. Fisher, W. C. Knopf, Jr. and F. E. Kinney, Astrophys. J. 130, 683 (1959).

38. R. Foy, Astron. and Astrophys. 18, 26 (1972).

39. R. H. Garstang, Mon. Not. Roy. Astron. Soc. 118, 238 (1958).

40. T. Garz, H. Holweger, M. Kock and J. Richter, Astron. and Astrophys. 2, 446 (1969).

41. T. Garz, H. Heise and J. Richter, Astron. and Astrophys. 9, 296 (1970).

42. T. Garz, Astron. and Astrophys. 10, 175 (1971).

43. O. Gingerich, R. Noyes, W. Kalkofen and Y. Cuny, Solar Phys. 18, 347 (1971).

44. L. Goldberg, E. Müller and L. Aller, Astrophys. J. Suppl. 5, 1 (1960).

45. L. Goldberg, R. A. Kopp and A. K. Dupree, Astrophys. J. 140, 707 (1964).

46. N. Grevesse, Ph. D. Thesis, University of Liège, Belgium (1969).

47. N. Grevesse and J. P. Swings, Solar Phys. 13, 19 (1970).

48. G. R. Harrison, M.I.T. Wavelength Tables (Wiley and Sons, Inc., New York, 1939).

49. G. R. Harrison, M.I.T. Wavelength Tables (Revised), (M.I.T., Cambridge, Mass., 1969).

50. H. Holweger, Zeit. f. Astrophys. 65, 365 (1967).

51. M. C. E. Huber and W. H. Parkinson, Astrophys. J. 172, 229 (1972).

52. E. Hulpke, E. Paul and W. Paul, Z. Physik 177, 257 (1964).

53. K. Hunger, Zeit. f. Astrophys. 39, 38 (1956).

54. P. Hvelplund and B. Fastrup, Phys. Rev. 165, 408 (1968).

55. L. Kay, Physica Scripta 5, 138 (1972).

56. R. B. King, Astrophys. J. 108, 87 (1948).

57. T. K. Krueger and S. J. Czyzak, Astrophys. J. 144, 1194 (1966).

58. J. Laurent and S. Weniger, J. Quant. Spectrosc. Rad. Transfer 10, 315 (1970).

59. G. Lawrence, J. Link and R. King, Astrophys. J. 141, 293 (1965).

60. H. W. Lewis, Phys. Rev. 78, 526 (1950).

61. J. Lindhard, M. Scharff and H. E. Schiott, Kgl. Danske Videnskab. Selskab. Mat. Fys. Medd. 33, 1 (1963).

62. G. D. Magnuson, C. E. Carlston, P. Mahadevan and A. R. Comeaux, Rev. Sci. Instr. 36, 136 (1965).

63. J. Marek, Astron. and Astrophys. 17, 83 (1972).

64. M. Martinez-Garcia, Ph.D. Thesis, California Institute of Technology (1971a).

65. M. Martinez-Garcia, W. Whaling, D. L. Mickey and G. M. Lawrence, Astrophys. J. 165, 213 (1971b).

66. D. Mihalas, Stellar Atmospheres (W. H. Freeman and Company, San Francisco, 1970).

67. M. Minnaert, G. F. W. Mulders and J. Houtgast, Photometric Atlas of the Solar Spectrum, 3332Å to 8771Å (Amsterdam, Schnabel, 1940).

68. O. C. Mohler, A. K. Pierce, R. R. McMath and L. Goldberg, Photometric Atlas of the Near Infrared Solar Spectrum, λ8465 to λ25242 (University of Michigan Press, Ann Arbor, 1950).

69. O. C. Mohler, A Table of Solar Spectrum Wavelengths, 11,984Å to 25,578Å (University of Michigan Press, Ann Arbor, 1955).

70. C. E. Moore, A Multiplet Table of Astrophysical Interest, rev. ed. (Princeton University Observatory, 1945).

71. C. E. Moore, An Ultraviolet Multiplet Table, Natl. Bur. Std. Circular 488 (1950).

72. C. E. Moore, M. G. J. Minnaert and J. Houtgast, The Solar Spectrum 2935Å-8770Å, Natl. Bur. Std. Monograph 61 (1966).

73. C. E. Moore, Atomic Energy Levels, Natl. Bur. Std. Circular 467, Vol. II (1971).

74. G. M. Nikolsky, Solar Phys. 6, 399 (1969).

75. A. K. Pierce and J. B. Breckinridge, The Kitt Peak Table of Photographic Solar Spectrum Wavelengths, Kitt Peak Natl. Obs. Contr. 559 (1973).

76. S. Pottasch, Bull. Astr. Inst. Netherlands 19, 113 (1967).

77. G. Racah, Phys. Rev. 62, 438 (1942).

78. J. R. Roberts, T. Andersen and G. Sorensen, Astrophys. J. 181, 567 (1973a).

79. J. R. Roberts, T. Andersen and G. Sorensen, Astrophys. J. 181, 587 (1973b).

80. J. R. Roberts, T. Andersen and G. Sorensen, Nucl. Instr. and Meth. 110, 119 (1973c).

81. J. E. Ross and L. H. Aller, Solar Phys. 25, 30 (1972).

82. C. Roth, J. Res. Natl. Bur. Std. 74A, 715 (1970).

83. H. A. Rowland, Astrophys. J. 1, 2, 3, 4, 5 (1895-97).

84. A. G. Shenstone, J. Res. Natl. Bur. Std. 74A, 801 (1970).

85. P. L. Smith and W. Whaling, Phys. Rev. 188, 36 (1969).

86. P. L. Smith, W. Whaling and D. L. Mickey, Nucl. Instr. and Meth. 90, 47 (1970).

87. P. L. Smith, Ph.D. Thesis, California Institute of Technology (1972).

88. P. L. Smith and W. Whaling, Astrophys. J. 183, 313 (1973).

89. I. I. Sobel'man, Introduction to the Theory of Atomic Spectra (Pergamon Press, New York, 1972).

90. R. Stair, R. G. Johnston and E. W. Halbach, J. Res. Natl. Bur. Std. 64A, 291 (1960).

91. J. W. Swensson, W. S. Benedict, L. Delbouille and G. Roland, The Solar Spectrum from λ7498-λ12016: Measures and Identifications (Institut d'Astrophysique de l'Université de Liège, Belgium, 1970).

92. R. Takens, Astron. and Astrophys. 5, 244 (1970).

93. L. Testerman, private communication (1973).

94. S. Tolansky, High Resolution Spectroscopy (Methuen and Co., London, 1947).

95. A. Unsöld, Physik der Sternatmospharen (Springer-Verlag, Berlin, 1955).

96. H. C. Urey, Quart. J. Roy. Astron. Soc. 8, 23 (1967).

97. H. van Driel, Ph.D. Thesis, University of Utrecht (1935).

98. B. Warner, Observatory 85, 72 (1965).

99. B. Warner, Mem. Roy. Astr. Soc. 70, 165 (1967).

100. B. Warner, Mon. Not. Roy. Astr. Soc. 138, 229 (1968).

101. R. C. Weast, Handbook of Chemistry and Physics, 49th ed. (The Chemical Rubber Co., Cleveland, Ohio, 1968).

102. W. Whaling, R. B. King and M. Martinez-Garcia, Astrophys. J. 158, 389 (1969).

103. K. O. Wright, Pub. Dom. Astrophys. Obs. 8, 1 (1948).

TABLE 1

Recent values for the solar Ni abundance:

$A_{Ni} = \log_{10}(N_{Ni}/N_H) + 12.00$.

TABLE 1

Recent values for the solar Ni abundance: $A_{Ni} = \log_{10}(N_{Ni}/N_H) + 12.0$

A_{Ni}	Authors	Comments
5.9 ± 0.6	Goldberg, Müller and Aller (1960)	Photosphere, Ni I. Relative gf's normalized by f-sum rule.
5.49	Warner (1965)	Photosphere, Ni I. gf's from Corliss (1965).
5.69 ± 0.10	Cowley (1966)	Photosphere, Ni I. gf's from Corliss (1965).
6.24	Urey (1967)	Meteorites (assuming $A_{Si} = 7.55$).
6.51	Pottasch (1967)	Corona, Ni X-XIII (EUV lines). Theoretical gf's from Cohen and Dalgarno (1964), Crossley and Dalgarno (1965).
5.08	Warner (1968)	Photosphere, Ni II. gf's from Warner (1967).
6.3 ± 0.3	Nikolsky (1969)	Corona, Ni X-XV (EUV lines). Theoretical gf values.
5.90 ± 0.17	Grevesse (1969)	Photosphere, Ni I. Normalized gf's from Corliss (1965) to scale of Lawrence *et al*. (1965).
6.3 ± 0.3	Grevesse and Swings (1970)	Photosphere, [Ni II]. Theoretical gf's from Garstang (1958).
6.41	Takens (1970)	Photosphere, Ni I. Corrects gf's from Corliss and Bozman (1962).
6.25 ± 0.15	Garz (1971)	Photosphere, Ni I. Relative gf's from Garz *et al*. (1970) normalized to absolute scale of Lawrence *et al*. (1965).
5.68 ± 0.30	Boyle (1972)	Photosphere, Ni I. W's from Kitt Peak Atlas; source of gf's not cited.

TABLE 1 - (Continued)

A_{Ni}	Authors	Comments
6.6	de Boer, Olthof and Pottasch (1972)	Corona, [Ni XII-XVI]. Theoretical gf's from Krueger and Czyzak (1966).
6.18	A. G. W. Cameron (1973)	Meteorites.

TABLE 2

Beam velocity measurements using the Doppler shift method for λ3619.392. The calculated velocity was obtained by subtracting the energy lost in nuclear collisions (Lindhard 1963) and in electronic collisions (Hvelplund and Fastrup 1968) from the known incident energy. The uncertainty in the calculated velocities is due to the ±40% uncertainty in the thickness of the carbon foils (refer to Figure 2 and to page 14).

TABLE 2

	Directly Measured Velocity ($\times 10^7$ cm/sec)	Calculated Velocity ($\times 10^7$ cm/sec)
$E_{incident} = 410$ keV $t = 10\ \mu gm/cm^2$	10.8 ± 0.4	10.5 ± 0.3
$E_{incident} = 307$ keV $t = 5\ \mu gm/cm^2$	9.6 ± 0.2	9.7 ± 0.3

TABLE 3

Results of the beam-foil lifetime measurements for 11 levels in Ni I. The incident beam energy (in keV) and foil thickness (in $\mu gm/cm^2$) are shown in parentheses for the individual measurements. The uncertainties for each measurement are those assigned in the curve fitting program. The mean values, $<\tau>$, were calculated by taking a weighted average of all measurements. The overall uncertainty is obtained after a consideration of all possible sources of error (see pages 26 and 27). The values of R(0) are representative values over the individual measurements. The values without superscripts given in column 6 are found by summing the transition probabilities of Corliss (1965) for all branches for which he has given results. Other values are noted by superscripts: (a) Marek (1972); (b) Brand *et al*. (1973). The upper level designations are given as they appear in Moore (1971) with the excitation energy (E_u) in eV.

TABLE 3

$\lambda(\mathring{A})$	Upper Level (E_u)	Beam Energy (keV), Foil Thickness ($\mu gm/cm^2$)	τ (ns)	$<\tau>$ (ns)	$<R(0)>$	τ^{others} (ns)
3446.263	$z^3D_2^o$ (3.70)	(359,10) (432, 5)	16.73 ± 0.83 19.44 ± 0.42	18.9 ± 2.0	0.0	9.50,23.0 ± 4.6[b]
3458.474	$z^3F_2^o$ (3.80)	(357,10) (432, 5)	16.20 ± 1.07 16.46 ± 1.03	16.3 ± 2.0	0.04	7.76,22.9[b]
3492.956	$z^3P_1^o$ (3.66)	(432, 5) (410,10)	9.59 ± 1.15 9.71 ± 0.82	9.7 ± 1.5	0.15	5.83, 9.72 ± 0.19[a], 12.8 ± 3.2[b]
3858.301		(410,10)	11.56 ± 1.95			
3515.054	$z^3F_3^o$ (3.63)	(432, 5) (349,20) (410,10) (317,10)	15.80 ± 2.20 14.79 ± 1.42 13.41 ± 1.61 15.12 ± 1.36	14.2 ± 2.5	0.06	8.33, 12.26 ± 0.25[a], 16.2 ± 4.2[b]
3524.541	$z^3P_2^o$ (3.54)	(305,10) (410,10) (486,10) (313, 5) (432, 5)	12.47 ± 1.02 13.42 ± 1.80 13.08 ± 0.94 11.72 ± 0.71 12.03 1.05	12.2 ± 2.5	0.05	6.04, 9.91 ± 0.20[a], 14.0 ± 2.5[b]
3566.372	$z^1D_2^o$ (3.90)	(410,10) (317,10)	19.97 ± 0.69 20.31 ± 1.03	20.1 ± 2.0	0.0	7.90, 19.1 ± 4.4[b]
3619.392	$z^1F_3^o$ (3.84)	(410,10) (317,10) (432, 5)	12.32 ± 1.24 14.94 ± 1.00 13.69 ± 1.35	13.9 ± 2.0	0.05	6.95, 15.2 ± 1.5[b]
4295.888	g^3F_3 (6.72)	(432,10) (359,10)	11.92 ± 0.83 10.26 ± 0.65	10.9 ± 2.0	0.0	3.90

TABLE 3 - Continued

$\lambda(\text{Å})$	Upper Level (E_u)	Beam Energy (keV), Foil Thickness (μgm/cm^2)	τ (ns)	$<\tau>$ (ns)	$<R(0)>$	τ^{others} (ns)
4855.414	e^3P_2 (6.09)	(410,10) (317,10)	12.62 ± 0.73 11.92 ± 1.37	12.4 ± 2.0	0.14	3.11
4980.161	e^3G_5 (6.10)	(410,10) (282, 5) (432,10)	17.58 ± 0.92 18.91 ± 0.62 15.88 ± 0.72	17.6 ± 2.0	0.0	3.19
4714.421 5017.591	e^5F_5 (6.01)	(359,10) (307, 5)	7.89 ± 0.66 9.06 ± 1.26	8.15 ± 1.5	0.13	1.60

TABLE 4

Decay modes for the 11 levels whose lifetimes were measured. Also listed are the branches for 2 levels whose lifetimes were measured by Marek (1972) and for which we have measured branching ratios. The RMT number and level designation are from Moore (1945), and the configuration and energy (in cm^{-1}) are from Moore (1971). Transitions without corresponding multiplet numbers have their sources referenced:

[a] Ni I has two transitions at λ3548.185 (RMT No. 3 and RMT No. 20),

[b] Observed by Fisher _et_ _al_. (1959),

[c] Tabulated by Corliss (1965),

[d] CIT predicted wavelength as discussed in Section 2 (see Appendix G),

[e] Observed by Mohler (1955),

[f] Listed by Swensson _et_ _al_. (1970),

[g] Listed by Harrison (1939),

[*] Misprint in Multiplet Table (Moore 1945): λ5039.259 → λ5039.359 .

TABLE 4

Upper Level (E_u)	RMT No.	Wavelength (Å)	Lower Level Designation (E_ℓ)	
$z^3D^o_z$	20	3367.892	a^3D_3	205
(29889)	20	3446.263	a^3D_2	880
	6	3500.852	a^3F_3	1332
	20	3548.185[a]	a^3D_1	1713
	6	3612.741	a^3F_2	2217
	33	3775.572	a^1D_2	3410
	45	6108.121	b^1D_2	13521
	64	7001.57	a^3P_2	15610
	64	7062.97	a^3P_1	15734
$z^1F^o_3$	8	3221.652	a^3F_4	0
(31031)	22	3243.058	a^3D_3	205
	22	3315.663	a^3D_2	880
	8	3366.168	a^3F_3	1332
	8	3469.486	a^3F_2	2217
	35	3619.392	a^1D_2	3410
	46	5709.559	b^1D_2	13521
	66	6482.811	a^3P_2	15610
	81	11196.70	a^1G_4	22102
$z^3P^o_2$	18	3524.541	a^3D_3	205
(28569)	18	3610.462	a^3D_2	880
	4	3670.427	a^3F_3	1332

TABLE 4 - (Continued)

Upper Level (E_u)	RMT No.	Wavelength (Å)	Lower Level Designation	(E_ℓ)
	18	3722.484	a^3D_1	1713
	4	3793.608	a^3F_2	2217
	31	3973.562	a^1D_2	3410
	43	6643.641	b^1D_2	13521
	62	7714.27	a^3P_2	15610
	62	7788.95	a^3P_1	15734
$z^3P^o_1$	18	3492.956	a^3D_2	880
(29501)	18	3597.705	a^3D_1	1713
	4	3664.095	a^3F_2	2217
	31	3831.690	a^1D_2	3410
	43	6256.365	b^1D_2	13521
	57	6767.778	a^1S_0	14729
	62	7197.07	a^3P_2	15610
	62	7261.94	a^3P_1	15734
	62	7414.51	a^3P_0	16017
$z^3F^o_3$	5	3409.578	a^3F_4	0
(29321)	19	3433.558	a^3D_3	205
	19	3515.054	a^3D_2	880
	5	3571.869	a^3F_3	1332
	5	3688.415	a^3F_2	2217

TABLE 4 - (Continued)

Upper Level (E_u)	RMT No.	Wavelength (Å)	Lower Level Designation (E_ℓ)	
	32	3858.301	a^1D_2	3410
	44	6327.603	b^1D_2	13521
	63	7291.48	a^3P_2	15610
	-	13849.49[b]	a^1G_4	22102
$z^3F_2^o$	19	3286.946	a^3D_3	205
(30619)	19	3361.556	a^3D_2	880
	5	3413.478	a^3F_3	1332
	19	3458.474	a^3D_1	1713
	5	3519.766	a^3F_2	2217
	32	3674.150	a^1D_2	3410
	44	5847.010	b^1D_2	13521
	-	6716.14[c]	a^3P_1	15734
$z^1D_2^o$	23	3200.423	a^3D_3	205
(31442)	23	3271.118	a^3D_2	880
	9	3320.257	a^3F_3	1332
	23	3362.806	a^3D_1	1713
	9	3420.741	a^3F_2	2217
	36	3566.372	a^1D_2	3410
	47	5578.734	b^1D_2	13521
	67	6314.666	a^3P_2	15610
	67	6364.597	a^3P_1	15734

TABLE 4 - (Continued)

Upper Level (E_u)	RMT No.	Wavelength (Å)	Lower Level Designation	(E_ℓ)
e^3G_5	99	4565.45	$z^5G^o_6$	27261
(49159)	-	4633.031[d]	$z^5G^o_5$	27580
	99	4740.165	$z^5G^o_4$	28068
	112	4849.12	$z^5F^o_5$	28542
	112	4980.161	$z^5F^o_4$	29084
	143	5080.523	$z^3F^o_4$	29481
	176	5499.39	$z^3G^o_4$	30980
	228	6176.813	$y^3F^o_4$	32973
	258	6421.507	$z^1G^o_4$	33590
	-	16945.47[e]	$w^3F^o_4$	43259
e^5F_5	86	4401.547	$z^5D^o_4$	25754
(48467)	98	4714.421	$z^5G^o_6$	27261
	98	4786.541	$z^5G^o_5$	27580
	98	4900.97	$z^5G^o_4$	28068
	111	5017.591	$z^5F^o_5$	28542
	111	5157.993	$z^5F^o_4$	29084
	141	5265.748	$z^3F^o_4$	29481
	226	6452.770	$y^3F^o_4$	32973
g^3F_3	150	4009.984	$z^3F^o_3$	29321
(54251)	150	4035.96	$z^3F^o_4$	29481
	150	4230.39	$z^3F^o_2$	30619

TABLE 4 - (Continued)

Upper Level (E_u)	RMT No.	Wavelength (Å)	Lower Level Designation	(E_ℓ)
	178	4295.888	$z^3G^o_4$	30980
	-	4382.87^c	$z^1D^o_2$	31442
	178	4450.13	$z^3G^o_3$	31786
	235	4698.408	$y^3F^o_4$	32973
	235	4729.291	$y^3F^o_3$	33112
	254	4817.847	$y^3D^o_3$	33501
	260	4838.651	$z^1G^o_4$	33590
	235	4843.53	$y^3F^o_2$	33611
	254	4976.71	$y^3D^o_2$	34163
	-	5371.33^c	$y^1F^o_3$	35639
	272	5664.017	$y^1D^o_2$	36601
	295	9689.35	$x^1D^o_2$	43933
	284	10061.29	$y^3G^o_4$	44315
	-	10226.14^f	$w^3D^o_2$	44475
	289	10321.10	$w^3F^o_3$	44565
e^3P_2 (49159)	-	4444.55^c	$z^5D^o_3$	26666
	-	4597.65^c	$z^5D^o_2$	27415
	130	4855.414	$z^3P^o_2$	28569
	142	5039.359*	$z^3F^o_3$	29321
	130	5085.479	$z^3P^o_1$	29501
	159	5129.383	$z^3D^o_3$	29669

TABLE 4 - (Continued)

Upper Level (E_u)	RMT No.	Wavelength (Å)	Lower Level Designation (E_ℓ)	
	159	5187.86	$z^3D^o_2$	29889
	-	5262.83[c]	$z^5F^o_2$	30163
	189	5514.80	$z^1F^o_3$	31031
	203	5642.660	$z^1D^o_2$	31442
	217	6180.093	$z^1P^o_1$	32982
	227	6230.115	$y^3F^o_3$	33112
	246	6384.697	$y^3D^o_3$	33501
	-	6666.71[c]	$y^3D^o_2$	34163
	-	7960.72[g]	$y^1D^o_2$	36601
	-	15373.64[e]	$y^3P^o_1$	42656
	-	15639.71[e]	$w^3D^o_3$	42768
	-	21343.28[e]	$w^3D^o_2$	44475
$z^5F^o_4$	3	3437.280	a^3F_4	0
(29084)	17	3461.652	a^3D_3	205
	3	3602.281	a^3F_3	1332
$z^3F^o_4$	5	3391.050	a^3F_4	0
(29481)	19	3414.765	a^3D_3	205
	5	3551.534	a^3F_3	1332

TABLE 5

Results of the branching ratio measurements for the $z^3D_2^o$ level in Ni I. The values of Corliss and Bozman (1962) are given in column 3. The absolute transition probabilities calculated from the branching ratios and the lifetimes using equation (4.3) are given in column 4. Values of $\log_{10}(gf)$ are given in column 5.

Other experimentally measured values for $\log_{10}(gf)$ listed in column 6 are from column 15 of Corliss (1965) unless otherwise noted by superscripts: (a) Garz, Heise and Richter (1970); (b) Bell, Paquette and Wiese (1966); (c) Laurent and Weniger (1970) (refer to page 34).

TABLE 5

λ(Å)	Branching Ratio (%)		Transition Probability (10^6sec^{-1})	log gf_{CIT}	log gf_{other}
	CIT	CB			
3367.892	0.30 ± 0.03	0.95	0.16 ± 0.02	-2.87 ± 0.07	-2.26
3446.263	73.8 ± 2.0	70.5	39.1 ± 4.3	-0.46 ± 0.05	-0.23,-0.42[b]
3500.852	9.4 ± 0.7	9.8	5.0 ± 0.7	-1.34 ± 0.06	-1.00,-0.92[c]
3548.185	2.1 ± 2.1	-	1.1 ± 1.1	$\leq$ -1.68	-1.19,-1.46[c]
3612.741	6.9 ± 0.5	8.0	3.6 ± 0.5	-1.45 ± 0.06	-1.04,-1.27[a] -1.33[c]
3775.572	7.5 ± 0.6	10.6	4.0 ± 0.5	-1.37 ± 0.06	-0.91
6108.121	0.11 ± 0.03	0.22	0.06 ± 0.02	-2.78 ± 0.11	-2.30
7001.57	0.0097 ± 0.002	-	0.0052 ± 0.001	-3.72 ± 0.12	-2.94
7062.97	0.014 ± 0.004	-	0.0074 ± 0.002	-3.56 ± 0.12	-2.92

TABLE 6

Branching ratios, absolute transition probabilities and $\log_{10}(gf)$'s for the transitions out of the $z^1F^o_3$ level in Ni I. The format is given in the caption to Table 5, (refer to page 35).

TABLE 6

$\lambda(\mathring{A})$	Branching Ratio (%) CIT	CB	Transition Probability ($10^6 sec^{-1}$)	$\log gf_{CIT}$	$\log gf_{other}$
3221.652	1.2 ± 0.1	1.7	0.85 ± 0.1	-2.03 ± 0.07	-1.52
3243.058	4.8 ± 0.4	6.5	3.5 ± 0.6	-1.42 ± 0.07	-1.03
3315.663	5.5 ± 0.5	7.2	4.0 ± 0.7	-1.34 ± 0.07	-0.98
3366.168	3.2 ± 0.3	3.6	2.3 ± 0.4	-1.56 ± 0.07	-1.11
3469.486	1.2 ± 0.1	2.7	0.84 ± 0.1	-1.98 ± 0.07	-1.36,-1.54[c]
3619.392	83.9 ± 0.9	78.0	60.4 ± 8.7	-0.08 ± 0.06	0.19,-0.25[a] -0.04[b]
5709.559	0.13 ± 0.03	0.37	0.096 ± 0.03	-2.48 ± 0.12	-1.81
6482.811	0.057 ± 0.02	-	0.041 ± 0.01	-2.74 ± 0.14	-2.12
11196.70	< 0.47	-	< 0.34	< -1.35	-

TABLE 7

Branching ratios, absolute transition probabilities and $\log_{10}(gf)$'s for the transitions out of the $z^3P_2^o$ level in Ni I. The format is given in the caption to Table 5. (Refer to page 35).

TABLE 7

$\lambda(\mathring{A})$	Branching Ratio (%) CIT	CB	Transition Probability ($10^6 sec^{-1}$)	log gf_{CIT}	log gf_{other}
3524.541	87.8 ± 0.7	80.9	72.0 ± 15.	-0.17 ± 0.09	0.13, -0.06[b], -0.14[c]
3610.462	10.0 ± 0.6	13.2	8.20 ± 1.8	-1.10 ± 0.10	-0.83, -1.09[a], -1.02[c]
3670.427	0.83 ± 0.07	1.8	0.68 ± 0.2	-2.16 ± 0.10	-1.76
3722.484	0.58 ± 0.05	1.4	0.48 ± 0.1	-2.31 ± 0.10	-1.80, -2.16[c]
3793.608	0.15 ± 0.01	-	0.12 ± 0.03	-2.89 ± 0.10	-2.30
3973.562	0.30 ± 0.03	1.4	0.25 ± 0.06	-2.54 ± 0.10	-1.82
6643.641	0.14 ± 0.03	0.37	0.12 ± 0.04	-2.41 ± 0.14	-1.86
7714.27	0.13 ± 0.04	0.58	0.11 ± 0.04	-2.32 ± 0.15	-1.59
7788.95	0.083 ± 0.02	0.39	0.068 ± 0.02	-2.51 ± 0.15	-1.76

TABLE 8

Branching ratios, absolute transition probabilities and $\log_{10}(gf)$'s for the transitions out of the $z^3P_1^o$ level in Ni I. The format is given in the caption to Table 5. (Refer to page 36).

TABLE 8

$\lambda(\overset{\circ}{A})$	Branching Ratio (%) CIT	CB	Transition Probability ($10^6 sec^{-1}$)	log gf_{CIT}	log gf_{other}
3492.956	83.2 ± 0.9	74.8	86.0 ± 13.3	-0.33 ± 0.07	-0.14, -0.50^a, -0.31^b, -0.45^c
3597.705	13.7 ± 0.8	18.6	14.2 ± 2.3	-1.08 ± 0.07	-0.77, -1.09^a, -1.05^c,
3664.095	1.3 ± 0.1	2.9	1.3 ± 0.2	-2.10 ± 0.08	-1.53
3831.690	1.2 ± 0.1	1.9	1.2 ± 0.2	-2.11 ± 0.08	-1.61
6256.365	0.19 ± 0.04	0.27	0.18 ± 0.05	-2.49 ± 0.12	-2.14
6767.778	0.30 ± 0.07	0.73	0.31 ± 0.08	-2.19 ± 0.12	-1.61
7197.07	0.080 ± 0.02	0.25	0.083 ± 0.03	-2.71 ± 0.13	-2.04
7261.94	0.075 ± 0.02	0.25	0.078 ± 0.02	-2.74 ± 0.13	-2.04
7414.51	0.095 ± 0.02	0.25	0.098 ± 0.03	-2.61 ± 0.13	-2.00

TABLE 9

Branching ratios, absolute transition probabilities and $\log_{10}(gf)$'s for the transitions out of the $z^3F^o_3$ level in Ni I. The format is given in the caption to Table 5. (Refer to page 36).

TABLE 9

$\lambda(\text{Å})$	Branching Ratio (%) CIT	Branching Ratio (%) CB	Transition Probability ($10^6 sec^{-1}$)	log gf_{CIT}	log gf_{other}
3409.578	0.41 ± 0.04	1.1	0.29 ± 0.06	-2.45 ± 0.09	-1.93
3433.558	21.0 ± 1.1	21.6	14.8 ± 2.7	-0.74 ± 0.08	-0.50, -0.66[a], -0.58[c]
3515.054	61.4 ± 1.4	54.1	43.3 ± 7.7	-0.25 ± 0.08	-0.09, -0.25[b], -0.75[c]
3571.869	6.7 ± 0.4	8.3	4.7 ± 0.9	-1.20 ± 0.08	-0.82
3688.415	0.51 ± 0.04	1.6	0.36 ± 0.07	-2.29 ± 0.09	-1.76
3858.301	9.9 ± 0.6	13.2	6.9 ± 1.3	-0.96 ± 0.08	-0.56
6327.603	0.022 ± 0.005	-	0.015 ± 0.004	-3.19 ± 0.12	-2.80
7291.48	0.037 ± 0.009	0.13	0.026 ± 0.008	-2.84 ± 0.14	-2.42
13849.49	-	-	-	-	-

TABLE 10

Branching ratios, absolute transition probabilities and $\log_{10}(gf)$'s for the transitions out of the $z^3F_2^o$ level in Ni I. The format is given in the caption to Table 5. (Refer to page 36).

TABLE 10

λ(Å)	Branching Ratio (%) CIT	CB	Transition Probability ($10^6 sec^{-1}$)	log gf_{CIT}	log gf_{other}
3286.946	0.42 ± 0.04	-	0.26 ± 0.04	-2.69 ± 0.07	-2.07,-1.31[c]
3361.556	6.1 ± 0.5	5.0	3.7 ± 0.5	-1.50 ± 0.06	-1.14
3413.478	6.4 ± 0.5	5.2	3.9 ± 0.6	-1.46 ± 0.06	-1.17
3458.474	77.7 ± 1.1	79.3	47.6 ± 5.9	-0.37 ± 0.05	-0.05,-0.46[a], -0.28[b],-0.94[c],
3519.766	5.7 ± 0.4	10.5	3.5 ± 0.5	-1.49 ± 0.06	-0.96
3674.150	3.7 ± 0.3	-	2.3 ± 0.3	-1.64 ± 0.06	-
5847.010	0.018 ± 0.004	-	0.011 ± 0.003	-3.55 ± 0.11	-2.97
6716.14	< 0.013	-	< 0.0082	< -3.56	-3.90

TABLE 11

Branching ratios, absolute transition probabilities and $\log_{10}(gf)$'s for the transitions out of the $z^1D_2^o$ level in Ni I. The format is given in the caption to Table 5. (Refer to page 37).

TABLE 11

$\lambda(\AA)$	Branching Ratio (%) CIT	CB	Transition Probability ($10^6 sec^{-1}$)	log gf_{CIT}	log gf_{other}
3200.423	0.15 ± 0.01	-	0.073 ± 0.01	-3.25 ± 0.06	-2.46
3271.118	0.84 ± 0.08	1.6	0.42 ± 0.06	-2.47 ± 0.06	-1.80
3320.257	6.7 ± 0.5	5.6	3.3 ± 0.4	-1.56 ± 0.06	-1.09,-1.07[c]
3362.806	0.18 ± 0.02	-	0.088 ± 0.01	-3.13 ± 0.06	-2.42
3420.741	0.18 ± 0.02	-	0.088 ± 0.01	-3.11 ± 0.06	-2.68
3566.372	91.0 ± 0.6	92.3	45.3 ± 4.5	-0.36 ± 0.04	0.03
5578.734	0.090 ± 0.02	0.16	0.045 ± 0.01	-2.98 ± 0.11	-2.26
6314.666	0.91 ± 0.2	0.29	0.45 ± 0.1	-1.87 ± 0.10	-1.87
6364.597	0.0055 ± 0.001	-	0.0028 ± 0.0007	-4.08 ± 0.12	-3.54

TABLE 12

Branching ratios, absolute transition probabilities and $\log_{10}(gf)$'s for the transitions out of the e^3G_5 level in Ni I. The format is given in the caption to Table 5. (Refer to page 37).

TABLE 12

λ(Å)	Branching Ratio (%) CIT	CB	Transition Probability ($10^6 sec^{-1}$)	log gf_{CIT}	log gf_{other}
4565.45	< 0.012	-	< 0.0065	< -3.65	-
4633.031	0.14 ± 0.04	-	0.077 ± 0.02	-2.56 ± 0.13	-
4740.165	0.59 ± 0.07	-	0.34 ± 0.06	-1.91 ± 0.07	-1.09
4849.12	< 0.012	-	< 0.0065	< -3.60	-
4980.161	33.8 ± 3.0	27.5	19.2 ± 2.8	-0.11 ± 0.06	0.56,0.03[a]
5080.523	55.9 ± 3.2	64.8	31.7 ± 4.0	0.13 ± 0.06	0.91
5499.39	0.11 ± 0.02	-	0.062 ± 0.02	-2.51 ± 0.11	-1.55
6176.813	8.2 ± 1.1	7.7	4.7 ± 0.8	-0.53 ± 0.08	0.18
6421.507	1.3 ± 0.2	-	0.73 ± 0.1	-1.31 ± 0.09	-0.40
16945.47	-	-	-	-	-

TABLE 13

Branching ratios, absolute transition probabilities and $\log_{10}(gf)$'s for the transitions out of the e^5F_5 level in Ni I. The format is given in the caption to Table 5. (Refer to page 38).

TABLE 13

$\lambda(\text{Å})$	Branching Ratio (%)		Transition Probability ($10^6 sec^{-1}$)	log gf_{CIT}	log gf_{other}
	CIT	CB			
4401.547	30.6 ± 1.8	37.5	37.5 ± 7.2	0.08 ± 0.09	0.86
4714.421	37.3 ± 1.9	34.2	45.8 ± 8.8	0.22 ± 0.08	0.90,0.31[a]
4786.541	14.6 ± 1.0	13.8	17.9 ± 3.5	-0.17 ± 0.09	0.50
4900.97	0.41 ± 0.05	-	0.50 ± 0.1	-1.70 ± 0.10	-1.04
5017.591	16.3 ± 1.2	14.5	20.0 ± 4.0	-0.08 ± 0.09	0.59
5157.993	0.48 ± 0.06	-	0.59 ± 0.1	-1.59 ± 0.10	-0.81
5265.748	0.30 ± 0.05	-	0.37 ± 0.09	-1.77 ± 0.11	-1.13
6452.770	< 0.03	-	< 0.037	< -2.60	-

TABLE 14

Branching ratios, absolute transition probabilities and $\log_{10}(gf)$'s for the transitions out of the g^3F_3 level in Ni I. The format is given in the caption to Table 5. (Refer to page 38).

TABLE 14

$\lambda(\mathring{A})$	Branching Ratio (%) CIT	CB	Transition Probability ($10^6 sec^{-1}$)	log gf_{CIT}	log gf_{other}
4009.984	0.93 ± 0.1	-	0.85 ± 0.2	-1.84 ± 0.10	-
4035.96	0.53 ± 0.08	-	0.48 ± 0.1	-2.08 ± 0.11	-
4230.39	< 0.45	-	< 0.41	< -2.12	-
4295.888	18.5 ± 0.9	-	16.9 ± 3.2	-0.49 ± 0.08	0.01
4382.87	1.6 ± 0.2	-	1.5 ± 0.3	-1.53 ± 0.09	-0.96
4450.13	0.89 ± 0.4	-	0.81 ± 0.4	-1.77 ± 0.20	-1.28
4698.408	6.8 ± 0.5	-	6.2 ± 1.2	-0.84 ± 0.09	-0.17
4729.291	3.0 ± 0.2	-	2.7 ± 0.5	-1.20 ± 0.09	-
4817.847	7.7 ± 0.6	-	7.0 ± 1.4	-0.77 ± 0.09	-0.38
4838.651	23.7 ± 1.3	-	21.7 ± 4.2	-0.27 ± 0.08	0.26
4843.53	4.8 ± 0.4	-	4.4 ± 0.9	-0.97 ± 0.09	-0.53
4976.71	1.7 ± 0.2	-	1.6 ± 0.3	-1.39 ± 0.09	-1.00
5371.33	17.7 ± 1.4	-	16.2 ± 3.3	-0.31 ± 0.09	-0.02
5664.017	12.3 ± 1.3	100.	11.3 ± 2.4	-0.42 ± 0.09	-0.01

TABLE 14 - (Continued)

λ(Å)	Branching Ratio (%)		Transition Probability ($10^6 sec^{-1}$)	log gf_{CIT}	log gf_{other}
	CIT	CB			
9689.35	< 1.2	-	< 1.1	< -0.97	-
10061.29	< 2.1	-	< 1.9	< -0.70	-
10226.14	< 2.2	-	< 2.0	< -0.66	-
10321.10	< 2.6	-	< 2.4	< -0.58	-

TABLE 15

Branching ratios, absolute transition probabilities and $\log_{10}(gf)$'s for the transitions out of the e^3P_2 level in Ni I. The format is given in the caption to Table 5. (Refer to page 34).

TABLE 15

$\lambda(\mathring{A})$	Branching Ratio (%)		Transition Probability ($10^6 sec^{-1}$)	log gf_{CIT}	log gf_{other}
	CIT	CB			
4444.55	< 0.063	-	< 0.050	< -3.13	-2.56
4597.65	< 0.089	-	< 0.072	< -2.94	-2.01
4855.414	70.1 ± 1.3	72.8	56.6 ± 9.2	0.00 ± 0.07	0.55,-0.01[a]
5039.359	4.6 ± 0.4	-	3.7 ± 0.7	-1.15 ± 0.08	-0.54
5085.479	2.1 ± 0.2	-	1.7 ± 0.3	-1.49 ± 0.09	-0.58
5129.383	15.4 ± 0.9	27.2	12.4 ± 2.1	-0.61 ± 0.08	0.06
5187.86	0.75 ± 0.1	-	0.61 ± 0.1	-1.91 ± 0.10	-1.24
5262.83	0.071± 0.02	-	0.057 ± 0.02	-2.92 ± 0.12	-2.04
5514.80	0.56 ± 0.08	-	0.45 ± 0.1	-1.98 ± 0.09	-1.21
5642.660	0.50 ± 0.7	-	0.40 ± 0.09	-2.02 ± 0.09	-1.08
6180.093	0.47 ± 0.08	-	0.38 ± 0.09	-1.97 ± 0.10	-1.29
6230.115	2.4 ± 0.4	-	1.9 ± 0.4	-1.25 ± 0.10	-0.74
6384.697	3.0 ± 0.5	-	2.4 ± 0.5	-1.13 ± 0.10	-0.38
6666.71	< 1.8	-	< 1.5	< -1.32	-1.76
7960.72	< 0.19	-	< 0.15	< -2.14	-

TABLE 15 - (Continued)

$\lambda(\mathring{A})$	Branching Ratio (%)		Transition Probability ($10^6 sec^{-1}$)	log gf_{CIT}	log gf_{other}
	CIT	CB			
15373.64	-	-	-	-	-
15639.71	-	-	-	-	-
21343.28	-	-	-	-	-

TABLE 16

Branching ratios, absolute transition probabilities and $\log_{10}(gf)$'s for the transitions out of the $z^5F^o_4$ level in Ni I. The absolute transition probabilities were obtained from our branching ratio measurements and using Marek's (1972) value of 33.4 ± 4.0 nsec for the lifetime. The format is given in the caption to Table 5. (Refer to page 40).

TABLE 16

λ(Å)	Branching Ratio (%) CIT	CB	Transition Probability ($10^6 sec^{-1}$)	log gf_{CIT}	log gf_{other}
3437.280	12.2 ± 0.8	16.2	3.65 ± 0.5	-1.23 ± 0.06	-0.89,-1.04[a], -0.73[c]
3461.652	86.5 ± 0.8	83.8	25.9 ± 3.1	-0.38 ± 0.05	-0.22,-0.48[a]
3602.281	1.3 ± 0.1	-	0.39 ± 0.06	-2.16 ± 0.07	-1.70,-1.58[c]

TABLE 17

Branching ratios, absolute transition probabilities and $\log_{10}(gf)$'s for the transitions out of the $z^3F_4^o$ level in Ni I. The absolute transition probabilities were obtained from our branching ratio measurements and using Marek's (1972) value of 16.85 ± 0.8 nsec for the lifetime. The format is given in the caption to Table 5. (Refer to page 40).

TABLE 17

λ(Å)	Branching Ratio (%) CIT	CB	Transition Probability ($10^6 sec^{-1}$)	log gf_{CIT}	log gf_{other}
3391.050	8.7 ± 0.7	13.7	5.1 ± 0.5	-1.10 ± 0.04	-0.84,-0.94[a], -1.10[b]
3414.765	91.1 ± 0.7	85.7	54.1 ± 2.7	-0.07 ± 0.02	0.02,-0.08[b]
3551.534	0.24 ± 0.03	0.6	0.14 ± 0.02	-2.62 ± 0.05	-2.10

TABLE 18

Observed and predicted locations of the Ni I transition $a^3P_2 - z^3P^o_2$ (RMT No. 62). (Refer to page 35).

TABLE 18

Source	Wavelength (Å) [in air]
Moore (1945)	7714.27
Kitt Peak Preliminary Solar Atlas (Testerman 1973)	7714.307
Moore *et al*. (1966)	7714.310
Pierce and Breckenridge (1973)	7714.3205
Swensson *et al*. (1970)	7714.32
Babcock and Moore (1947)	7714.310
Predicted wavelength: This thesis (See Section 2)	7714.317

TABLE 19

Comparison of branching ratios for some strong Ni I lines measured in this work (see Tables 5-17) with values given by Marek (1972).

TABLE 19

Wavelength (Å)	RMT No.	Branching Ratio (CIT)	Branching Ratio (Marek)
3414.765	(19)	91.1%	87.3%
3461.652	(17)	86.5	81.8
3492.956	(18)	83.2	75.3
3515.054	(19)	61.4	53.0
3524.541	(18)	87.8	85.7

TABLE 20

Comparison of CIT results with those of Bell *et al*. (1966), denoted BPW, for the 7 lines measured by both groups. (Refer to page 49).

TABLE 20

Wavelength (Å)	RMT No.	log gf_{BPW}	log gf_{CIT}
3391.050	(5)	-1.10	-1.10
3446.263	(20)	-0.42	-0.46
3458.474	(19)	-0.28	-0.37
3492.956	(18)	-0.31	-0.33
3515.054	(19)	-0.25	-0.25
3524.541	(18)	-0.06	-0.17
3619.392	(35)	-0.04	-0.08

TABLE 21

Values of W and log(gf Γ) for the solid data points plotted in Figure 18. The values of log Γ are from Cayrel and Jugaku (1963). The transitions are listed in order of increasing wavelength. The wavelengths at the end of the table are those transitions not used in the fits to Hunger's (1956) theoretical curves of growth shown in Figure 18. Values of W in column 5 are from Moore (1966) unless otherwise noted by superscripts: (a) Lennard (Michigan Atlas, unpublished); (b) Holweger (1967); (c) Swensson _et al_. (1970); (d) Grevesse (1969).

TABLE 21

Wavelength (Å)	RMT No.	log(gf Γ)	W^{KP} (mÅ)	W^{other} (mÅ)
3221.652	(8)	3.44		104
3243.058	(22)	4.03		127
3315.663	(22)	4.03		153
3320.257	(9)	3.75		122
3361.556	(19)	3.87		156
3362.806	(23)	2.14		93
3366.168	(8)	3.75		116
3367.892	(20)	2.58	84.4	39,79[a]
3391.050	(5)	4.38		238
3409.578	(5)	3.03		100
3413.478	(5)	3.85		186
3420.741	(9)	2.10		78
3437.280	(3)	4.25		184
3500.852	(6)	3.98		163
3519.766	(5)	3.73		174
3551.534	(5)	2.71		94
3571.869	(5)	4.13		249
3597.705	(18)	4.20		181
3602.281	(3)	3.16		94
3610.462	(18)	4.29		188
3612.741	(6)	3.77		163
3664.095	(4)	3.12		160
3670.427	(4)	3.17		149
3674.150	(32)	3.43		121
3688.415	(5)	2.93		109
3775.572	(33)	3.71		178
3858.301	(32)	4.12		255

TABLE 21 - Continued

Wavelength (Å)	RMT No.	log(gf Γ)	W^{KP}(mÅ)	W^{other}(mÅ)
4009.984	(150)	0.18	14.5	18
4035.96	(150)	-0.08	4.49	
4295.888	(178)	1.35	50.1	42
4382.87	-	0.26	18.6	
4401.547	(86)	2.52	99.6	115
4450.13	(178)	-0.03	3.84	4.9
4633.031	-	-0.30	3.17	
4698.408	(235)	0.77	26.1	26
4714.421	(98)	2.49	171	118
4729.291	(235)	0.40		16
4740.165	(99)	0.27	15.9	14
4786.541	(98)	2.06	99.1	110
4817.847	(254)	0.78	54.0	62
4838.651	(260)	1.27	50.3	45
4843.53	(235)	0.57	23.6	20
4855.414	(130)	2.12		75
4900.97	(98)	0.47	20.8	17
4976.71	(254)	0.09	6.97	6
4980.161	(112)	1.95	104	100
5017.591	(111)	2.04	101	90
5039.36	(142)	0.88		31
5080.523	(143)	2.14	121	93
5085.479	(130)	0.52		18
5129.383	(159)	1.38		62
5157.993	(111)	0.47	18.7	18,17[b]
5187.86	(159)	0.05		8
5371.33	-	0.99	28.7	62
5499.39	(176)	-0.68	3.09	2.7
5514.80	(189)	-0.16	7.46	7.7
5578.734	(47)	0.91	58.2	52,52[b]

TABLE 21 - Continued

Wavelength (Å)	RMT No.	log(gf Γ)	W^{KP}(mÅ)	W^{other}(mÅ)
5642.660	(203)	-0.24	5.75	4.5
5664.017	(272)	0.76	41.8	35
5709.559	(46)	1.40	78.6	90
5847.010	(44)	0.33	20.3	20,20[b]
6108.121	(45)	1.10	65.6	63,61[b],70.6[d]
6176.813	(228)	1.05	67.5	54,65[b]
6180.093	(217)	-0.39	4.57	3
6230.115	(227)	0.31	20.1	17,20[b]
6256.365	(43)	1.39	96.0	81
6314.666	(67)	1.75	77.8	68
6327.603	(44)	0.68	37.3	36,36[b]
6364.597	(67)	-0.47	3.50	
6384.697	(246)	0.38		20
6421.507	(258)	0.19	18.2	16
6482.811	(66)	0.87	40.9	38,38[b]
6643.641	(43)	1.45	96.0	90,91[b]
6767.778	(57)	1.53	81.6	82,77[b]
7001.57	(64)	-0.12	11.0	11,11[b]
7062.97	(64)	0.02	14.4	13
7197.07	(62)	0.88	70.3	70
7261.94	(62)	0.84	65.9	70
7291.48	(63)	0.75	49.6	47
7414.51	(62)	0.92	69.1	71
7714.27	(62)	1.24	107	105,109[c]
7788.95	(62)	1.04	94.6	84,97[c]
3414.765	(19)	5.38		809
3433.558	(19)	4.72		490
3446.263	(20)	4.92		470
3458.474	(19)	4.90		656
3461.652	(17)	5.08		758

TABLE 21 - Continued

Wavelength (Å)	RMT No.	log(gf Γ)	W^{KP}(mÅ)	W^{other}(mÅ)
3492.956	(18)	5.05		835
3515.054	(19)	5.13		710
3524.541	(18)	5.29		1271
3566.372	(36)	4.71		503
3619.392	(35)	4.99		739

TABLE 22

Values for the solar Ni abundance, $A_{Ni} = \log_{10}(N_{Ni}/N_H) + 12.00$, derived by L. Testerman (KPNO) using HSRA temperature model. Values of W are from the Kitt Peak Preliminary Solar Atlas and also appear in Table 21. Values of log gf are from this work. (Refer to pages 66 and 67).

TABLE 22

Wavelength (Å)	RMT No.	W^{KP}(mÅ)	A_{Ni}
4740.165	(99)	15.9	6.44
5157.993	(111)	18.7	6.23
5499.39	(176)	3.09	6.58
5709.559	(46)	78.6	6.12
5847.010	(44)	20.3	6.33
6108.121	(45)	65.6	6.23
6176.813	(228)	67.5	6.34
6256.365	(43)	96.0	6.24
6327.603	(44)	37.3	6.27
6364.597	(67)	3.50	6.33
6421.507	(258)	18.2	6.41
6482.811	(66)	40.9	6.11
6643.641	(43)	96.0	6.13
6767.778	(57)	81.6	5.90
7001.57	(64)	11.0	6.39
7062.97	(64)	14.4	6.37
7261.94	(62)	65.9	6.36
7291.48	(63)	49.6	6.28
7414.51	(62)	69.1	6.32
7788.95	(62)	94.6	6.34

TABLE 23

Values for the solar Ni abundance, $A_{Ni} = \log_{10}(N_{Ni}/N_H) + 12.00$, derived using published data from Holweger (1967). The W values are taken from the Michigan Atlas (unpublished). The values in columns 3 and 4 are taken directly from Holweger. Values of log gf are from this work (See Tables 5-17).

TABLE 23

Wavelength (Å)	RMT No.	W^{Mich} (mÅ)	A_{Ni}+ log(gf)	log(gf_{CIT})	A_{Ni} (Holweger)
5157.993	(111)	17	4.6	-1.59	6.19
5578.734	(47)	52	3.4	-2.98	6.38
5847.010	(44)	20	2.8	-3.55	6.35
6108.121	(45)	61	3.5	-2.78	6.29
6176.813	(228)	65	5.8	-0.53	6.33
6230.115	(227)	20	5.1	-1.25	6.35
6327.603	(44)	36	3.1	-3.19	6.29
6482.811	(66)	38	3.4	-2.74	6.14
6643.641	(43)	91	3.9	-2.41	6.31
6767.778	(57)	77	3.9	-2.19	6.09
7001.57	(64)	11	2.7	-3.72	6.42

TABLE 24

Summary of the results obtained for the Ni abundance, A_{Ni}, in this work and comparison with the result of Garz (1971). Column 1 gives the source of the equivalent widths (W), colume 2 gives the source of the gf values used, and column 3 gives the number of lines used in the analysis. The result given in the last row was obtained by correcting the value of Grevesse (1969) using gf_{CIT} . The value of W marked with an asterisk was measured by Grevesse from the recent solar spectrum recorded by Delbouille *et al*. (1973). The uncertainties shown in column 6 are discussed in the text. (Refer to page 68).

TABLE 24

W	gf	No. of Lines	Solar Model	Method	A_{Ni}
W^{KP}	gf_{CIT}	20	HSRA (Gingerich _et_ _al_. 1971)	Fine analysis	6.29 ± 0.14
W^{Mich}	gf_{CIT}	11	Holweger (1967)	Fine analysis	6.29 ± 0.09
W^{KP}	gf_{CIT}	82	Cayrel and Jugaku (1963)	Curve of growth	6.26 ± 0.13
W^{Mich}	gf_{GHR}	21	Holweger (1967)	Fine analysis	6.25 ± 0.13
W^{*}	gf_{CIT}	1	Elste (1968)	Fine analysis	6.29

TABLE 25

Results of method described in Appendix F to determine the ratio of lifetimes for the $z^3P_1^o$ and $z^3P_2^o$ levels using the observed intensities of all the branches out of each upper level. The subscript on the quantity τ is the value of the quantum number J of the upper level. The superscript "M" refers to the values of Marek (1972).

TABLE 25

Upper Level Designation	Lifetime Ratios from Lifetime Measurements (see Table 3)	Lifetime Ratios from Appendix F
$z^3F^o_{2,3,4}$	$\tau_2^{CIT}/\tau_3^{CIT}$ = 1.15 ± 0.24	τ_2/τ_3 = 1.32 ± 0.11
	τ_3^M/τ_4^M = 0.73 ± 0.02	τ_3/τ_4 = 0.73 ± 0.01
$z^3P^o_{1,2}$	$\tau_1^{CIT}/\tau_2^{CIT}$ = 0.80 ± 0.20	τ_1/τ_2 = 0.91 ± 0.06
	$\tau_1^M\ \tau_2^M$ = 0.98 ± 0.03	

TABLE 26

Possible unclassified transitions in Ni I. The predicted wavelengths, obtained by the method described in Section 2 (equation (2.7)), represent wavelengths in air. Solar wavelengths and intensities are from the Kitt Peak Preliminary Solar Atlas. Values of W^{KP} in parentheses are uncertain. Where no values are given, there is no evidence for the presence of the predicted line in the solar spectrum. (Refer to page 105).

TABLE 26

Predicted Wavelength (Å)	Transition (lower - upper)	Transition Probability (sec^{-1})	Observed Solar Wavelength (Å)	W^{KP}(mÅ)
4271.402	$z^5D^o_4$ - e^3G_5	$< 5.6 \times 10^5$	-	-
4633.031	$z^5G^o_5$ - e^3G_5	7.71×10^4	4633.037	3.17
4712.217	$z^5D^o_1$ - e^3P_2	$< 9.9 \times 10^4$	-	-
5327.022	$z^5F^o_1$ - e^3P_2	$< 1.7 \times 10^4$	-	-
5392.359	$z^3F^o_2$ - e^3P_2	$< 2.2 \times 10^4$	-	-
5479.068	$z^3D^o_1$ - e^3P_2	$< 5.0 \times 10^4$	-	-
5482.210	$z^3G^o_5$ - e^3G_5	$< 5.3 \times 10^4$	5482.205	(0.52)
5698.453	$z^3G^o_5$ - e^5F_5	$< 1.4 \times 10^4$	-	-
5717.036	$z^3G^o_4$ - e^5F_5	$< 1.4 \times 10^4$	-	-
6660.577	a^3P_2 - $z^3F^o_2$	$< 4.3 \times 10^3$	6660.593	(0.67)
6720.218	$z^1G^o_4$ - e^5F_5	$< 5.2 \times 10^4$	-	-
6777.571	$y^3D^o_1$ - e^3P_2	$< 1.0 \times 10^5$	-	-
7960.703	$y^1D^o_2$ - e^3P_2	$< 1.5 \times 10^5$	-	-

FIGURE 1

Schematic diagram of the lifetime measurement apparatus.

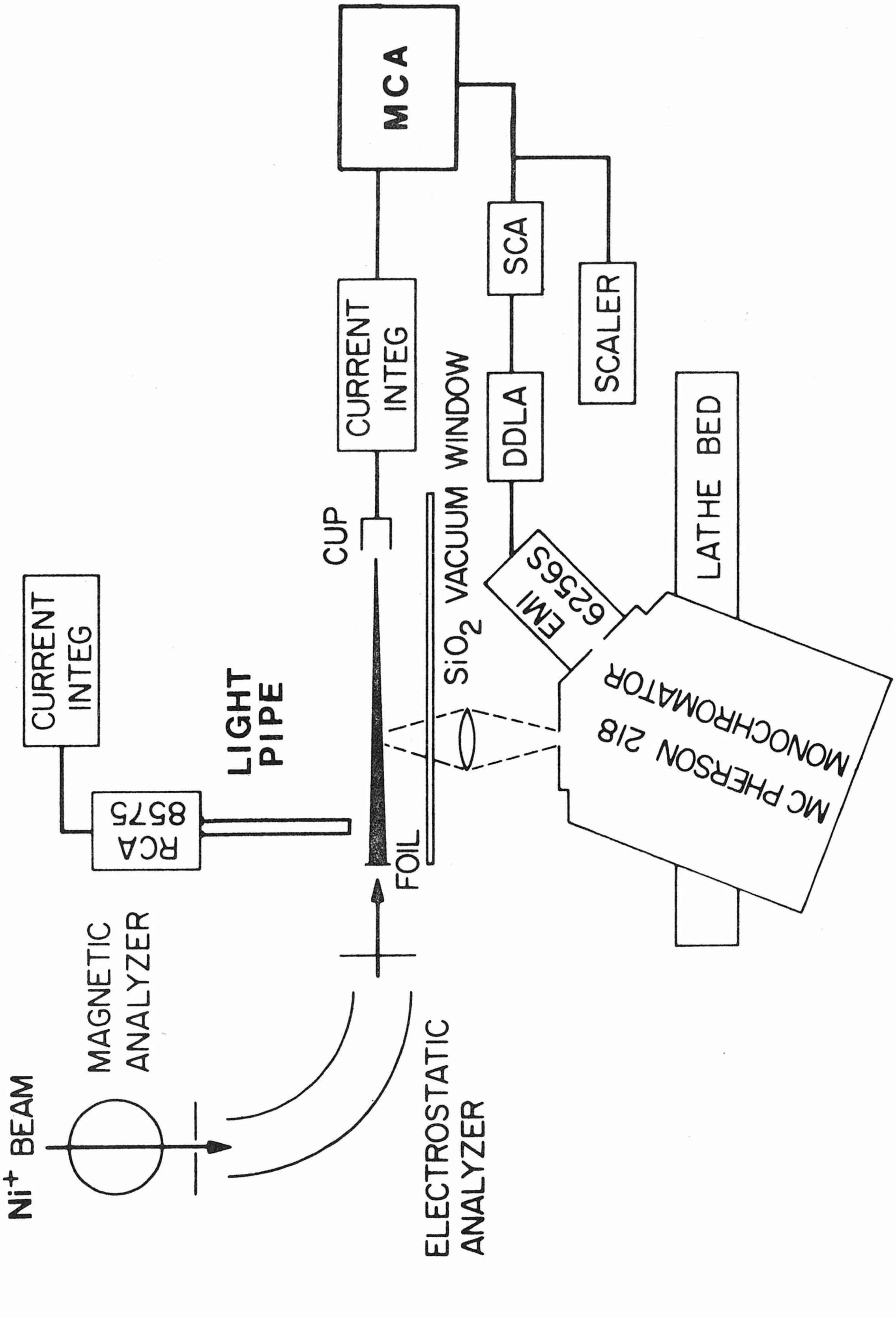
Ni⁺ BEAM
MAGNETIC ANALYZER
ELECTROSTATIC ANALYZER
FOIL
RCA 8575
CURRENT INTEG
LIGHT PIPE
CUP
CURRENT INTEG
MCA
SiO₂ VACUUM WINDOW
DDLA
SCA
SCALER
EMI 6256S
MC PHERSON 218 MONOCHROMATOR
LATHE BED

FIGURE 2

a) Schematic diagram of apparatus used to measure the Doppler shift of the Ni I λ3619 line emitted by the moving beam particles. The angle θ between the beam direction and the direction of observation is shown.

b) Typical Doppler shift of λ3619. The 0^o profile was observed using the apparatus shown in (a). The 90^o profile was observed using the apparatus shown in Figure 1. The distance between the line centers is $\Delta\lambda = \beta\lambda_o$, where $\lambda_o = 3619Å$.

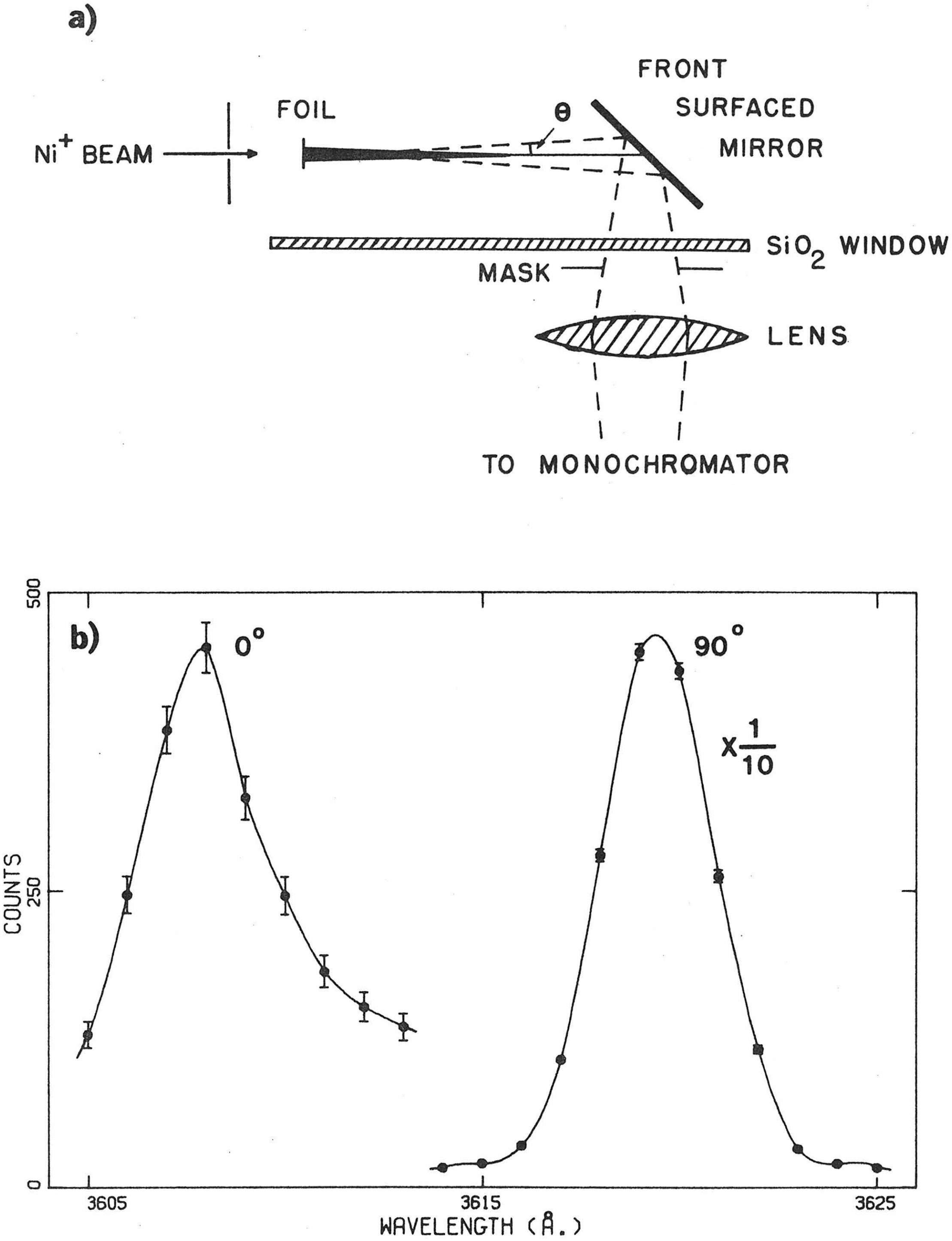
a)
FRONT
SURFACED
MIRROR
FOIL
θ
Ni$^+$ BEAM
SiO$_2$ WINDOW
MASK
LENS
TO MONOCHROMATOR
b)
0°
90°
x $\frac{1}{10}$
COUNTS
500
250
0
3605
3615
3625
WAVELENGTH (Å.)

FIGURE 3

Light decay curve for λ3492.956 (a^3D_2 - $z^3P^o_1$, RMT No. 18) at 410 keV incident beam energy, approximately 350 keV beam energy emerging from a 10 μgm/cm^2 carbon foil. Angle of observation is 90° and the pass band of the monochromator is 2.7Å fwhm. The 1 cm entrance slit is normal to the beam velocity. The sources of background have been subtracted from the data. Statistical errors are shown. The dashed lines show the computer-generated, two-exponential fit. The lifetime obtained from the fit was 9.7 ± 0.8 nsec and R(0) = 0.15 . (Refer to page 17).

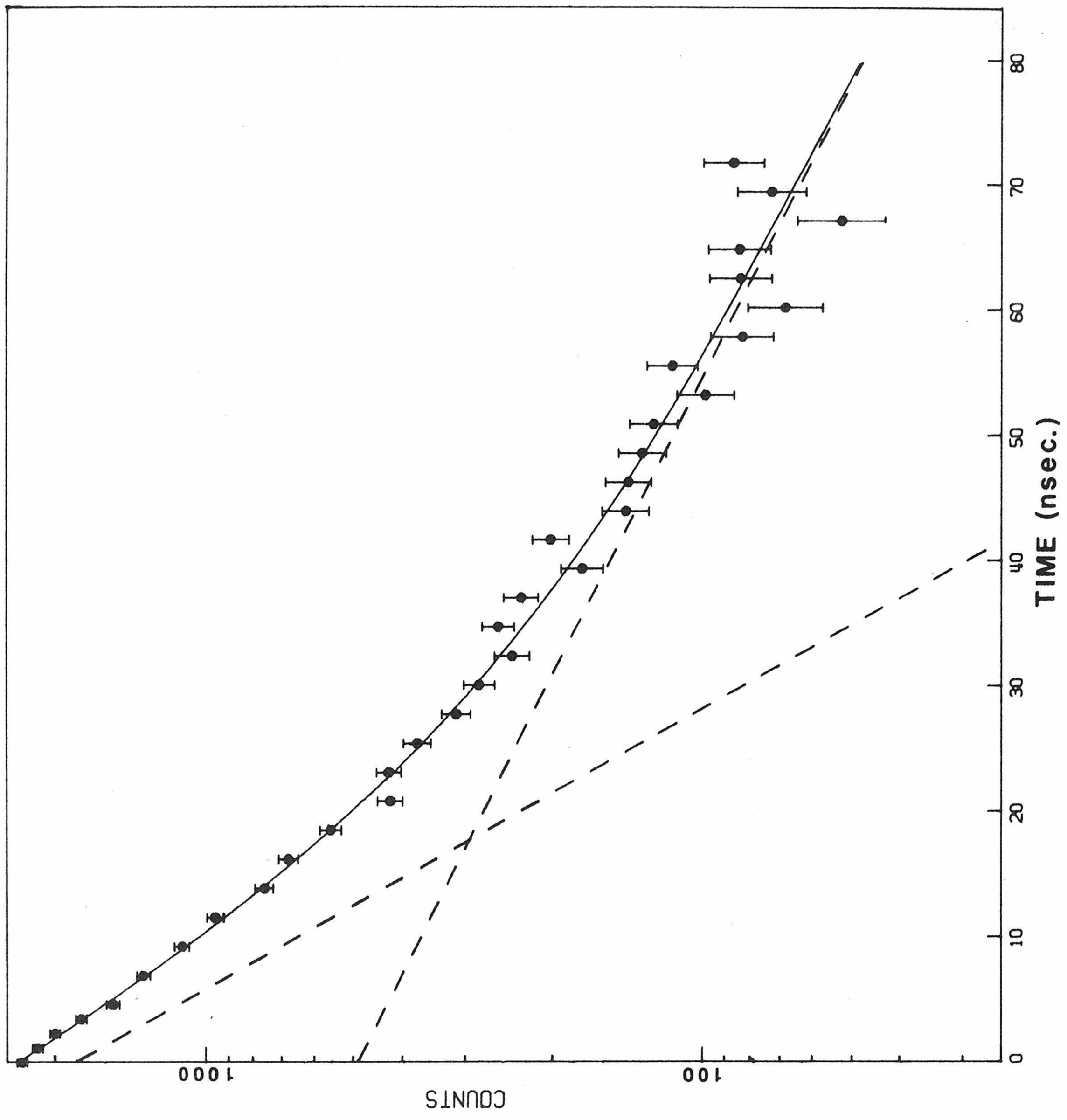
COUNTS
1000
100
TIME (nsec.)
0
10
20
30
40
50
60
70
80

FIGURE 4

Light decay curve for λ3524.541 (a^3D_3 - $z^3P^o_2$, RMT No. 18) at 305 keV incident beam energy, approximately 250 keV beam energy emerging from a 10 μgm/cm^2 carbon foil. The observing conditions are the same as in Figure 3. The dashed lines show the computer-generated, two-exponential fit. The lifetime obtained from the fit was 12.5 ± 1.0 nsec. The value of R(0) was 0.06.

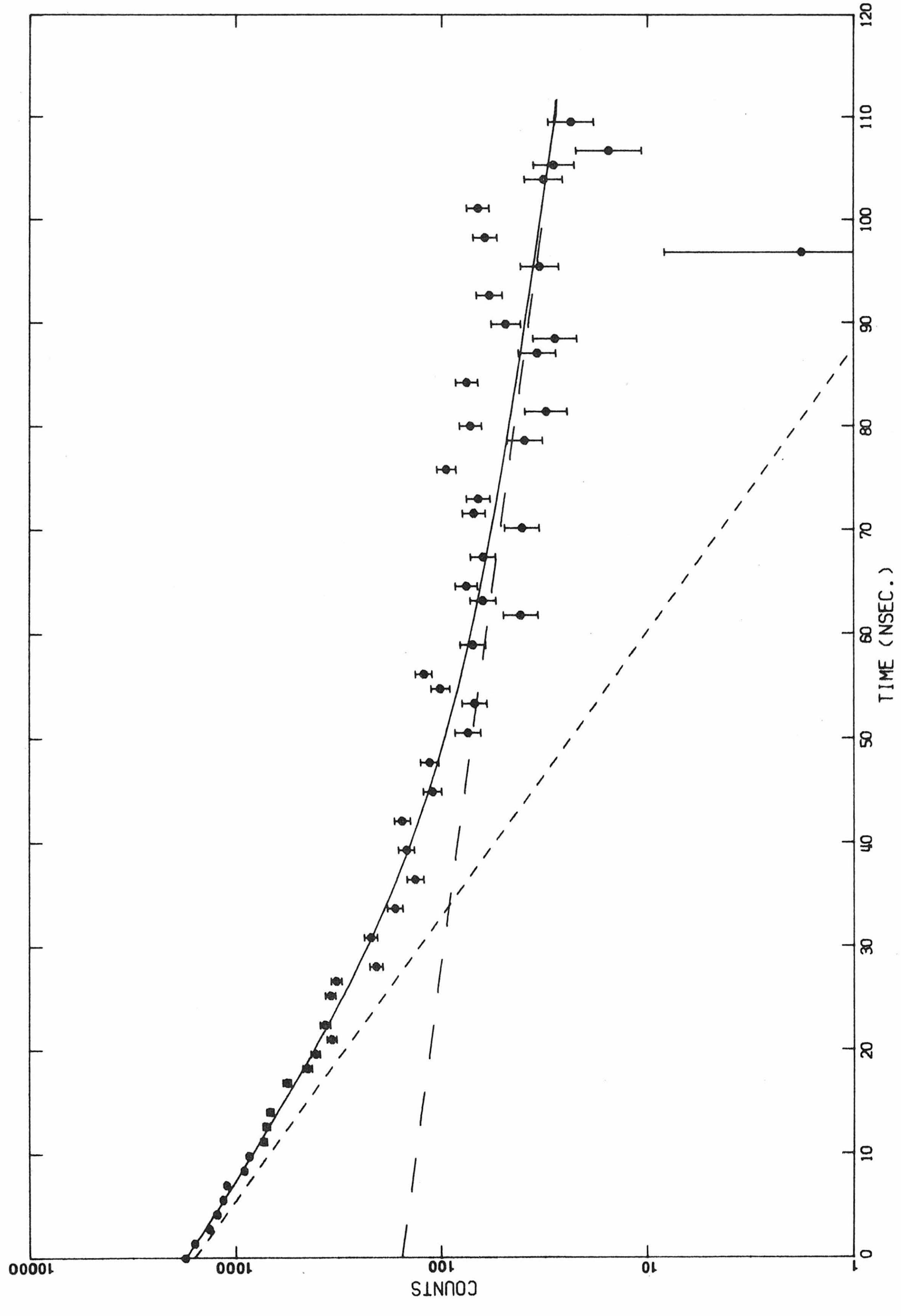
COUNTS
10000
1000
100
10
1
TIME (NSEC.)
0
10
20
30
40
50
60
70
80
90
100
110
120

FIGURE 5

Partial Grotian diagram for Ni I, showing the decay modes for level e^3G_5 . The wavelengths of the various branches can be found in Table 4. The designation of the levels is from Moore (1971). The vertical height of the levels represents the excitation energy above the ground state in kilokaysers (1 kK = 1000 cm^{-1}). The branching ratios for the decay channels are taken from Table 12.

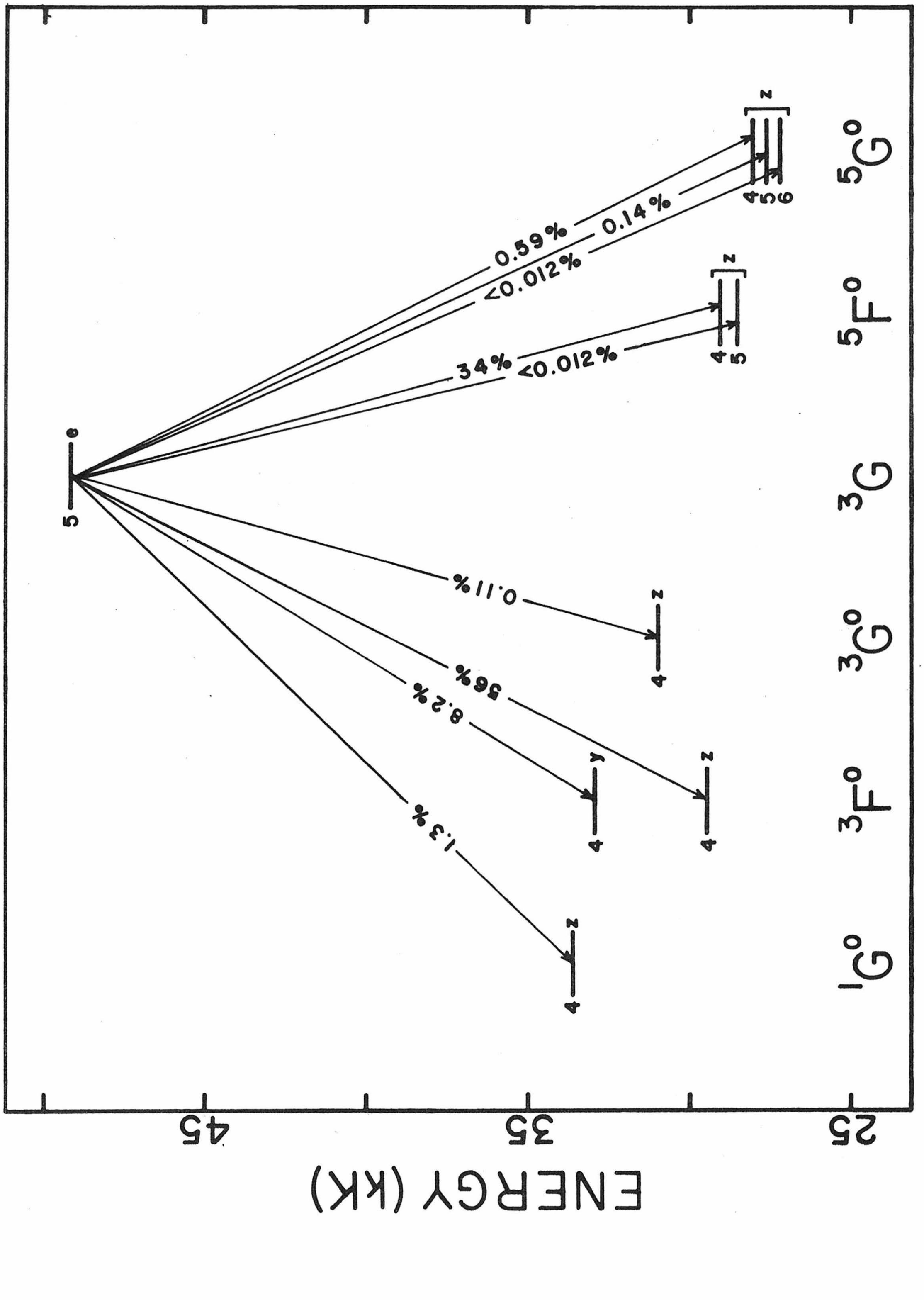
ENERGY (kK)
25
35
45
$^1G^o$
$^3F^o$
$^3G^o$
^3G
$^5F^o$
$^5G^o$
5 e
1.3%
8.2%
56%
0.11%
34%
<0.012%
<0.012%
0.14%
0.59%
4 z
4 y
4 z
4 z
4 5 z
4 5 6 z

FIGURE 6

Schematic diagram of the two-channel Paschen-Runge spectrometer and hollow cathode source used for the branching ratio measurements in the wavelength region λλ3200-8000. Both the monitor and the scanning channel detectors move along the circular track. The monitor channel is shown in its position to detect the spectrum diffracted to the right of the grating normal while the scanning channel detects the left spectrum which is enhanced by the grating blaze. The detector system relative efficiency is measured by rotating the concave mirror to image the tungsten-strip filament of the standard lamp onto the entrance slit of the spectrometer.

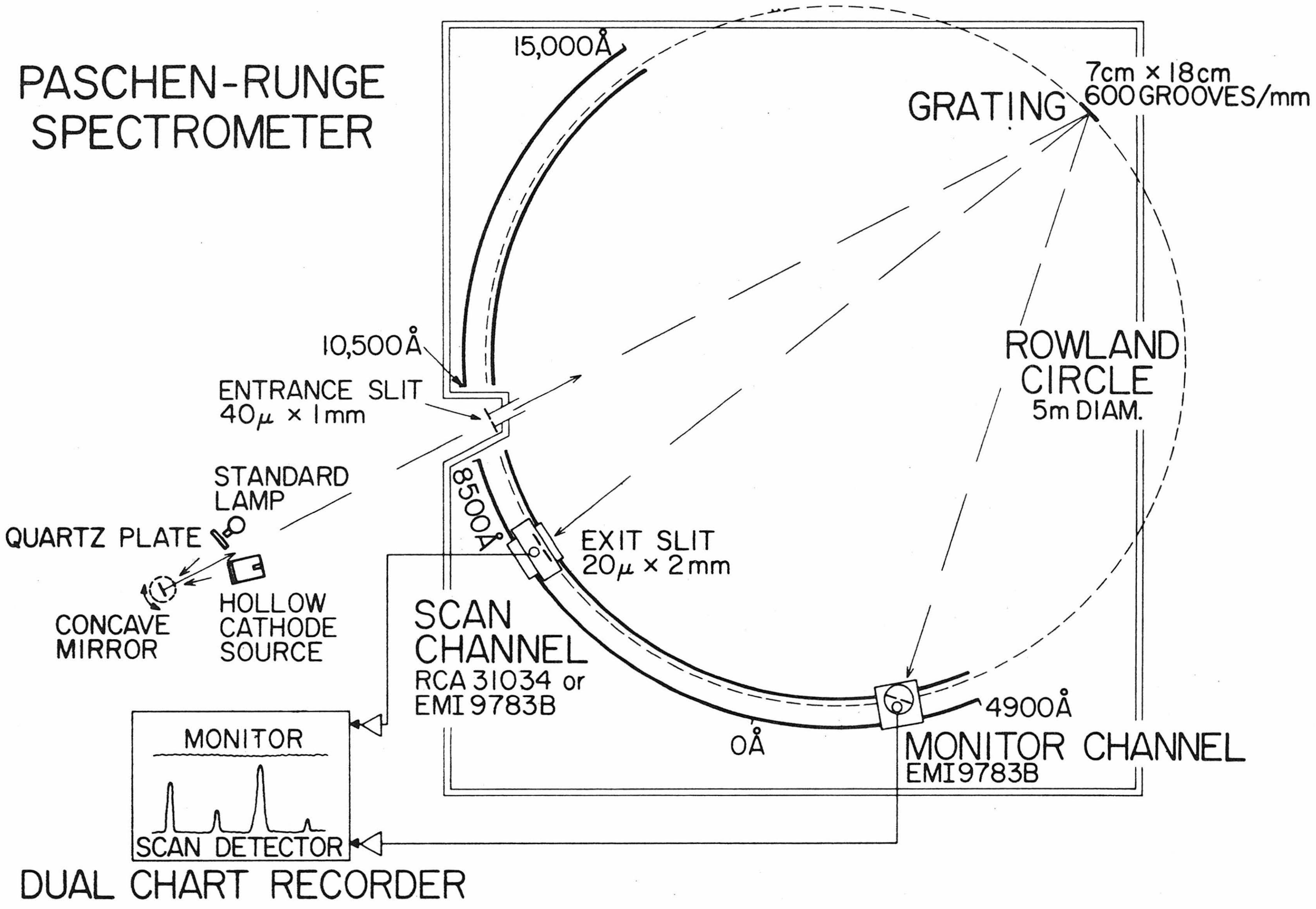

PASCHEN-RUNGE SPECTROMETER

FIGURE 7

a) Results of the spectral search for λ10061.29 ($y^3G^o_4$ - g^3F_3 , RMT NO. 284) using the hollow cathode source and the McPherson system with a 600 lines/mm grating in first order. The detector was an HTV R406 photomultiplier tube having an S-1 spectral response. The data were stored in a multi-channel analyzer operated in the time mode. The pass band of the monochromator is 2.0Å fwhm. The statistical uncertainties are shown.

b) Observed hollow cathode spectrum in the region of λ4838.651 ($z^1G^o_4$ - g^3F_3, RMT No. 260). The observing conditions are the same as for (a). Both spectra were accumulated over the same counting times. Both transitions are from the same upper level.

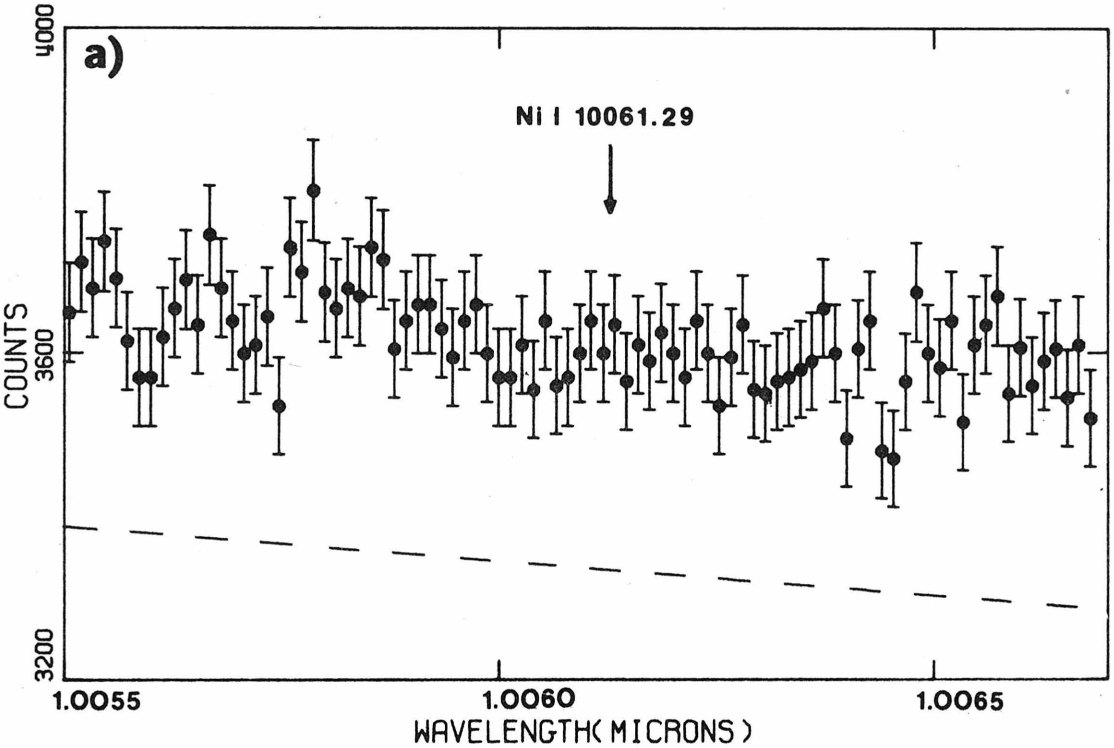
a)
Ni I 10061.29
COUNTS
4000
3600
3200
1.0055
1.0060
1.0065
WAVELENGTH(MICRONS)

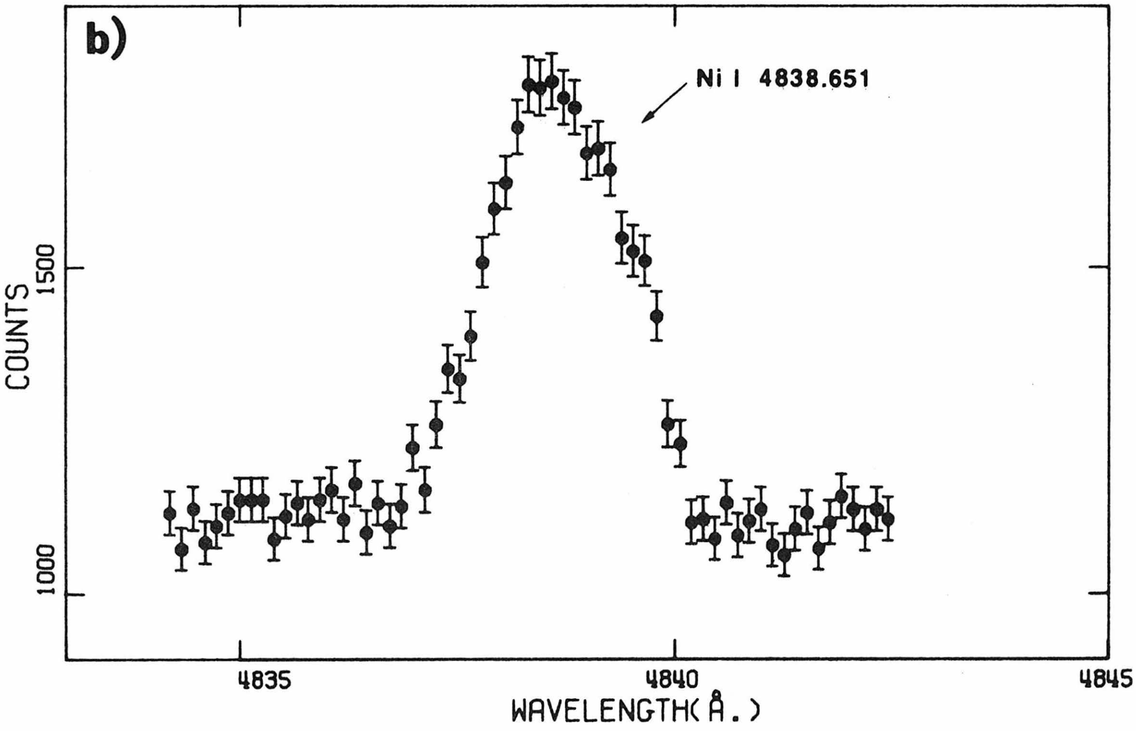
b)
Ni I 4838.651
COUNTS
1500
1000
4835
4840
4845
WAVELENGTH(Å.)

FIGURE 8

$\log_{10}(gf_{CIT})$ are plotted against $\log_{10}(gf_{GHR})$. CIT refers to values measured in this thesis, GHR are from Garz, Heise and Richter (1970). The dashed line has a slope of unity and passes through the origin. It is not a fit to the data points.

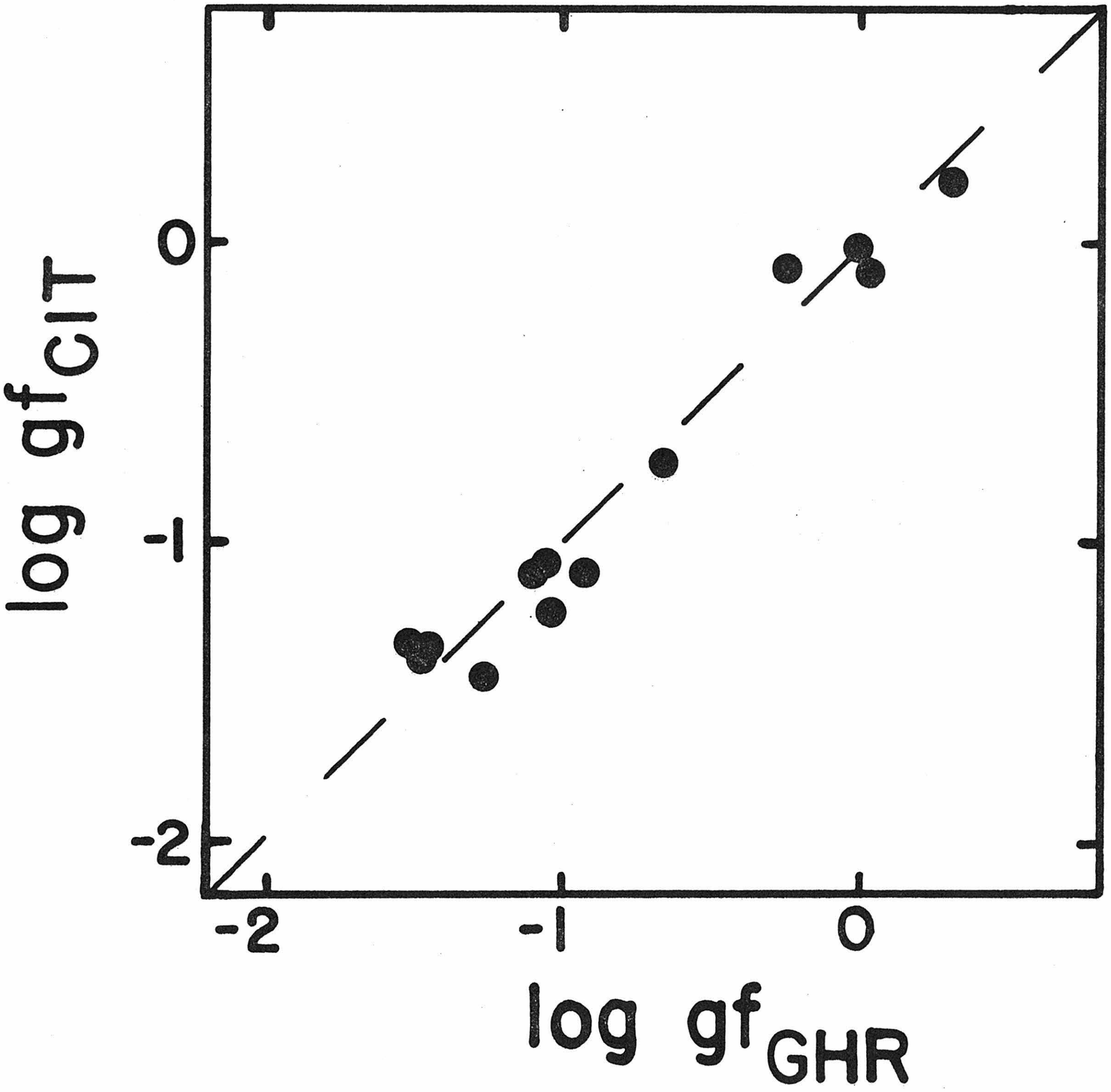
log gf$_{CIT}$
0
-1
-2
-2
-1
0
log gf$_{GHR}$

FIGURE 9

$\log_{10}(gf_{CIT})$ are plotted against $\log_{10}(gf_{CORLISS})$. The solid diamonds are for transitions out of upper levels with $E_u > 6.0$ eV. The solid squares are for transitions out of upper levels with $E_u < 6.0$ eV. The solid line passes through the origin and has a slope of unity.

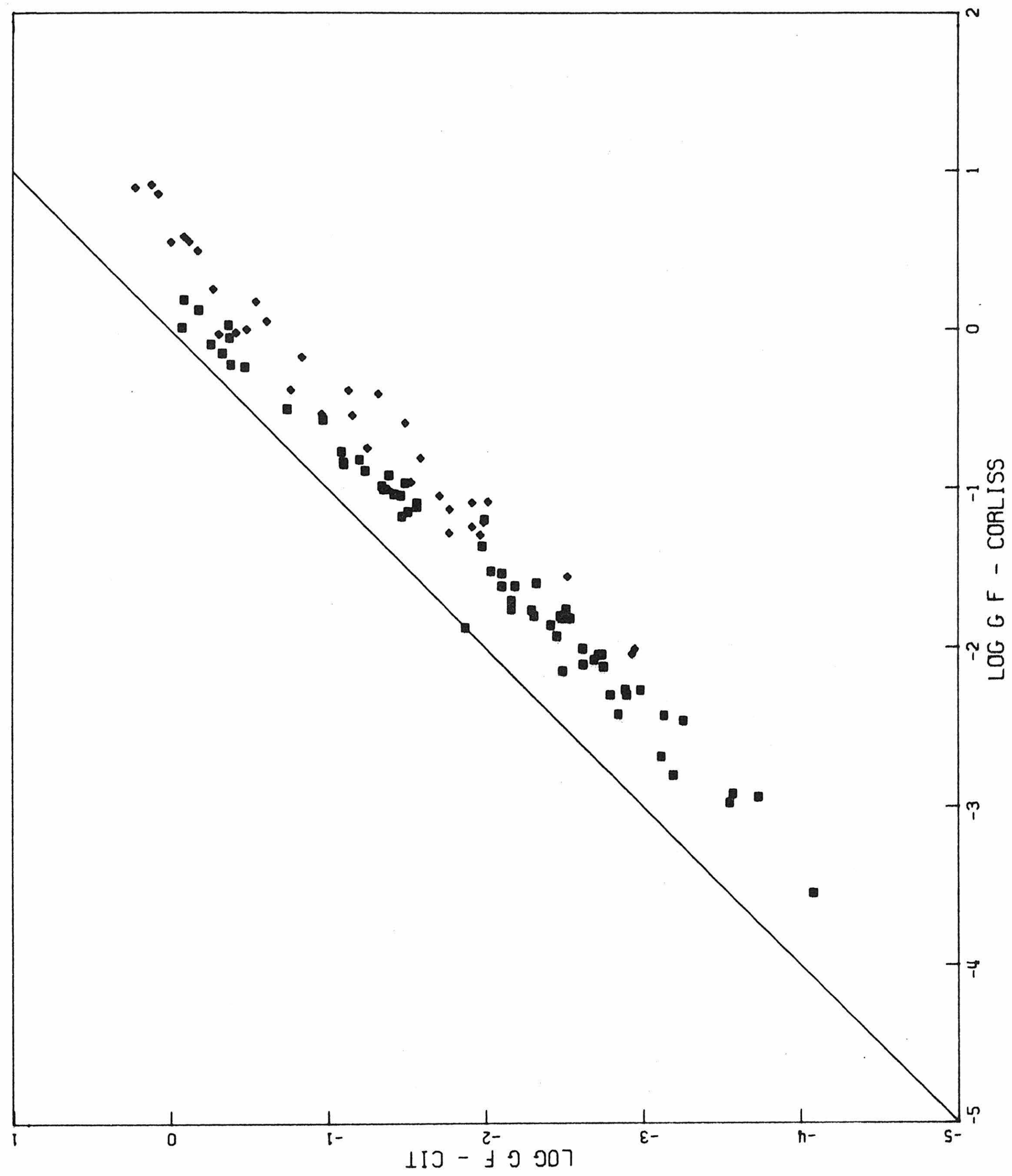
LOG G F - CORLISS
2
1
0
-1
-2
-3
-4
-5
LOG G F - CIT
1
0
-1
-2
-3
-4
-5

FIGURE 10

$\log_{10}(gf_C/gf_{CIT})$ as a function of wavelength. The subscript "C" refers to the values chosen by Corliss (1965) as "best" values. The plotting symbols are the same as for Figure 9. (Refer to page 49).

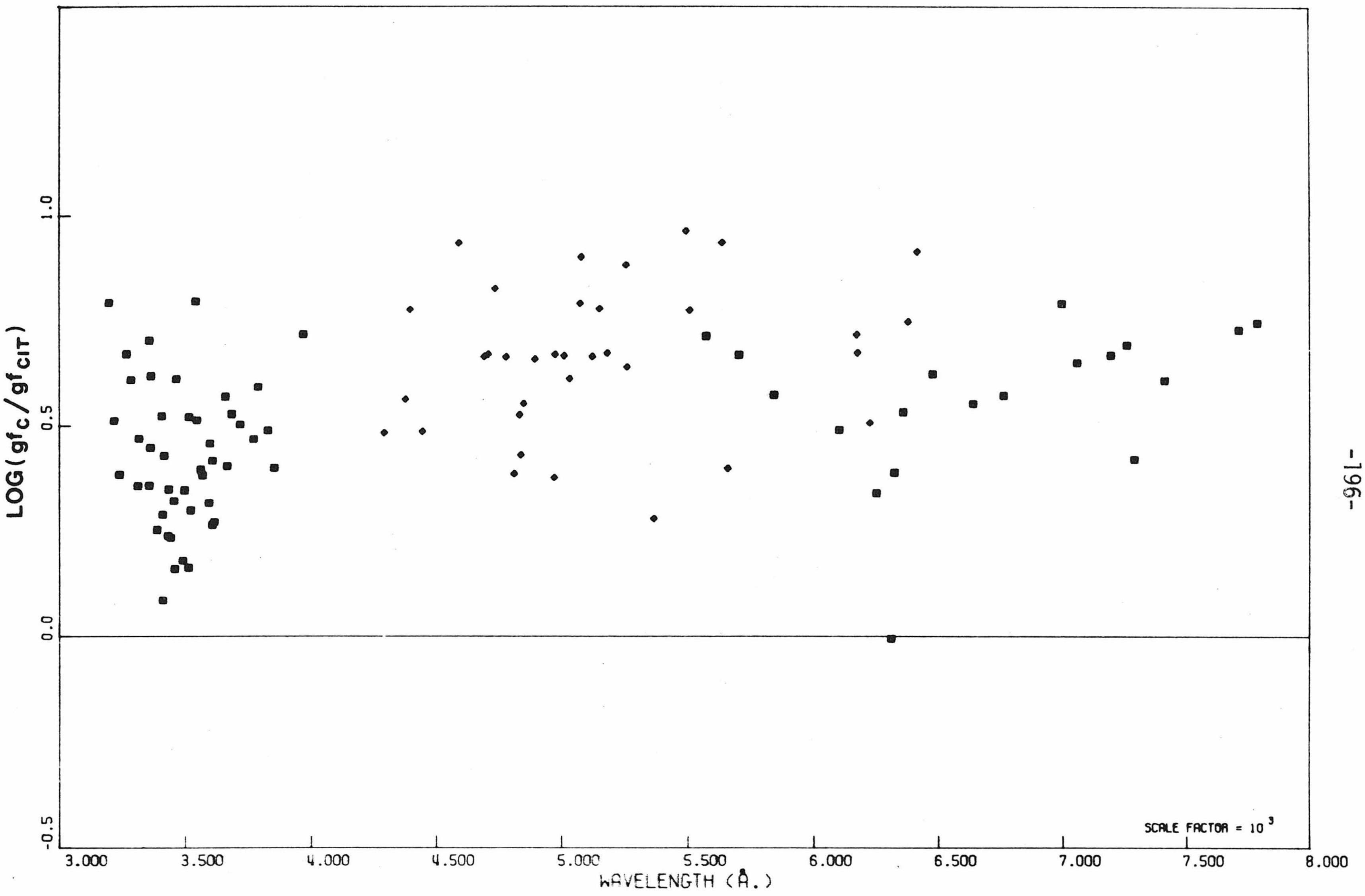
LOG(gf$_C$/gf$_{CIT}$)
1.0
0.5
0.0
-0.5
3.000
3.500
4.000
4.500
5.000
5.500
6.000
6.500
7.000
7.500
8.000
WAVELENGTH (Å.)
SCALE FACTOR = 10^3

FIGURE 11

Synthesis of the observed solar spectrum (Kitt Peak Preliminary Solar Atlas) in the region around Ni I λ5157.993 (RMT No. 111). The solid spectrum at the left is the observed intensity and the dots represent the sum of the synthesized absorption lines shown individually at the right. The residual shown at the top left is the difference between the observed and synthesized spectra. The Ni I line is hatched in the right figure. The value of W^{KP} for λ5157 was found to be 18.7 mÅ.

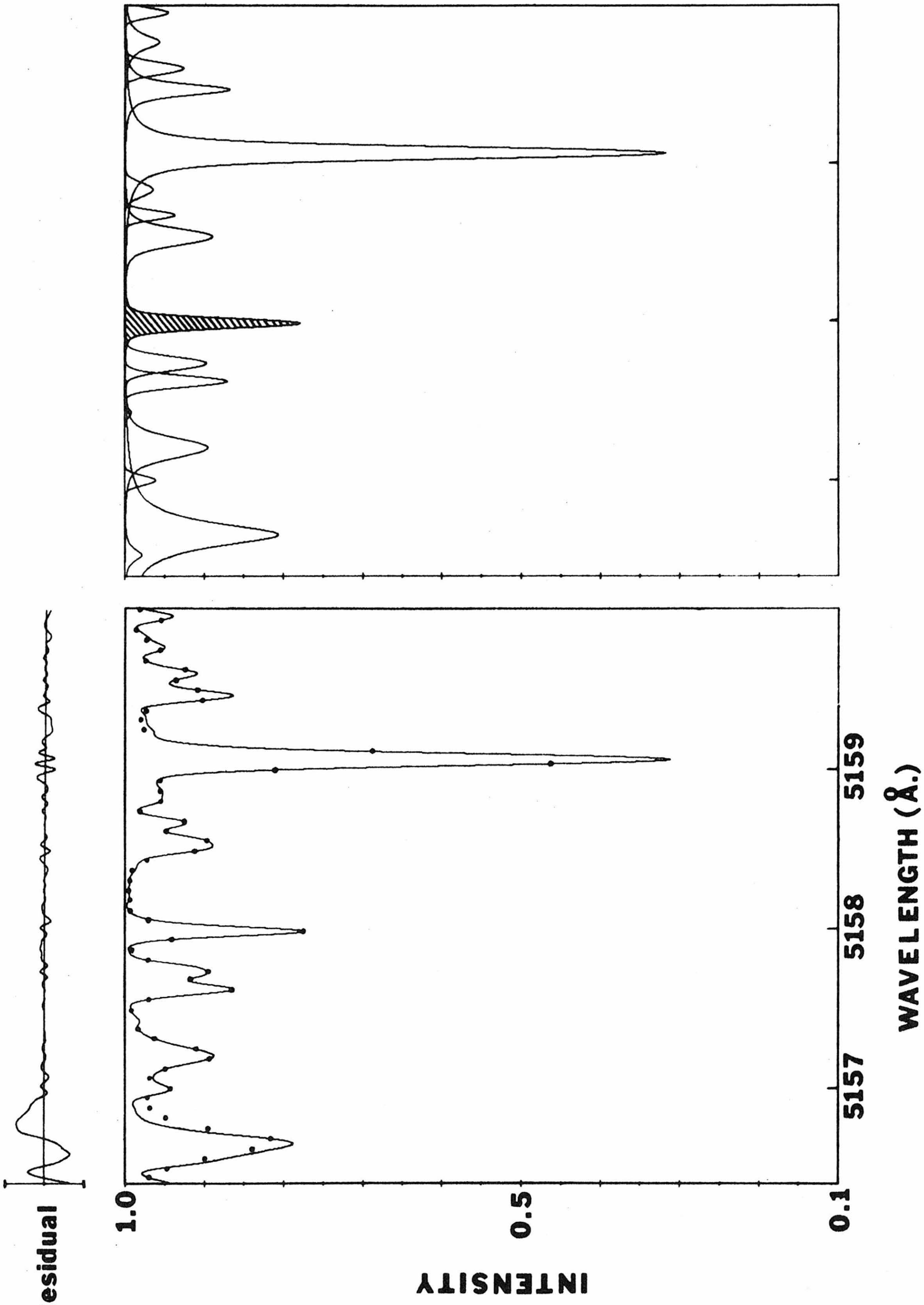
Residual
INTENSITY
1.0
0.5
0.1
5157
5158
5159
WAVELENGTH (Å.)

FIGURE 12

Synthesis of the solar spectrum in the vicinity of Ni I λ4009.984 (RMT No. 150), which is hatched in the right figure. Format is the same as for Figure 11. The value of W^{KP} obtained was 14.5 mÅ.

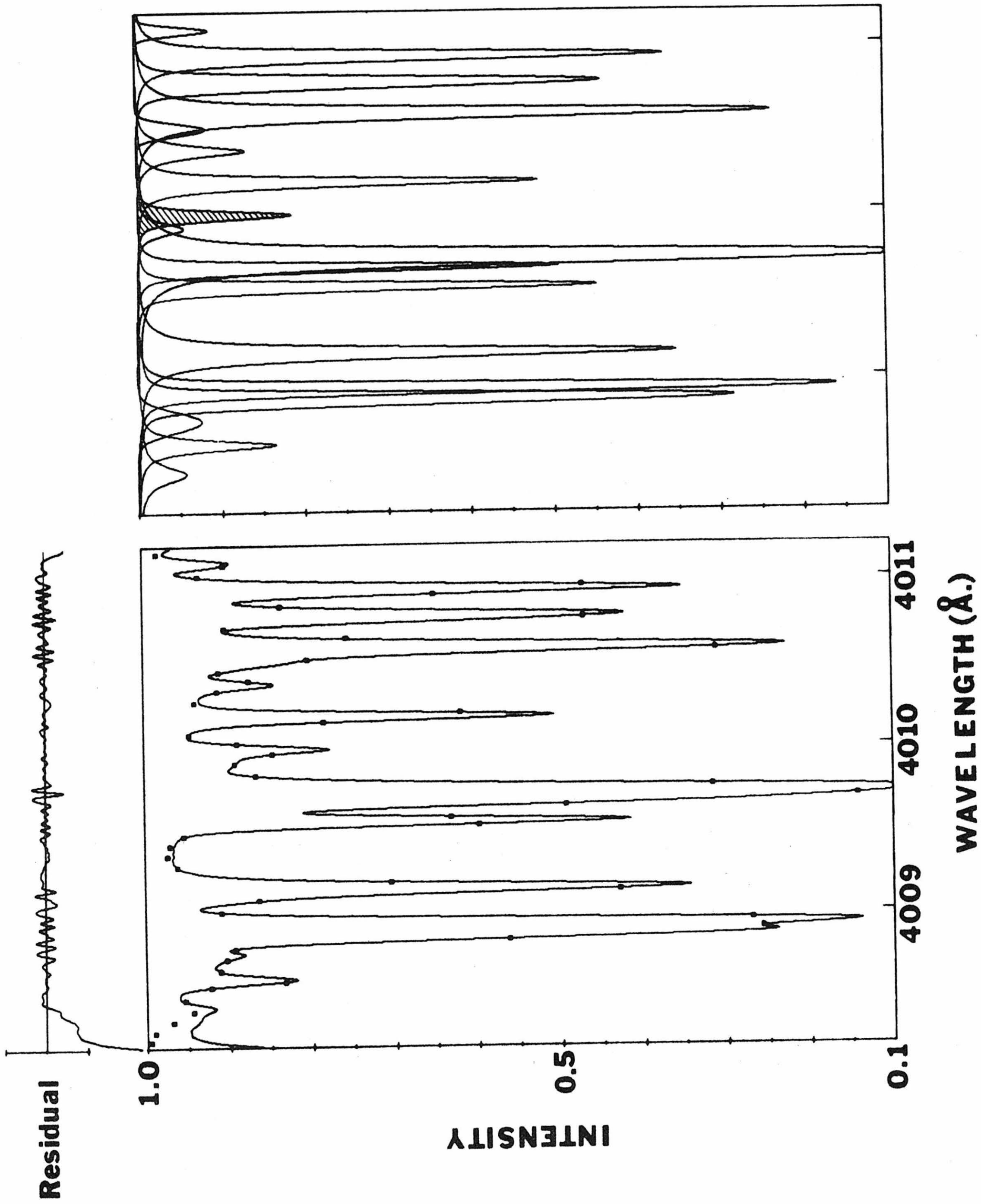
Residual
INTENSITY
1.0
0.5
0.1
4009
4010
4011
WAVELENGTH (Å.)

FIGURE 13

$\log_{10}(W^{KP}/W^{NBS})$ as a function of wavelength. W^{KP} were obtained from the Kitt Peak Preliminary Solar Atlas. W^{NBS} are taken from Moore *et al*. (1966).

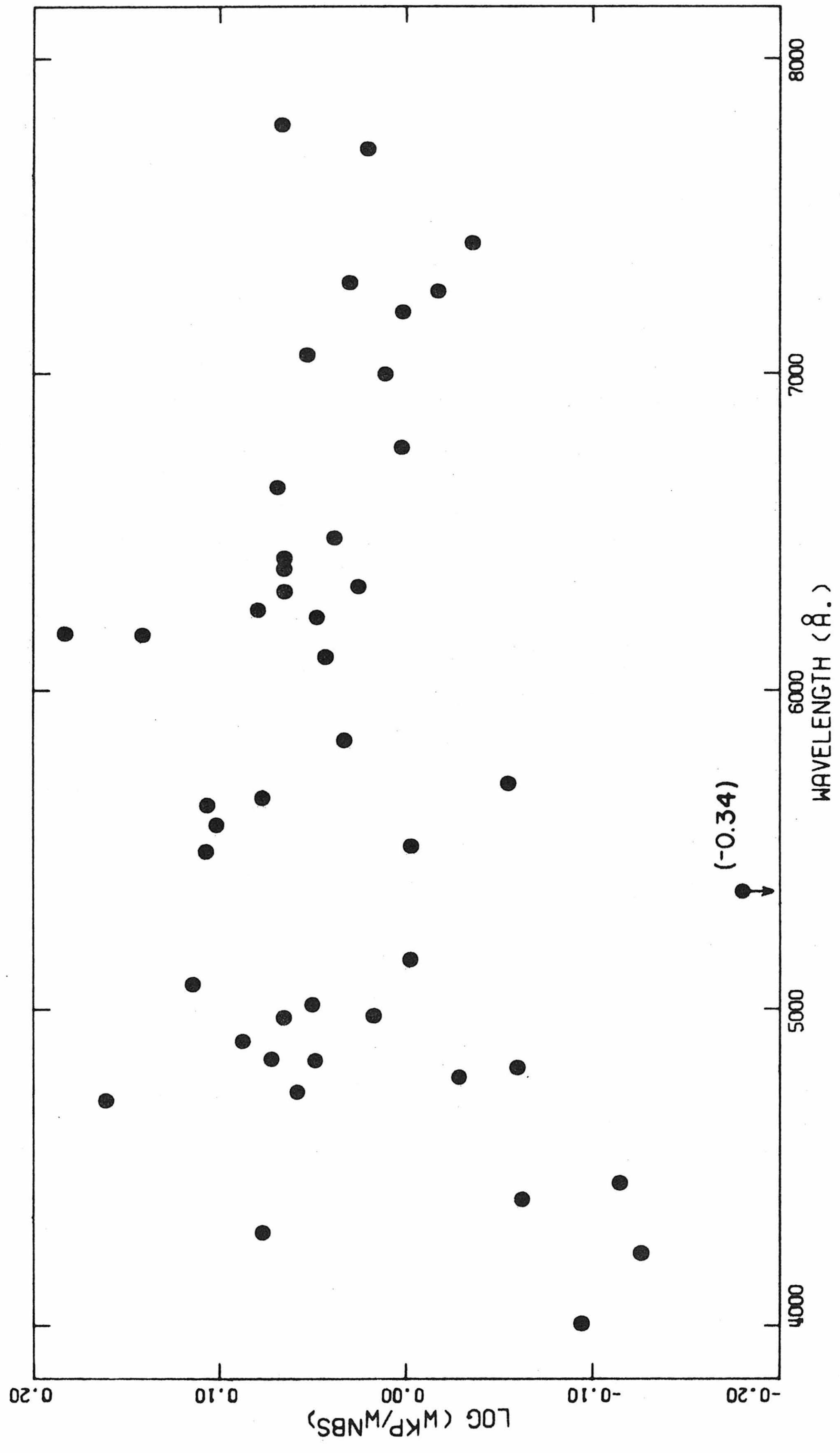
LOG (W_{KP}/W_{NBS})
0.20
0.10
0.00
-0.10
-0.20
4000
5000
6000
7000
8000
WAVELENGTH (Å.)
(-0.34)

FIGURE 14

$\log_{10}(W^{KP}/W^{NBS})$ as a function of the line strength, W^{NBS}. W^{NBS} are taken from Moore _et al_. (1966), W^{KP} were obtained from the Kitt Peak Preliminary Solar Atlas.

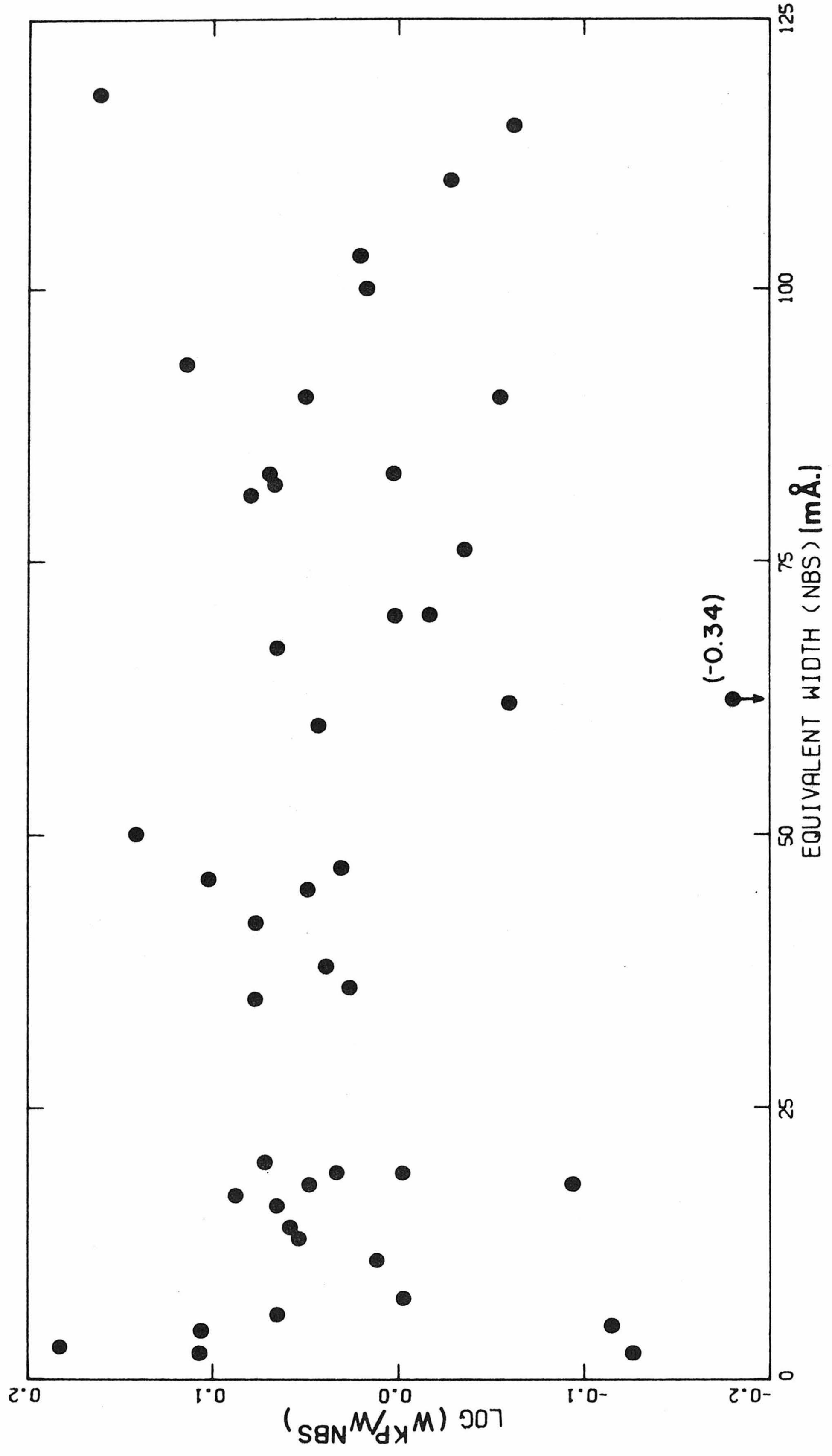
LOG (W KP/W NBS)
0.2
0.1
0.0
-0.1
-0.2
EQUIVALENT WIDTH (NBS) [mÅ]
0
25
50
75
100
125
(-0.34)

FIGURE 15

Synthesis of the solar spectrum in the vicinity of Ni I λ5371.33 (not listed in the RMT but tabulated by Corliss (1965)), which is hatched in the right figure. Format is the same as for Figure 11. The Ni I line is blended with the Fe I line at λ5371.493 (RMT No. 15). The residual is larger than usual in the vicinity of the Ni I line and the value of W^{KP} = 28.7 mÅ obtained from the synthesis has a large uncertainty. (Refer to page 56).

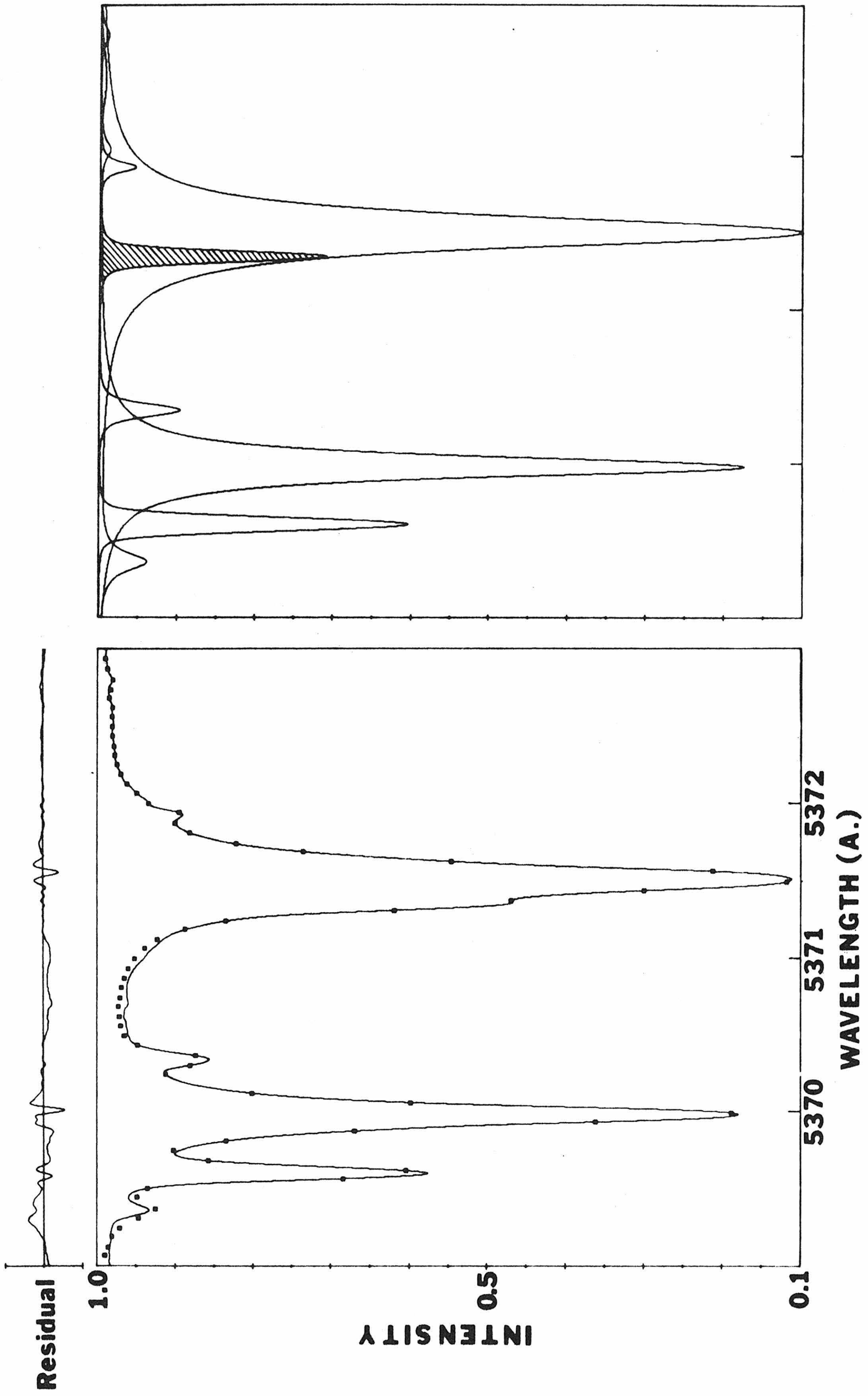
Residual
1.0
0.5
0.1
INTENSITY
5370
5371
5372
WAVELENGTH (A.)

FIGURE 16

Tracings of the solar spectrum in the vicinity of the Ni I line at λ3367.892 (RMT No. 20). The large arrow at the bottom of each tracing points to the Ni I line, the small arrow points to the nearby Zr II line at λ3367.81 (RMT No. 11). Left, Michigan Atlas (unpublished); top right, Brückner (1960); bottom right, Kitt Peak Preliminary Solar Atlas. (Refer to page 56).

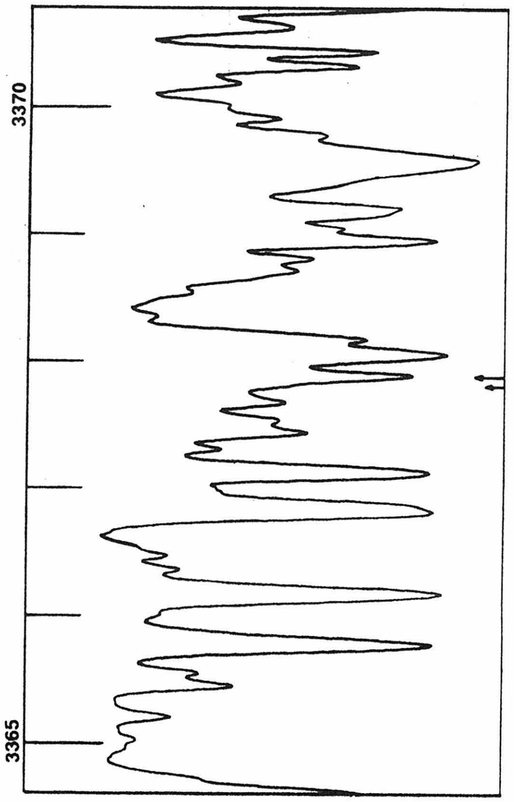
3370
3365

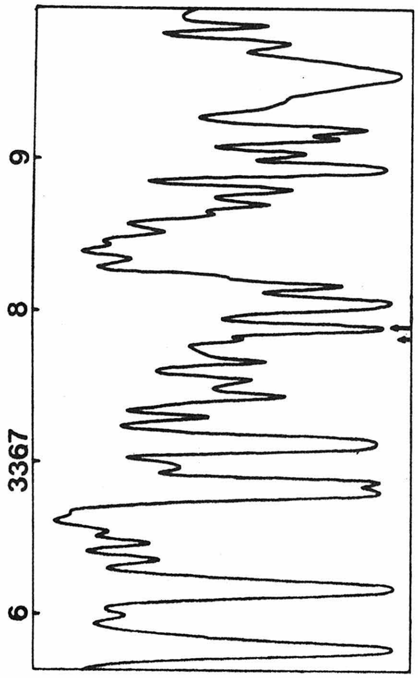
9
8
3367
6

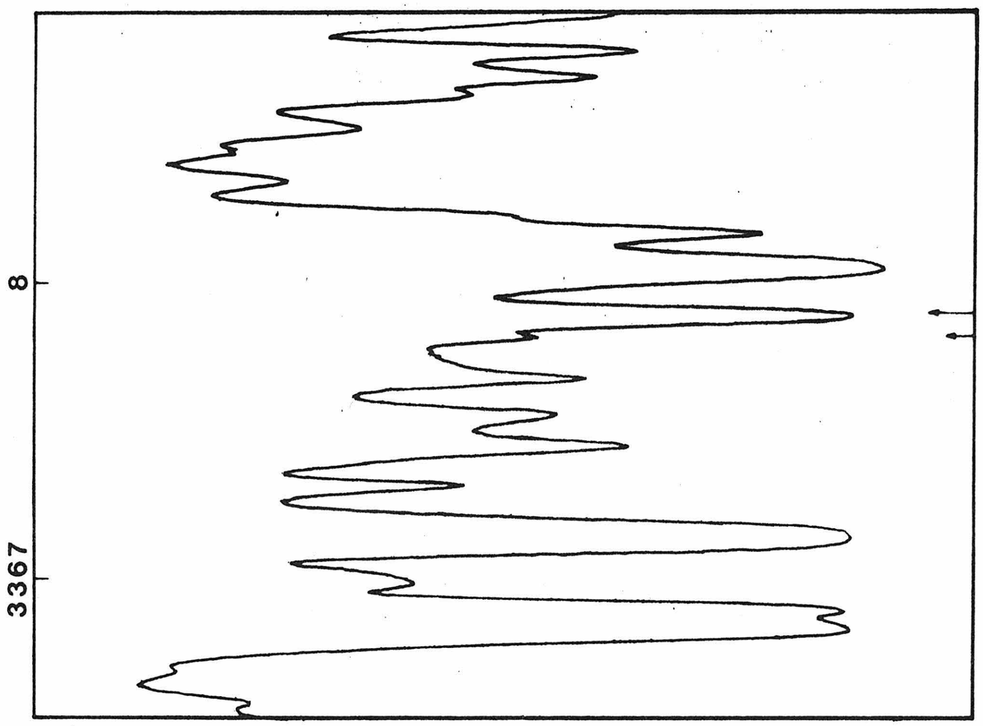
8
3367

FIGURE 17

$\log_{10}(W^{KP}/W^{Mich})$ as a function of wavelength. Values of W^{Mich} were obtained by Holweger (1967) from the Michigan Atlas (unpublished). W^{KP} are from the Kitt Peak Preliminary Solar Atlas.

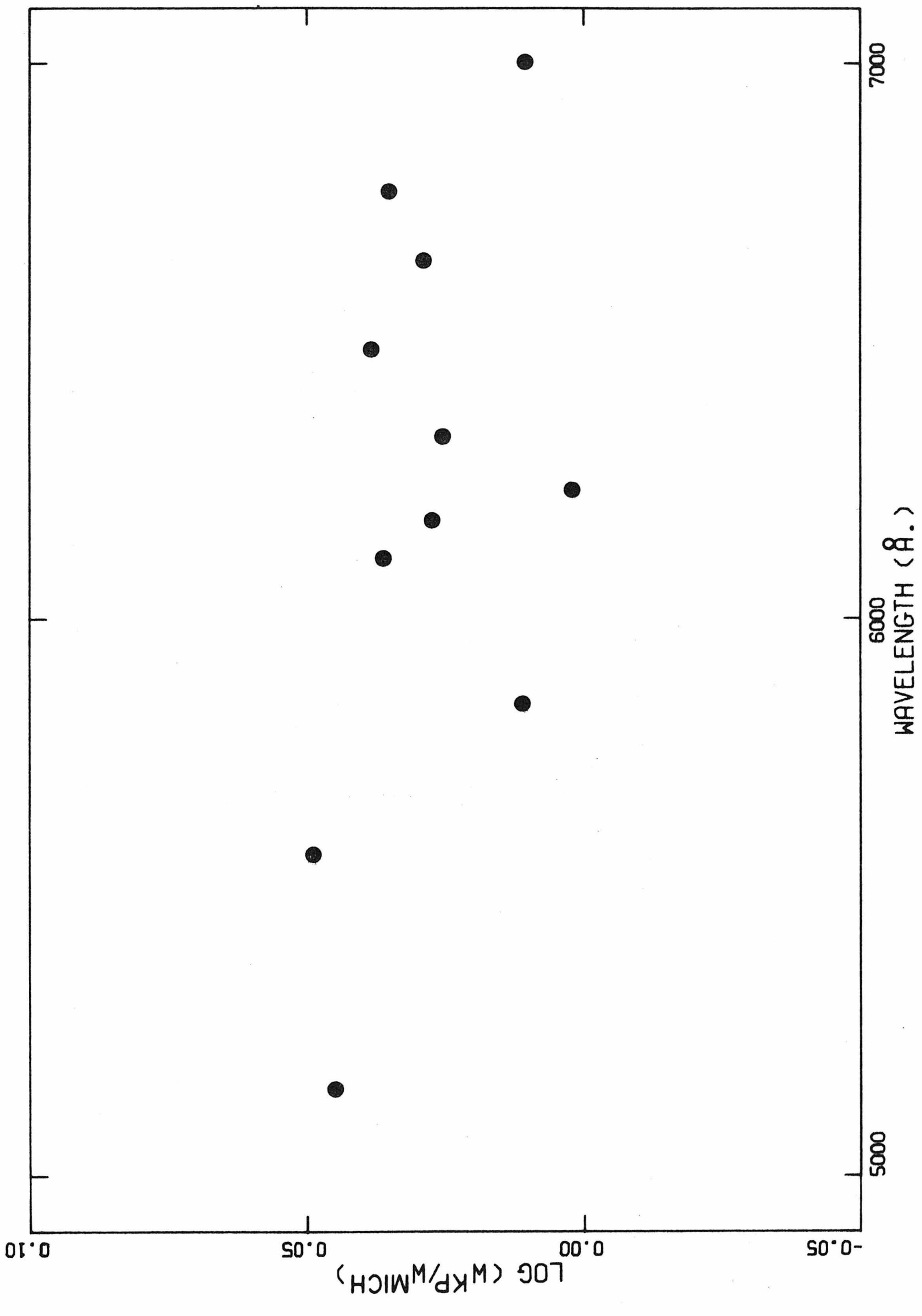
LOG (W KP/W MICH)
0.10
0.05
0.00
-0.05
WAVELENGTH (Å.)
5000
6000
7000

FIGURE 18

Solar curve of growth for Ni I for the center of the solar disc. The abscissae are calculated from the values of log gf measured in this work (see Tables 5-17) and the values of $\log \Gamma$ from the model of Cayrel and Jugaku (1963). The values of W and $\log(gf\,\Gamma)$ are given in Table 21. The solid circles represent data obtained in this work. The open squares are the data of Garz (1971) using W^{Mich}. The open circle is for Ni I λ3722.484 to show the unreliability of W^{NBS} (see Figure 19). The solid curves are theoretical curves of growth taken from Hunger (1956) for different values of the damping parameter, a . They have been fitted to the solid data points with abscissae ≤ 4.5 in a least squares sense. (Refer to pages 59-63).

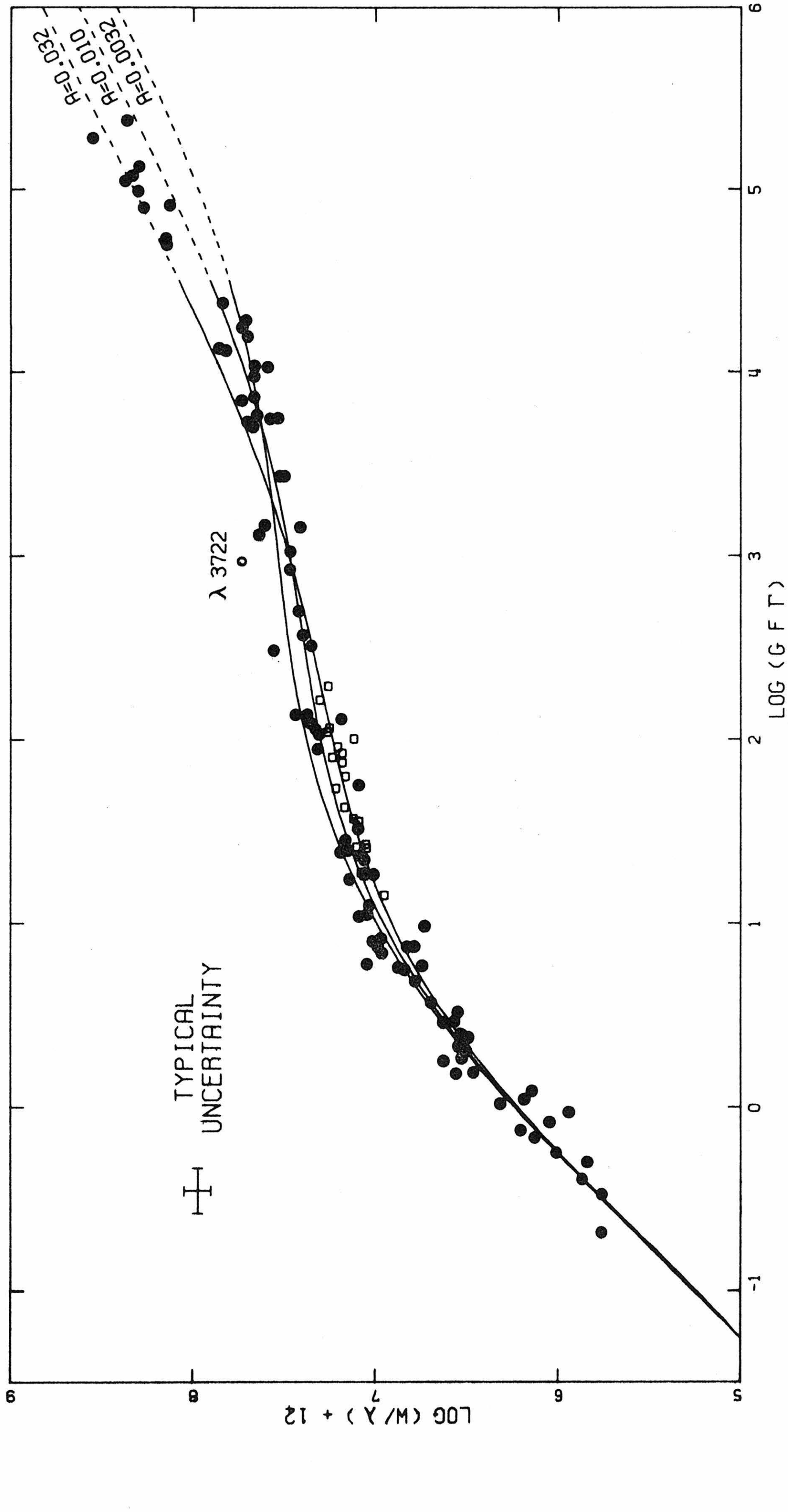
A=0.032
A=0.010
A=0.0032
λ 3722
TYPICAL
UNCERTAINTY
LOG (G F Γ)
LOG (W/λ) + 12
-1
0
1
2
3
4
5
6
5
6
7
8
9

FIGURE 19

A tracing of the solar spectrum from the Kitt Peak Preliminary Solar Atlas in the vicinity of the line Ni I λ3722.484 (RMT No. 18). The proximity of the very strong Fe I lines at λ3719.935 (RMT No. 5) and λ3722.564 (RMT No. 5) renders a synthesis of the spectrum very difficult. (Refer to page 62).

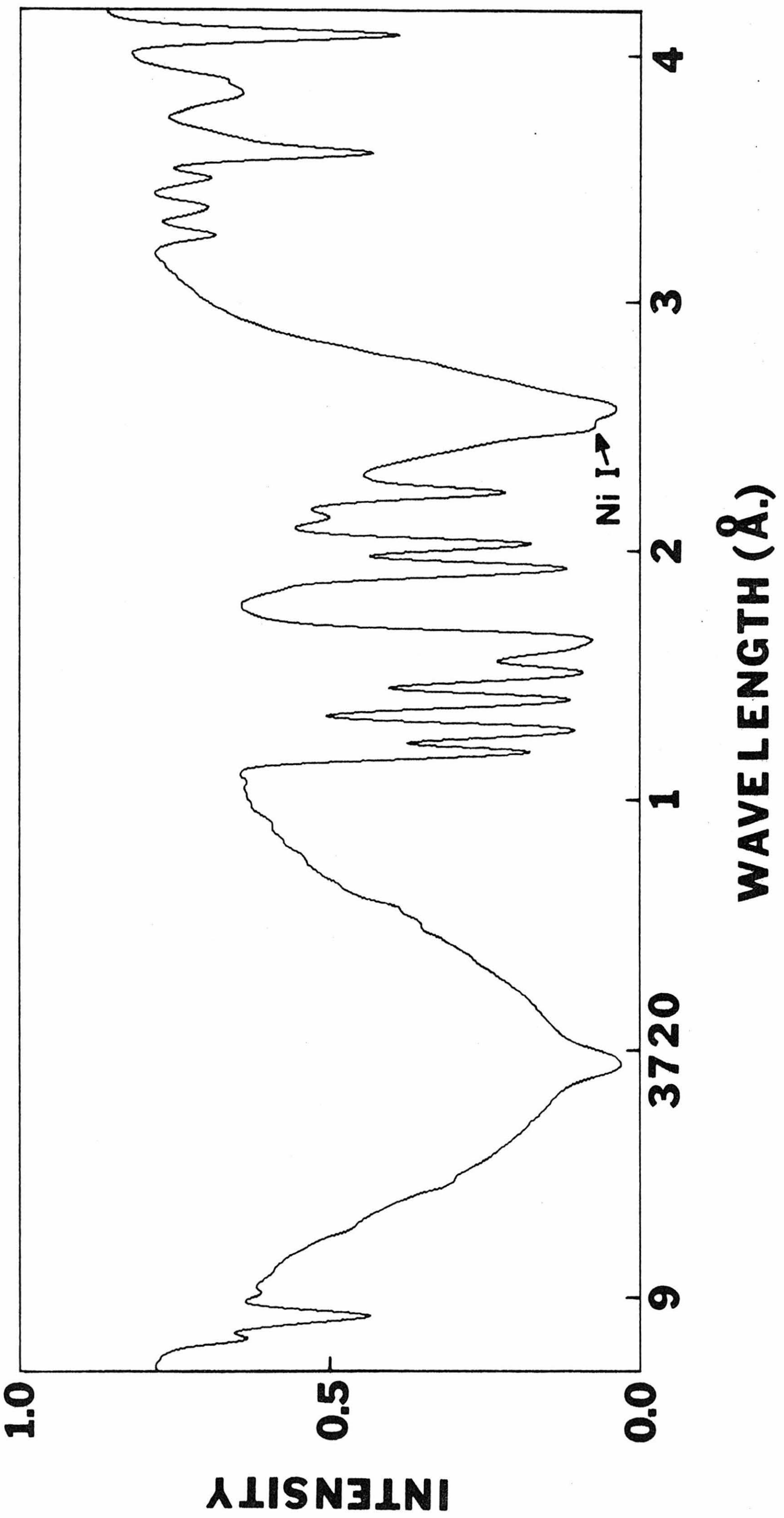
INTENSITY
1.0
0.5
0.0
9
3720
1
2
3
4
WAVELENGTH (Å.)
Ni I→

FIGURE 20

Relative detection efficiency of the McPherson spectrometer system in first order as a function of wavelength. The dotted curve has been drawn to aid the reader. The solid curve shows a typical S-1 photocathode spectral response function. The grating has 600 lines/mm and the blaze wavelength is 10,000Å. (Refer to page 94).

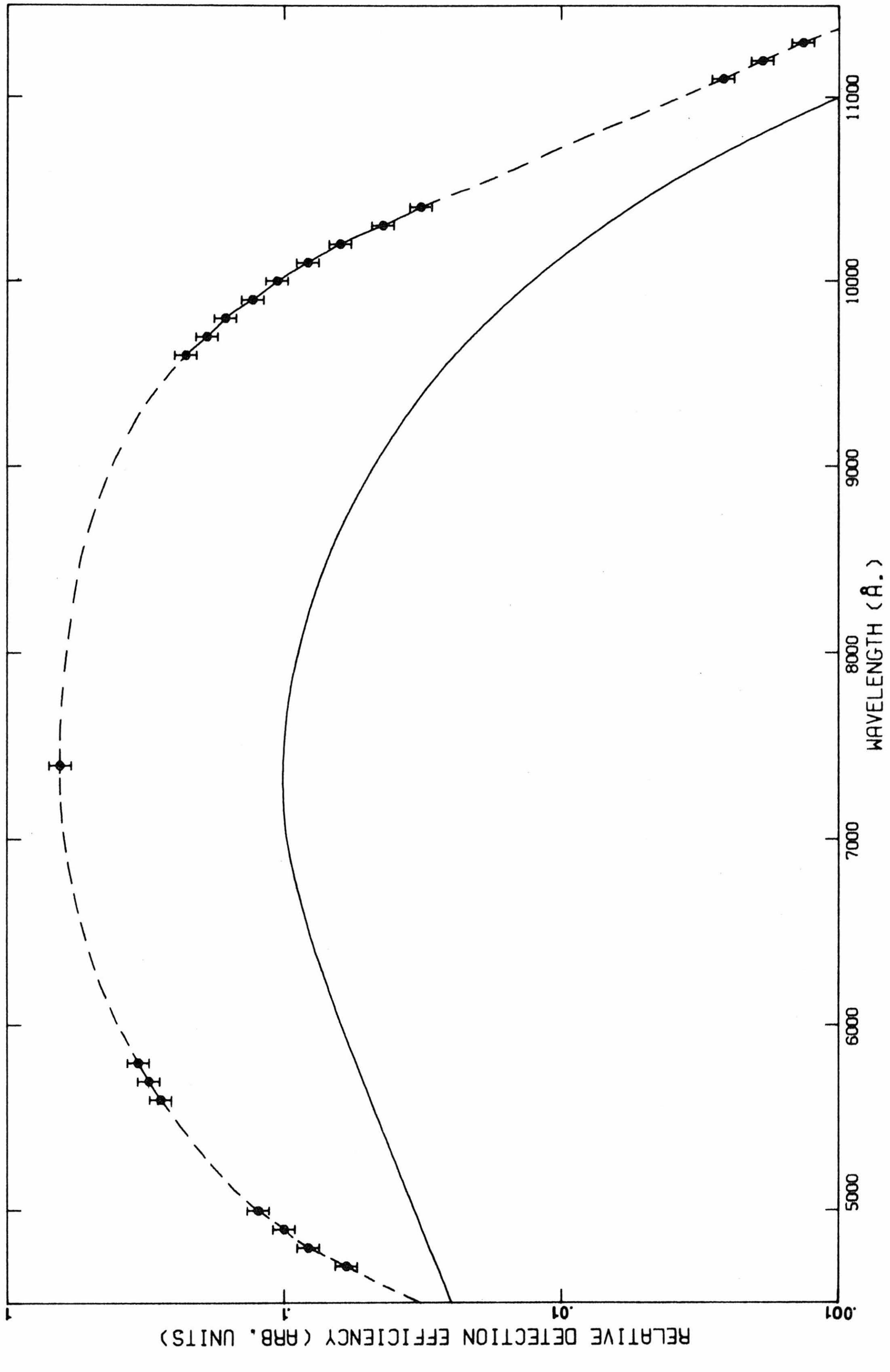
RELATIVE DETECTION EFFICIENCY (ARB. UNITS)
1
.1
.01
.001
WAVELENGTH (Å.)
5000
6000
7000
8000
9000
10000
11000

FIGURE 21

Theoretically calculated root-mean-square scattering angles for nickel on carbon as a function of foil thickness (t) and incident beam energy, E_0 . These curves were used to correct the lifetime data for those particles scattered outside the field of view of the monochromator downstream from the foil.

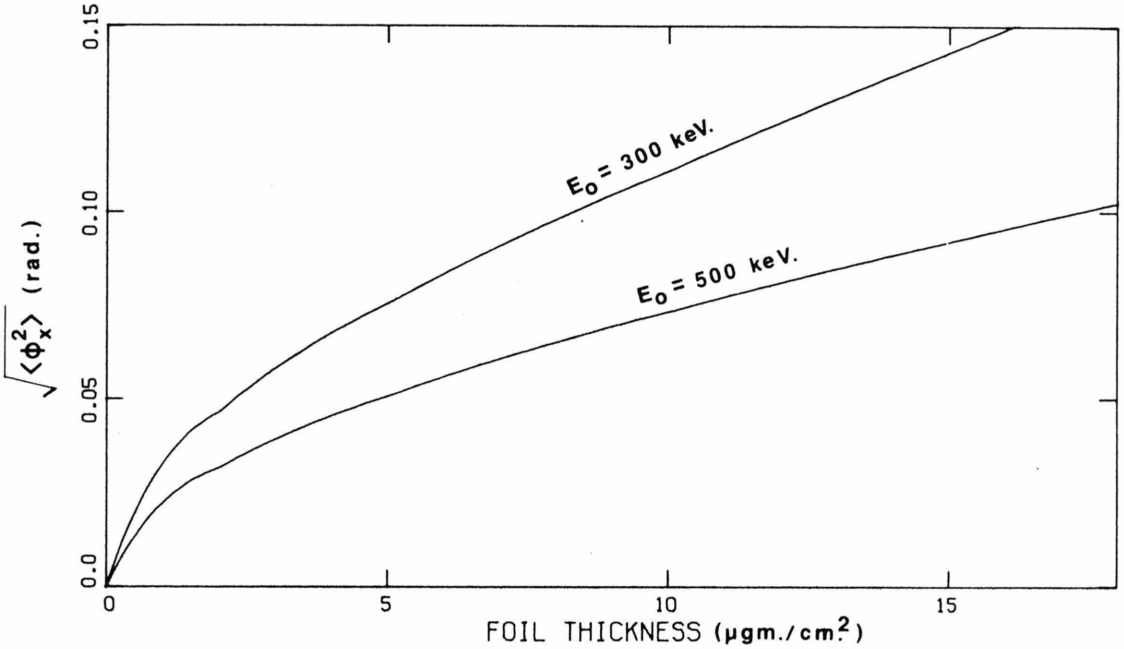
0.0
0.05
0.10
0.15
$\sqrt{\langle\phi_x^2\rangle}$ (rad.)
0
5
10
15
FOIL THICKNESS (μgm./cm.^{2})
E_0 = 300 keV.
E_0 = 500 keV.

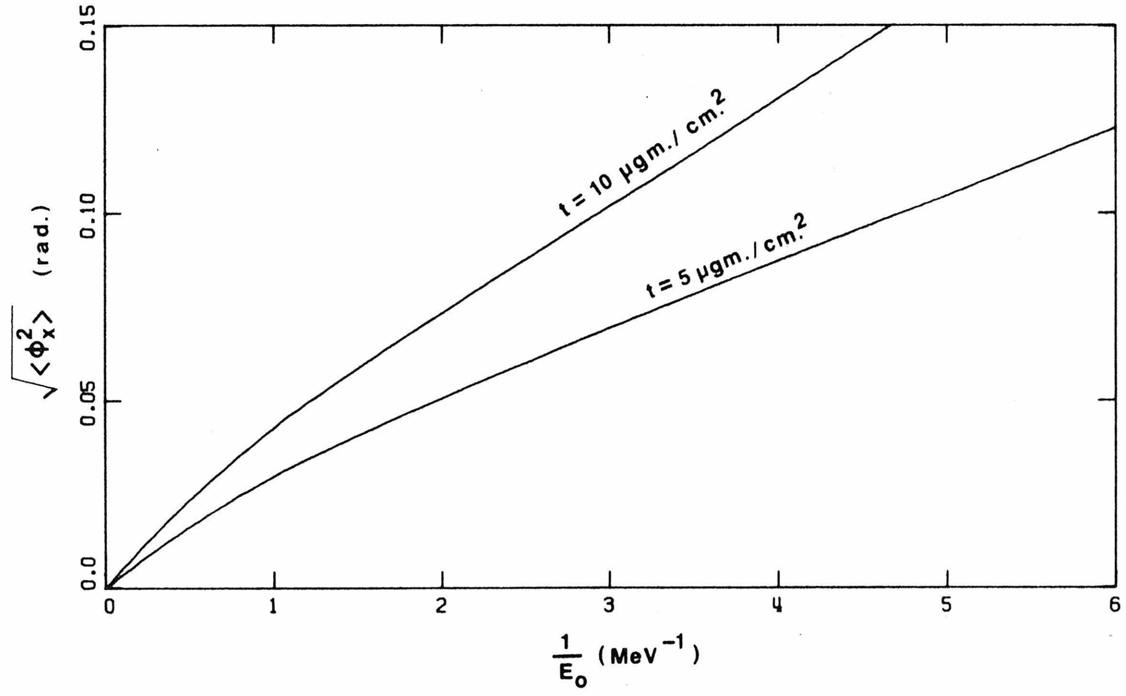
0.0
0.05
0.10
0.15
$\sqrt{\langle\phi_x^2\rangle}$ (rad.)
0
1
2
3
4
5
6
$\frac{1}{E_0}$ (MeV^{-1})
t = 10 μgm./cm.^{2}
t = 5 μgm./cm.^{2}

FIGURE 22

$\log_{10}(I_{JJ'}/g_J A_{JJ'})$ as a function of excitation energy, E_J, for branches out of levels with $3.54 \text{ eV} \leq E_j \leq 3.90 \text{ eV}$. The solid curve is a straight line fit to the data. (Refer to pages 102 and 103).

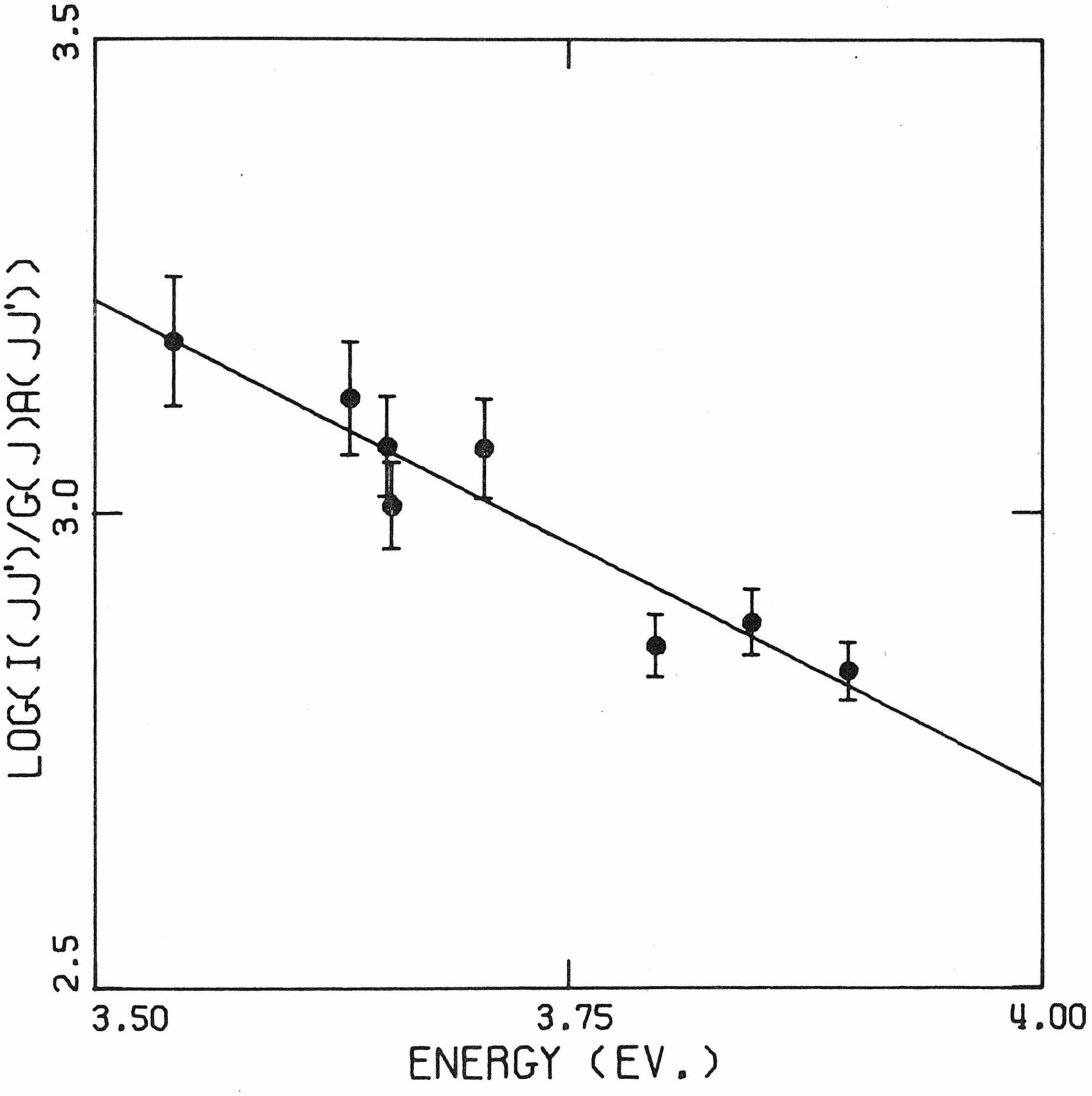
3.5
3.0
2.5
LOG(I(JJ')/G(J)A(JJ'))
3.50
3.75
4.00
ENERGY (EV.)